

This is the accepted manuscript of the following article:

Senn, A.-C., Kaegi, R., Hug, S. J., Hering, J. G., Mangold, S., & Voegelin, A. (2015). Composition and structure of Fe(III)-precipitates formed by Fe(II) oxidation in water at near-neutral pH: interdependent effects of phosphate, silicate and Ca. *Geochimica et Cosmochimica Acta*, 162, 220–246. <http://doi.org/10.1016/j.gca.2015.04.032>

This manuscript version is made available under the CC-BY-NC-ND 4.0 license <http://creativecommons.org/licenses/by-nc-nd/4.0/>

Composition and structure of Fe(III)-precipitates formed by Fe(II) oxidation in water at near-neutral pH: Interdependent effects of phosphate, silicate and Ca

Anna-Caterina Senn^{a,b}, Ralf Kaegi^a, Stephan J. Hug^a, Janet G. Hering^{a,b,c},
Stefan Mangold^d, Andreas Voegelin^{a,*}

^a Eawag, Swiss Federal Institute of Aquatic Science and Technology, Ueberlandstrasse 133, CH-8600 Duebendorf, Switzerland

^b Department of Environmental Sciences, Institute of Biogeochemistry and Pollutant Dynamics, ETH, Swiss Federal Institute of Technology, Zurich, Switzerland

^c School of Architecture Civil and Environmental Engineering, EPFL, École Polytechnique Fédérale de Lausanne, Switzerland

^d Karlsruhe Institute of Technology, Institute of Synchrotron Radiation, Hermann-von-Helmholtz Platz 1, D-76344 Eggenstein-Leopoldshafen, Germany

* Corresponding author. E-mail address: andreas.voegelin@eawag.ch, phone +41 58 765 54 70, fax +41 58765 52 10

ABSTRACT

We studied the interdependent effects of phosphate, silicate and Ca on the formation of Fe(III)-precipitates by oxidation of 0.5 mM Fe(II) in near-neutral bicarbonate-buffered aqueous solutions at concentrations relevant for natural water resources. Complementary results obtained by a suite of analytical techniques including X-ray absorption spectroscopy and transmission electron microscopy showed that the ratio of initially dissolved phosphate over Fe(II) ($(P/Fe)_{init}$) had a major impact on precipitate formation. At $(P/Fe)_{init}$ above a critical ratio ($(P/Fe)_{crit}$) of ~ 0.5 in 8 mM $NaHCO_3$ and ~ 0.8 in 4 mM $Ca(HCO_3)_2$ electrolyte, Fe(II) oxidation led to exclusive formation of amorphous basic Fe(III)-phosphate or Ca-Fe(III)-phosphate ((Ca-)Fe(III)-phosphate) with maximum precipitate P/Fe ratios ($(P/Fe)_{ppt}$) of ~ 0.7 in Na and ~ 1.1 in Ca electrolyte. Enhanced phosphate uptake in the presence of Ca was due to phosphate-Ca interactions coupled to Fe precipitation, mainly formation of mitridatite-like Ca-Fe(III)-phosphate polymers and Ca-phosphate polymers. At $(P/Fe)_{init} < (P/Fe)_{crit}$, in the absence of silicate, (Ca-)Fe(III)-phosphate precipitation was followed by the formation of poorly crystalline lepidocrocite and concomitant transformation of the (Ca-)Fe(III)-phosphate into a phosphate-rich ferrihydrite-type precipitate with a $(P/Fe)_{ppt}$ of ~ 0.25 . In the presence of 0.5 mM silicate, initially formed (Ca-)Fe(III)-phosphate nanoparticles became coated with silicate-rich ferrihydrite during continuing Fe(II) oxidation and only limited transformation of the (Ca-)Fe(III)-phosphate occurred. The results from this study indicate the complexity of Fe(III)-precipitate formation in the presence of interfering solutes and its consequences for precipitate structure and phosphate sequestration. The findings provide a solid basis for further studies of the reactivity of different Fe(III)-precipitate types and for the systematic assessment of their impact on Fe, phosphate and trace elements dynamics in natural and engineered systems.

1. INTRODUCTION

The formation of amorphous to poorly-crystalline Fe(III)-precipitates by oxidation of dissolved Fe(II) in aerated water critically influences the biogeochemical cycling and the bioavailability of Fe (Stumm and Sulzberger, 1992; Taylor and Konhauser, 2011; Raiswell and Canfield, 2012). Because of their high sorption capacity and nanometer-range size, Fe(III)-precipitates may act as immobilizing sorbents or colloidal carriers of other major and trace elements and thereby critically influence the fate and impact of contaminants and nutrients in natural and technical systems (Waychunas et al., 2005; Hassellöv and von der Kammer, 2008).

The oxidation of dissolved Fe(II) in water triggers the polymerization and precipitation of Fe(III). Other solutes may interfere with Fe(III) polymerization and co-precipitate with Fe(III). This results in compositionally and structurally diverse Fe(III)-precipitates with different chemical and colloidal properties (Tessenow, 1974; Mayer and Jarrell, 1996; Gunnars et al., 2002; Bonneville et al., 2004; Raiswell et al., 2010; van Genuchten et al., 2014b). In near-neutral bicarbonate-buffered surface water, groundwater, and drinking water, key solutes controlling the formation and structure of Fe(III)-precipitate during Fe(II) oxidation are the oxyanions phosphate and silicate (silicic acid at near-neutral pH) that interfere with Fe(III) polymerization (Rose et al., 1996; Doelsch et al., 2000; Voegelin et al., 2010) and Ca that can affect phosphate-Fe interactions (Griffioen, 2006; Voegelin et al., 2010).

Phosphate is an essential nutrient with a high affinity for Fe(III). Phosphate uptake by Fe(III)-phases therefore has been extensively studied, for example with respect to phosphate dynamics in eutrophic aquatic systems (Buffle et al., 1989; Gunnars et al., 2002; Griffioen, 2006) or phosphate removal from wastewater (Hsu, 1973; Mao et al., 2012). At near-neutral pH, Fe(II) oxidation in the presence of phosphate leads to the precipitation of amorphous Fe(III)-phosphate in which phosphate limits Fe(III) polymerization to the stage of monomers and oligomers (Rose et al., 1996; Voegelin et al., 2010; Châtellier et al., 2013; Voegelin et al.,

2013). Amorphous Fe(III)-phosphates formed at natural anoxic/oxic boundaries typically also contain Ca (Buffle et al., 1989; Deike et al., 1997; Griffioen, 2006; Och et al., 2012). Effective co-precipitation of phosphate and Ca with Fe(III) has also been documented in laboratory studies (Gunnars et al., 2002; Voegelin et al., 2010; van Genuchten et al., 2014b). These field and laboratory observations have been attributed to electrostatically enhanced co-sorption or ternary complex formation of phosphate and Ca on Fe(III)-(hydr)oxides or precipitation of separate Ca- and Fe(III)- or mixed Ca-Fe(III)-phosphate (Hsu, 1973; Matthiesen et al., 2001; Rietra et al., 2001; Griffioen, 2006). Spectroscopic work indicated that the formation of Ca-containing Fe(III)-phosphate is partly due to structural incorporation of Ca and phosphate into amorphous Ca-Fe(III)-phosphate (Kaegi et al., 2010; Voegelin et al., 2010; van Genuchten et al., 2014a). To date, however, the mode of Ca and phosphate co-precipitation with Fe(III) and its influence on precipitate structure are still not fully understood. Furthermore, although field and laboratory studies indicate that up to ~0.5-1.0 P/Fe can be incorporated into amorphous (Ca-)Fe(III)-phosphate at near-neutral pH (Buffle et al., 1989; Lienemann et al., 1999; Gunnars et al., 2002; Kaegi et al., 2010; Voegelin et al., 2010; van Genuchten et al., 2014a), the maximum phosphate uptake per Fe has not been studied systematically in relation to solution chemistry and precipitate structure. (Note that we use the term “(Ca-)Fe(III)-phosphate” to refer to both (Ca-free) Fe(III)-phosphate and Ca-Fe(III)-phosphate.)

Under conditions where the initial Fe(II) concentration is higher than the amount required for the removal of dissolved phosphate by formation of (Ca-)Fe(III)-phosphate, continuing Fe oxidation and precipitation in the phosphate-depleted solution takes place (Einsele, 1938; Tessenow, 1974; Gunnars et al., 2002; Voegelin et al., 2013; van Genuchten et al., 2014a). The structure of the precipitate forming in phosphate-free solution depends on the dissolved Si/Fe ratio: Mainly poorly-crystalline lepidocrocite forms in silicate-free solution, whereas ferrihydrite-type precipitates dominate at Si/Fe ratios above ~0.2 (Schwertmann and

Thalmann, 1976; Voegelin et al., 2010; van Genuchten et al., 2014b). In a recent study on the dynamics of Fe(III)-precipitate formation during Fe(II) oxidation in near-neutral phosphate-containing Na electrolyte (Voegelin et al., 2013), we showed that, at initial dissolved P/Fe ratios < 0.55 , the initial formation of amorphous Fe(III)-phosphate with a P/Fe ratio ~ 0.55 was followed by its (partial) transformation into a phosphate-rich ferrihydrite-type precipitate with P/Fe ~ 0.25 and concomitant precipitation of lepidocrocite. These observations revealed the highly dynamic nature of Fe(III)-precipitate formation during Fe(II) oxidation in phosphate-containing solutions. The individual and coupled effects of silicate and Ca on sequential Fe(III)-precipitate formation and on the structure of fresh Fe(III)-precipitates formed in phosphate-containing solutions, however, have not been investigated in detail to date.

The goal of this study was to advance the understanding of the formation, composition, and structure of Fe(III)-precipitates formed by the oxidation of dissolved Fe(II) in the presence of phosphate, silicate and Ca. Our specific objectives were to (i) determine the composition and structure of (Ca-)Fe(III)-phosphate precipitates formed at high dissolved P/Fe ratios with special emphasis on the role of Ca and (ii) to identify the interdependent effects of phosphate, silicate and Ca at lower initial dissolved P/Fe ratios on sequential precipitate formation and structure. We investigated Fe(III)-precipitates formed by oxidation of Fe(II) in aerated aqueous solutions in an extensive fractional factorial experiment designed to cover concentration ranges relevant in near-neutral bicarbonate-buffered natural waters and to facilitate the identification of the interdependent effects of phosphate, silicate and Ca. Macroscopic results on precipitate composition were combined with spectroscopic and microscopic information from synchrotron-based X-ray absorption spectroscopy, transmission electron microscopy, Fourier-transform infrared spectroscopy and X-ray diffraction to gain quantitative and mechanistic insight into how phosphate, silicate and Ca interdependently affect Fe(III)-precipitate formation, structure and phosphate uptake.

2. MATERIALS AND METHODS

2.1. Chemicals

All chemicals were reagent grade from Fluka, Merck, or Sigma Aldrich and were used as received. All aqueous solutions were prepared with high-purity doubly deionized (DDI) water (18.2 MΩcm, Milli-Q[®] Element, Millipore).

2.2. Iron precipitation experiments in different background electrolytes

The Fe(III)-precipitates were synthesized at pH 7.0 in six different background electrolytes (Na, Ca, low Ca, Mg, Na+Si and Ca+Si) by oxidation of 0.5 mM Fe(II) at initial molar phosphate/Fe(II) ratios ((P/Fe)_{init}) from 0 to 2 in the initially homogeneous, oxygenated solutions (Table 1). The experiments were carried out in analogy to previous work (Roberts et al., 2004; Voegelin et al., 2010; Voegelin et al., 2013) (see footnote d of Table 1 for examined conditions). Throughout this manuscript, labels for individual treatments are composed of the respective background electrolyte and initial molar P/Fe ratio (e.g., Na 0.05 for experiments performed in Na electrolyte at P/Fe of 0.05).

For experiments in Na background electrolyte, 8 mM NaHCO₃ were dissolved in DDI water and the pH was lowered to 5-6 by purging the solution with CO₂ gas. The pH was then raised to 7.0 (±0.1) by purging with pressurized air to outgas CO₂. The Ca background electrolyte was prepared by stirring a CO₂-saturated suspension containing 4 mM CaCO₃ overnight, resulting in a clear solution with a pH of 5-6, followed by purging with pressurized air until the pH was 7.0 (±0.1). Analogously, low Ca background electrolyte was prepared from 0.5 mM CaCO₃ and 7 mM NaHCO₃, and Mg electrolyte from 4 mM MgO. The silicate-containing electrolytes Na+Si and Ca+Si were prepared by adding 0.5 mM silicate from an alkaline stock solution (100 mM Si from Na₂SiO₃·9H₂O, prepared daily) to the Na and Ca electrolytes. To minimize the formation of silicate polymers, silicate was added to the vigorously stirred and slightly acidic electrolytes after CO₂ purging before raising the pH to

7.0 (Roberts et al., 2004). Although silicate is mainly present as fully protonated silicic acid (H_4SiO_4) at pH 7.0, we use the term silicate throughout this article.

For the synthesis of Fe(III)-precipitates, 200 mL of pH-adjusted background electrolyte were transferred into individual 220-mL PET bottles. Phosphate was added from a pH-neutral stock solution (50 mM P from $\text{NaH}_2\text{PO}_4 \cdot \text{H}_2\text{O}$) to obtain phosphate concentrations from 0 to 1 mM. The experiments were started by adding 0.5 mM Fe(II) from an acidic stock solution (50 mM Fe from $\text{FeSO}_4 \cdot 7\text{H}_2\text{O}$, 1 mM HCl, prepared daily) to initiate Fe oxidation and precipitation. After Fe(II) addition, the solutions were agitated to ensure rapid mixing. Immediately after mixing, samples of the unfiltered suspensions were collected and acidified to 0.65% HNO_3 (Merck, suprapure) for the analysis of total initial concentrations of Fe, P, Si, Na, Ca and Mg by inductively coupled plasma-mass spectrometry (ICP-MS). The bottles were closed to prevent CO_2 outgassing and left for 4 h, with half-hourly remixing by turning the bottles upside down several times. Over time, the initially colorless and clear solutions had turned beige to orange-brown and turbid. Based on the kinetics of homogeneous and autocatalytic oxidation of Fe(II) in bicarbonate-buffered solutions at pH 7.0 (Stumm and Lee, 1961; Tamura et al., 1976; Millero et al., 1987; King, 1998), Fe was assumed to be nearly completely (>99%) oxidized after 4 h reaction time. The final pH was measured in unfiltered suspensions and varied only slightly (± 0.1) from the initial pH of 7.0.

Samples for determination of Fe, P, Si, Na, Ca and Mg concentrations in unfiltered suspensions and filtered solutions (0.1 μm cellulose nitrate) were collected and acidified to 0.65 % HNO_3 (Merck, suprapure) for analysis by ICP-MS. For transmission electron microscopy (TEM), precipitates were collected on TEM grids (Lacey-carbon Cu, Okenshoji Co. LTD, Japan) by depositing 20 μL of precipitate suspension on the grid and using a paper tissue to draw the solution through the grid. The grids were quickly immersed in DDI water to remove soluble salts and subsequently dried in a desiccator. Precipitate samples for analysis by

X-ray absorption spectroscopy (XAS) and Fourier-transform infrared spectroscopy (FTIR) were collected by filtration of the remaining suspension volume through cellulose nitrate filters (0.1 μm). The filters were washed by passing 20 mL of DDI water and drying under a stream of pressurized air. For precipitate analysis with X-ray diffraction (XRD), a second set of experiments in Na and Ca background electrolyte was performed in larger solution volumes (1000 mL) and only for selected P/Fe ratios, otherwise following the described protocol. Precipitate powders and TEM grids were stored in a desiccator until analysis. In all experiments, 7 μM arsenate was spiked to the electrolytes from a neutral stock solution (13.35 mM As(V) from $\text{Na}_2\text{HAsO}_4 \cdot 7\text{H}_2\text{O}$) after adjusting the pH to 7.0. At the resulting low molar As/Fe ratio of 0.014, As was not expected to substantially affect precipitate structure (except in the phosphate-free treatments). Results on the uptake of As by the Fe(III)-precipitates will be published separately.

To examine potential precipitation of calcite or Ca-phosphate, experiments without Fe were performed at 0.15 mM phosphate in Na, Ca, Na+Si and Ca+Si electrolyte, and at 0.5, 0.75, 1, 1.5 and 2 mM phosphate in Ca electrolyte. The experimental procedure followed the protocol described before, but no Fe(II) was added at the start of the experiments. An additional experiment in Ca electrolyte was performed with 0.5 mM phosphate at a low Fe(II) addition of 0.025 mM Fe(II).

Two sets of precipitate samples were digested for the direct determination of the contents of P, Si, Ca, Mg and Fe: (i) Precipitates formed at $(\text{P/Fe})_{\text{init}}$ of ~ 1 , ~ 1.5 and ~ 2 in the Mg and Ca electrolytes and (ii) precipitates formed at $(\text{P/Fe})_{\text{init}}$ of 0.0, 0.1, 0.2 and 0.4 in the Na+Si and Ca+Si electrolytes. Between 5.2 and 13.1 mg of the dried precipitate were dissolved in 10 mL 0.65% HNO_3 . The extracts were diluted as required for analysis by ICP-MS.

2.3. ICP-MS analyses

Acidified unfiltered and filtered samples were diluted with an aqueous 0.65% HNO_3 solution as required for the analysis of Fe, P, Si, Na, Ca and Mg by ICP-MS (Agilent 7500ce). The detection limit (DL) of the ICP-MS for P and Fe were $0.97 \mu\text{g/l}$ ($0.031 \mu\text{mol/l}$) and $0.15 \mu\text{g/l}$ ($0.003 \mu\text{mol/l}$), respectively. The amounts of P, Fe, Si, Ca and Mg in the precipitates (P_{ppt} , Fe_{ppt} , Si_{ppt} , Ca_{ppt} , Mg_{ppt}) were calculated from their concentrations in the initial unfiltered and the final filtered samples. In general, concentrations measured in filtered samples (P_{filt}) were assumed to correspond to dissolved concentrations (P_{soln}).

Due to the near-complete oxidation of Fe(II) and the low solubility of Fe(III), the Fe concentrations in final filtered solutions were expected to fall below the ICP-MS detection limit, which was the case for most treatments. However, low concentrations of Fe were measured in final filtered solutions from the Na and Na+Si treatments, in contrast to the treatments with bivalent Ca or Mg in the electrolyte. These low Fe concentrations were attributed to colloidal Fe in the monovalent Na electrolyte that passed the filter membrane. Therefore, dissolved concentrations of P in Na and Na+Si suspensions were calculated from the concentrations of Fe and P in the filtered solution based on the assumption that the P/Fe ratio of the Fe(III)-colloids that passed the filter membrane was equal to the P/Fe ratio of the Fe(III)-precipitate retained on the filter membrane and that all measured Fe in filtered solutions was colloidal Fe. At low $(\text{P/Fe})_{\text{init}}$ (<0.4) the correction was negligible (only 0-2% of P_{filt} in colloidal form). At high $(\text{P/Fe})_{\text{init}}$ (0.75-2.0), colloidal P accounted for 2-30% of P_{filt} . At the intermediate $(\text{P/Fe})_{\text{init}}$ of 0.5 and 0.6, colloidal P correspond to $\sim 70\%$ of P_{filt} .

2.4. X-ray absorption spectroscopy

2.4.1. Fe K-edge EXAFS spectroscopy

For Fe K-edge extended X-ray absorption fine structure (EXAFS) spectroscopy, appropriate amounts of the air-dried precipitates (equal to 2-4 mg Fe) were mixed with ~ 150

mg cellulose and pressed into 13-mm pellets (resulting in an absorption edge step of ~ 0.5 -1). Measurements at the XAS beamlines at the Angströmquelle Karlsruhe (ANKA, Eggenstein-Leopoldshafen, Germany) and at the Swiss Norwegian Beamline (SNBL) at the European Synchrotron Radiation Facility (ESRF, Grenoble, France) were performed at room temperature in transmission mode using gas-filled ionization chambers for the measurement of incident and transmitted photon intensity. At both beamlines, a double crystal monochromator (DCM) with a pair of Si(1 1 1) crystals was used for monochromatization. The energy was calibrated by setting the first inflection point of the K-shell absorption edge of a Fe foil to 7112 eV. Higher harmonics were rejected by detuning the incident photon beam to 70% (ANKA) and 65% (ESRF) of its maximum intensity.

The reference and sample spectra were processed and analyzed using the software code Athena (Ravel and Newville, 2005) and software from beamline 10.3.2 at the Advanced Light Source (Marcus et al., 2004). The E_0 was fixed at 7128.5 eV. The spectra were normalized by subtracting a first-order polynomial fitted to the data from -100 to -30 eV before the edge and subsequently dividing through a second-order polynomial fitted to the data from 100 to 300 eV above the edge. EXAFS spectra were extracted using the Autobk algorithm ($R_{\text{bkg}} = 0.9$; k -weight = 3; spline k -range 0.5-11.9 \AA^{-1}).

The sample EXAFS spectra were evaluated by linear combination fit (LCF) analysis using five reference spectra (synthetic lepidocrocite (Lp), 2-line ferrihydrite (Fh), ferrihydrite-type precipitate (HFO) with reduced corner-sharing Fe-Fe linkage compared to Fh, amorphous Fe(III)-phosphate (FeP) and natural mitridatite (Mitr)). Details on the synthesis of the reference materials Lp, Fh, HFO and FeP, their Fe K-edge EXAFS spectra, and a discussion of their structure with respect to local Fe coordination have been published previously (Voegelin et al., 2010) (HFO and FeP previously referred to as HFO-Si and Fe4-P4, respectively). Briefly, the reference Lp represents crystalline lepidocrocite. The reference Fh corresponds to 2-line

1 ferrihydrite synthesized according to a standard protocol based on forced Fe(III) hydrolysis. Its
2 spectrum is characterized by a reduced contribution from first-shell Fe-O that reflects the wide
3 spread in Fe-O distances and a second-shell peak dominated by the contributions from edge-
4 and corner-sharing Fe-Fe pairs. The reference HFO was synthesized by forced Fe(III)
5 hydrolysis in the presence of silicate (Si) and contains about 0.6 Si/Fe. It exhibits a similar
6 first-shell Fe-O coordination and similar degree of edge-sharing Fe-Fe linkage as 2-line
7 ferrihydrite, but a lower degree of corner-sharing Fe-Fe linkage (due to silicate). The reference
8 spectra Fh and HFO are similar, but both were required in the LCF analysis to account for
9 variations in the degree of corner-sharing Fe-Fe linkage in the ferrihydrite-type precipitate
10 fractions. Within this study, we use the term “ferrihydrite-type” to describe precipitates whose
11 second-shell coordination falls between the Fh (ferrihydrite) and HFO reference spectra, and
12 only refer to precipitates as “ferrihydrite” if their spectrum is closer to the Fh than HFO
13 reference spectrum. The FeP reference was synthesized by reacting a concentrated Fe(III)
14 solution with an alkaline phosphate solution (final suspension pH 8.2). It represents an
15 amorphous Fe(III)-phosphate with a P/Fe ratio near unity in which Fe(III) monomers and
16 oligomers are connected via coordinated phosphate groups. Together, the reference spectra Fh,
17 HFO and FeP served to represent the average local Fe coordination of Fe in the amorphous to
18 very poorly-crystalline Fe(III)-precipitate fraction, irrespective of whether the precipitates
19 formed in the presence or absence of phosphate and silicate. Mitridatite (Mitr) was included as
20 a fifth reference in the LCF analysis (specimen from Mineralogischer Fachhandel und Versand,
21 Leipzig, Germany; phase identity checked by X-ray diffraction). Mitridatite is a crystalline
22 basic Ca-Fe(III)-phosphate ($\text{Ca}_2\text{Fe}_3(\text{PO}_4)_3\text{O}_2(\text{H}_2\text{O})_3$) in which each Fe(III)O₆-octahedron is
23 linked to 2 edge-sharing Fe at 3.05 Å, to corner-sharing Fe at ~3.44 Å, 2 P at ~3.15 Å, 2 P at
24 ~3.28 Å, and 2 edge-sharing Ca at ~3.43 Å (see electronic Annex (EA); Fig. EA1). A

constrained shell fit based on this average local Fe coordination satisfactorily reproduced the first- and second-shell of the Mitr spectrum (Fig. EA2, Table EA1).

Based on the 5 reference spectra, the sample spectra were first evaluated by LCF over the k -range 2-11 Å⁻¹ using the software code Athena (Ravel and Newville, 2005) and software from beamline 10.3.2 at the Advanced Light Source (Marcus et al., 2004). Starting with the best one-component fit, the number of components n was increased as long as the normalized sum of squared residuals ($\text{NSSR} = \sum(\text{data}_i - \text{fit}_i)^2 / \sum \text{data}_i^2$) of the best $n+1$ -component was at least 10% (relative) lower than the NSSR of the best n -component fit. Individual fractions were constrained to positive values but the sum of all fractions was not constrained. For presentation and further interpretation, the LCF derived fractions were normalized to a sum of 1. In a second step of the Fe K-edge EXAFS data interpretation, the sample spectra were re-analyzed by LCF using endmember spectra derived from the 72 sample spectra (as described in section 3.2.2), following the same general approach as described for the LCF with reference spectra.

2.5. Ca K-edge XANES and EXAFS spectroscopy

For Ca K-edge XAS, reference materials and air-dried precipitates were mixed with cellulose and pressed into 13-mm diameter pellets with a mass of ~40 mg. For concentrated samples, the mass of Ca was adjusted to 1-1.5 mg to obtain an edge-jump around unity in transmission mode. The samples were measured at the XAS beamline at ANKA using the same setup as described for the Fe XAS analyses. The fluorescence signal was recorded with a 5-element solid-state Ge detector. The spectra were aligned by setting the maximum of the white line of apatite to 4051.8 eV. For data processing with the software code Athena (Ravel and Newville, 2005), the E_0 was fixed at 4046 eV. The spectra were normalized by subtracting a first-order polynomial fitted to the data from -60 to -20 eV before E_0 and subsequently dividing through a second-order polynomial fitted to the data from 30 to 300 eV above E_0 . EXAFS spectra were extracted using the Autobk algorithm ($R_{\text{bkg}} = 1.1$; k -weight = 3; spline k -

range 0.0-9.0 Å⁻¹) and Fourier-transformed over the *k*-range 3-8 Å⁻¹ (Kaiser-Bessel window, sill width 2 Å⁻¹). Five references were compared with the precipitate spectra: Calcite (CaCO₃, Sigma), mitridatite (see section 2.4.1), hydroxyapatite (HAP, Ca₅(PO₄)₃(OH), Alfa Aesar), brushite (CaHPO₄·2H₂O, Riedel-de-Haën), and aqueous Ca²⁺ (Ca²⁺_(aq), 200 mM Ca(NO₃)₂).

2.6. X-ray diffraction analysis and Fourier-transform infrared spectroscopy

For X-ray diffraction (XRD) analysis, 30 mg of dried precipitate were suspended in ethanol, transferred on 27-mm diameter low-background Si-slides and allowed to dry. XRD patterns were recorded from 5 to 95° 2-θ with a step-size of 0.017° and a measurement time of 6 h per sample using Co Kα radiation (X'Pert Powder diffractometer with XCellerator detector, PANalytical, Almelo, The Netherlands).

Fourier-transform infrared spectroscopy (FT-IR) was performed on a Biorad FTS 575 C instrument with a liquid N₂-cooled MCT detector and an attenuated total reflectance unit (Harrick Meridian diamond single reflection Split Pea ATR unit). In addition to the reference materials considered for Fe K-edge LCF analysis (HFO, Fh, Lp, FeP, and Mitr; section 2.4.1) the spectra of three Ca-phosphate minerals with varying Ca/P ratios were used for comparison with sample spectra: Brushite (Ca/P 1.00, section 2.5), HAP (Ca/P 1.67; Budenheim, Germany) and β-tricalcium phosphate (β-TCP, Ca₃(PO₄)₂, Ca/P 1.5; Budenheim, Germany).

2.7. Transmission electron microscopy

TEM analysis was performed on a STEM (HD2700Cs, Hitachi, Japan) operated at 200 kV. For image formation a secondary electron (SE) detector and a high-angle annular dark field (HAADF) detector were used. Elemental analysis, including distribution maps, were acquired with DigitalMicrograph (V.1.82, Gatan Inc., CA, USA) using an EDX detector (EDAX, NJ, USA). Signal processing was done using DigitalMicrograph.

2.8. Thermodynamic calculations

Saturation indices for Ca-phosphates and calcite in the background electrolytes were calculated with PHREEQC using the MinteqA2 V4 database (Parkhurst and Appelo, 1999).

3. RESULTS

3.1. Macroscopic results on Fe(III)-precipitate suspensions

3.1.1. Evolution of suspension color during Fe(II) oxidation

The evolution of suspension color during Fe(II) oxidation in the Na, Ca, Na+Si and Ca+Si electrolytes as a function of initial molar dissolved phosphate/Fe(II) ratio ($(P/Fe)_{init}$) and reaction time is shown in Fig. 1. In all electrolytes, the transition from initially colorless solutions to turbid suspensions started immediately after the addition of Fe(II). In the presence of phosphate, the suspensions first turned beige, irrespective of the absence or presence of silicate and Ca, indicating the initial formation of a Fe(III)-phosphate precipitate (Voegelin et al., 2013). After a reaction time that depended on the type of background electrolyte and on $(P/Fe)_{init}$, changes in suspension color to orange (Na, Ca) or brownish (Na+Si, Ca+Si) were observed that indicated the depletion of dissolved phosphate and the subsequent precipitation of other precipitates (Voegelin et al., 2013). The color changes were consistent with subsequent formation of predominantly lepidocrocite (orange) in the absence of silicate and ferrihydrite-like precipitate (brownish) in the presence of silicate (Cornell and Schwertmann, 2003; Voegelin et al., 2010). With increasing $(P/Fe)_{init}$, this transition occurred at later times because more Fe(III) was required to deplete dissolved phosphate. Above $(P/Fe)_{init}$ of 0.5 in the Na and Na+Si electrolytes and 0.75 in the Ca and Ca+Si electrolytes, the suspensions remained beige even after 4 h reaction time, indicating the exclusive formation of Fe(III)-phosphate.

3.1.2. Dissolved phosphate and precipitate composition

Total concentrations of Fe, P, Si, Ca and Mg in the final suspensions (4 h) in general deviated less than 5% from their initial total concentrations (Fig. EA3), suggesting that adsorption of dissolved species or attachment of precipitates at the walls of the PET bottles were not significant.

The final dissolved phosphate fractions in the Fe(III)-precipitate suspensions and the molar P/Fe ratio of the Fe(III)-precipitates ($(P/Fe)_{ppt}$) as function of $(P/Fe)_{init}$ are shown in Fig. 2. In all electrolytes, $(P/Fe)_{ppt}$ closely matched $(P/Fe)_{init}$ up to a specific $(P/Fe)_{init}$ subsequently referred to as critical $(P/Fe)_{crit}$. With increasing $(P/Fe)_{init}$ above $(P/Fe)_{crit}$, the $(P/Fe)_{ppt}$ leveled off (Fig. 2bdf) and dissolved phosphate fractions increased drastically (Fig. 2ace), indicating that the phosphate uptake capacity of the precipitates was exceeded. This transition in phosphate uptake at $(P/Fe)_{crit}$ was paralleled by the transition in precipitate color to beige (Fig. 1) indicative for exclusive (Ca-)Fe(III)-phosphate formation at $(P/Fe)_{init} > (P/Fe)_{crit}$.

In the silicate-free background electrolytes, the fraction of dissolved phosphate also increased with decreasing $(P/Fe)_{init}$ below $(P/Fe)_{crit}$. This trend can be attributed to the immediate onset of precipitate aging after complete Fe(II) oxidation, which results in the release of initially co-precipitated phosphate back into solution (Voegelin et al., 2013). Notably, the resolubilization of phosphate was hardly recognizable when considering dissolved phosphate concentrations rather than fractions (Fig. EA4), because the lower $(P/Fe)_{init}$ at constant Fe concentrations corresponded to lower total phosphate concentrations. In silicate-containing electrolytes, no analogous increase in dissolved phosphate fractions was observed (Fig. 2e), suggesting that silicate effectively slowed down phosphate resolubilization after Fe(II) oxidation. In Fig. 3a, the phosphate uptake by the Fe(III)-precipitates (expressed as $(P/Fe)_{ppt}$) is plotted as a function of dissolved phosphate after 4 h reaction time (P_{soln}). The $(P/Fe)_{ppt}$ sharply increased at very low P_{soln} and rapidly leveled off as P_{soln} started to increase

on a linear scale, indicating the very effective phosphate uptake by fresh Fe(III)-precipitates up to $(P/Fe)_{init} \sim (P/Fe)_{crit}$.

To estimate the $(P/Fe)_{crit}$ for each electrolyte, linear regressions of $(P/Fe)_{ppt}$ versus $(P/Fe)_{init}$ for precipitates formed at $(P/Fe)_{init}$ of ~ 1 , ~ 1.5 and ~ 2 were extrapolated to the condition $(P/Fe)_{ppt} = (P/Fe)_{init}$ which was set equal to $(P/Fe)_{crit}$. The $(P/Fe)_{crit}$ values for all electrolytes are listed in Table 2 and match with the trends observed in Fig. 1 and Fig. 2bdf. Because the experimental $(P/Fe)_{init}$ for individual precipitates formed at $(P/Fe) \geq 1$ varied slightly among the different electrolytes (Tables EA3-5), the linear regressions were also used to calculate the $(P/Fe)_{ppt}$ ratios for an initial dissolved (P/Fe) ratio of 1.50 (referred to as $(P/Fe)_{1.5}$) to facilitate the comparison of (Ca-)Fe(III)-phosphates formed in different background electrolytes (Table 2).

In Fig. 3b, the $(Mg/Fe)_{ppt}$ or $(Ca/Fe)_{ppt}$ ratios of precipitates formed in the Mg, low Ca, Ca and Ca+Si electrolytes at high $(P/Fe)_{init}$ are shown as a function of $(P/Fe)_{ppt}$ (tabulated values and details on their determination are provided in Table EA6). In the Mg electrolyte, the slight increase in $(P/Fe)_{ppt}$ from $(P/Fe)_{init}$ of ~ 1 to ~ 2 was accompanied by a modest increase in $(Mg/Fe)_{ppt}$ from 0.22 to 0.27. The corresponding $(Ca/Fe)_{ppt}$ ratios of precipitates formed in the low Ca electrolyte were somewhat higher (0.36-0.37) but did not indicate an increase from $(P/Fe)_{init}$ of ~ 1 to ~ 2 . In contrast to the Mg and low Ca electrolytes, both the $(P/Fe)_{ppt}$ and $(Ca/Fe)_{ppt}$ of precipitates formed in the Ca and Ca+Si electrolytes increased markedly from $(P/Fe)_{init}$ of ~ 0.75 to ~ 2 (values in Fig. 3b indicate average and standard deviation of replicate experiments, digestions, and pooled data from Ca and Ca+Si electrolytes; $n=3-6$, Table EA6). From the linear regression of the averaged $(Ca/Fe)_{ppt}$ versus $(P/Fe)_{ppt}$ values from the Ca and Ca+Si electrolytes (Fig. 3b), a $(Ca/P)_{ppt}$ of 1.22 could be derived, which pointed to increasing formation of Ca-phosphate with increasing $(P/Fe)_{init}$ in the Ca and Ca+Si electrolytes. In experiments without spiked Fe(II) with 0.15 mM phosphate in Na, Ca, Na+Si, Ca+Si

electrolytes or with 0.5, 0.75, 1 mM phosphate in Ca electrolyte, the Ca and phosphate concentrations in filtered (0.1 μ m) solutions after 4 h reaction time were not detectably different from their initial total concentrations, indicating negligible formation of filterable Ca-phosphate or Ca-carbonate within the 4 h reaction time (not shown). At higher phosphate concentrations of 1.5 and 2 mM in Ca electrolyte and over reaction times of 24 h and longer, however, Ca-phosphate precipitation was observed (not shown). Precipitation of Ca-phosphate within 4 h was also negligible if 0.025 mM Fe(II) were spiked into Ca electrolyte with 0.5 mM phosphate to form potential nucleation sites for Ca-phosphate (not shown). Together, these observations suggested that even at the highest examined $(\text{P/Fe})_{\text{init}}$ of 2 (equal to 1 mM phosphate) in Ca electrolyte (4 mM Ca), removal of dissolved Ca and phosphate within the 4-h reaction period after Fe(II) addition was dominantly driven by co-precipitation with Fe(III). The ratios $(\text{Ca/Fe})_{1.5}$ and $(\text{Mg/Fe})_{1.5}$ for precipitates formed at $(\text{P/Fe})_{\text{init}}$ of 1.5 in the low Ca, Ca, Ca+Si and Mg electrolytes were interpolated from the experimental values determined at $(\text{P/Fe})_{\text{init}}$ of ~ 1 , ~ 1.5 and ~ 2 , in analogy to the $(\text{P/Fe})_{1.5}$ ratios (Table 2; details in Table EA6) and reflect the trends observed in Fig. 3b.

For precipitates formed in Na+Si and Ca+Si electrolytes at $(\text{P/Fe})_{\text{init}}$ of 0, 0.1, 0.2 and 0.4, the molar Ca/Fe, Si/Fe and P/Fe ratios obtained from precipitate digestion are listed in Table 3. The results indicate that phosphate at a $(\text{P/Fe})_{\text{init}}$ of 0.1 did not markedly affect the uptake of silicate and Ca relative to the phosphate-free treatments. At $(\text{P/Fe})_{\text{init}}$ of 0.2 and 0.4, however, phosphate increasingly inhibited silicate uptake and favored Ca co-precipitation.

3.2. Fe K-edge EXAFS analysis of dried precipitates

3.2.1. LCF analysis of the sample spectra using reference spectra

To quantify variations in precipitate structure as a function of solution chemistry with respect to local Fe coordination, the Fe K-edge EXAFS spectra of precipitates from all experiments were first evaluated by LCF analysis using independent reference spectra. The Fe

K-edge EXAFS spectra and the respective Fourier transformed spectra of selected precipitates and of the reference spectra used for LCF analysis are shown in Fig. 4. The selected sample spectra represent the range of spectral features observed in the spectra from all background electrolytes (Fig. EA5). Principal component analysis (PCA) of all 72 sample spectra indicated that at least 4 reference spectra were required to evaluate the experimental data and target testing supported the use of the reference spectra shown in Fig. 4 for the analysis of sample spectra by LCF (section EA6 in EA).

The LCF results for all 72 samples are displayed in Fig. 5 (complete LCF results in Tables EA3-5, reconstructed LCF spectra together with sample spectra in Fig. EA7 in the electronic annex). In general, the trends of the LCF results for the Na, Ca, Na+Si and Ca+Si series (Fig. 5) were consistent with the observed variations in precipitate color (Fig. 1). For precipitates formed in the absence of phosphate (i.e., for $(P/Fe)_{init} = 0$), LCF returned a major fraction of Lp for the silicate-free electrolytes (Na, Ca, Mg, low Ca) and a major fraction of Fh for the silicate-containing electrolytes (Na+Si, Ca+Si). In all electrolytes, i.e., in the absence and presence of silicate, an increase of $(P/Fe)_{init}$ from 0 to $(P/Fe)_{crit}$ resulted in a gradual increase of the LCF-derived Fe(III)-phosphate fraction (FeP + Mitr). For $(P/Fe)_{init} \geq (P/Fe)_{crit}$, LCF analysis indicated near-exclusive formation of Fe(III)-phosphate (Fig. 5).

3.2.2. Identification and characterization of spectral endmembers

The LCF based on the 5 spectra of synthetic (Lp, Fh, HFO, FeP) or natural (Mitr) reference compounds provided a satisfactory representation of all sample EXAFS spectra (Fig. 4, Fig. EA7) and allowed to characterize major trends in local Fe coordination over the range of studied conditions (Fig. 5). However, as will be further detailed in the following subsections, the LCF results also showed that the reference spectra used for LCF did not correspond to the true spectral endmembers of the studied system, i.e., the reference materials were not identical to the structural endmembers. In a next step, we therefore identified and

characterized the spectral and structural endmembers in the set of 72 samples and derived endmember spectra with improved signal-to-noise ratio by averaging respective sample spectra. These endmember spectra were then used to re-analyze the sample spectra by LCF (section 3.2.3).

3.2.2.1 Amorphous (Ca-)Fe(III)-phosphate formed at high $(P/Fe)_{init}$

Principal component analysis of the 18 spectra of Fe(III)-phosphate-type precipitates formed at $(P/Fe)_{init}$ of ~ 1 , ~ 1.5 and ~ 2 revealed the presence of 2 spectral components and target testing based on these two spectral components indicated that the FeP and mitridatite reference spectra were suitable to describe the spectral variability (see section EA6; Fig. EA6). The best LCF of the respective samples from the series without Ca (Na, Na+Si, Mg) included only the FeP spectrum, whereas mitridatite was consistently included in the best LCF of samples from the Ca and Ca+Si electrolytes (Fig. 5). The spectra of samples formed at $(P/Fe)_{init}$ of ~ 1.5 and ~ 2 in the Na and Na+Si electrolytes were almost identical in k - and r -space, and the same was observed within the corresponding set of samples from the Ca and Ca+Si electrolytes (Fig. EA8ab), showing that silicate did not significantly affect Fe coordination at high $(P/Fe)_{init}$.

The endmember spectra FeP* and CaFeP* shown in Fig. 6 were obtained by averaging the spectra Na 1.43, Na 1.95, Na+Si 1.39 and Na+Si 1.84 (for FeP*) and Ca 1.45, Ca 1.91, Ca+Si 1.50 and Ca+Si 1.98 (for CaFeP*), respectively. Their direct comparison revealed differences in k -space (Fig. 6a) that were localized in the region of the second-shell in r -space (Fig. 6b), clearly reflecting differences in local Fe coordination. For the spectrum FeP*, a good fit for the second-shell region was achieved with the FeP reference alone (Fig. 6; Table 4). In contrast, the spectrum CaFeP* was not adequately described by FeP alone (NSSR 7.8×10^{-3}) and a substantially better fit with 49% lower NSSR was obtained when the mitridatite reference was included (Fig. 6; Table 4). To further ascertain and interpret this result, the

second-shell signal of the spectra FeP*, CaFeP* and Mitr are compared to each other in Fig. 7ade. Both the magnitude and imaginary parts of the spectra FeP* and CaFeP* exhibit differences that are in line with a mitridatite-component in the spectrum CaFeP*. Furthermore, the imaginary parts over the second-shell r -range from 2.3-3.4 Å and the corresponding back-transformed spectra over the k -range 2-11 Å⁻¹ exhibit isosbestic behavior, with the CaFeP* spectrum in-between the FeP* and Mitr spectra, indicating that the mitridatite reference provided a very accurate description of the changes in local Fe coordination induced by Ca.

The average spectrum MgFeP* (Mg 1.46; Mg 1.87, Fig. EA8) closely resembled the FeP* spectrum (Fig. 6). The average spectrum lowCaFeP* (low Ca 1.45, low Ca 2.00, Fig. EA8) on the other hand could be perfectly described as a linear combination of 0.60×FeP* + 0.40×CaFeP* (Fig. 6, Table 4). Considering the LCF results for the spectra CaFeP* and FeP* (Table 4), the LCF of the spectrum lowCaFeP* based on the spectra Fe* and CaFeP* corresponded to a fit with 0.06×Mittr + 0.94×FeP. The finding that the spectra FeP* and CaFeP* allowed to reproduce the spectra MgFeP* and lowCaFeP* showed that they represent the spectral endmembers for Fe(III)-phosphate-type precipitates in all studied electrolytes.

3.2.2.2 Poorly crystalline lepidocrocite

In the silicate-free electrolytes (Na, Ca, low Ca, Mg), the EXAFS spectra of Fe(III)-precipitates formed in the absence of phosphate were described by LCF as a combination of a major fraction (63-70%) of Lp and a minor fraction of Fh+HFO (Fig. 5). In an earlier study on precipitates formed in Na electrolyte (Voegelin et al., 2013), we concluded from XRD and TEM data that an analogous LCF result reflected the formation of poorly crystalline lepidocrocite rather than the formation of a mixture of crystalline lepidocrocite and ferrihydrite. This interpretation was supported by the results from a recent study in which total X-ray scattering data collected on analogous precipitates was shown to match with simulations for poorly crystalline (turbostratic) lepidocrocite but not with simulations for mixtures of

crystalline lepidocrocite and ferrihydrite (van Genuchten et al., 2014b). The endmember spectrum pcLp* was therefore calculated from the sample spectra Na 0.00, Ca 0.00, Mg 0.00 and low Ca 0.00 (Fig. EA8; Fig. 6cd) and was considered to represent the poorly crystalline lepidocrocite in our sample set. Comparison of this spectrum to the spectrum Lp (Fig. 7b) clearly reveals the reduced amplitudes of the second and higher shells.

3.2.2.3 Silicate-containing ferrihydrite

For the silicate-containing electrolytes Na+Si and Ca+Si, the LCF analysis of the two precipitates formed in the absence of phosphate (Na+Si 0.00 / Ca+Si 0.00) returned a major fraction of Fh (67% / 49%) and minor fractions of HFO (0% / 23%) and FeP (33% / 28%). These LCF results indicated that the ferrihydrite-type precipitate with $(\text{Si/Fe})_{\text{ppt}} \sim 0.1$ formed in the absence of phosphate exhibited a significantly lower degree of corner-sharing Fe(III) polymerization than the 2-line ferrihydrite reference (Fh). This has previously been observed for ferrihydrite-type precipitates formed by Fe(II) oxidation in silicate-containing solution (Voegelin et al., 2010; van Genuchten et al., 2014b), and total X-ray scattering data for such a ferrihydrite-type precipitate suggested that the reduced corner-sharing Fe-Fe linkage goes along with a significant reduction in the coherently scattering domain size relative to 2-line ferrihydrite (van Genuchten et al., 2014b). As an endmember spectrum for silicate-containing ferrihydrite forming in the silicate-containing Na+Si and Ca+Si electrolytes, we calculated the average spectrum Fh-Si* (Na+Si 0.00, Ca+Si 0.00; Fig. 6cd, Fig. 7c, Fig. EA8) Comparison of the spectrum Fh-Si* to the spectra Fh, HFO and FeP shows a first-shell amplitude between HFO and FeP and a second-shell signal intermediate between Fh and HFO with respect to corner-sharing Fe-Fe linkage (Fig. 7c), which resulted in the inclusion of all 3 references in the LCF of the spectrum Fh-Si* (Table 4).

3.2.2.4 Ferrihydrite-type precipitate formed by Fe(III)-phosphate transformation

In addition to the four endmember spectra derived above, an additional spectrum was required to account for the ferrihydrite-type precipitate formed by the transformation of initially precipitated (Ca-)Fe(III)-phosphate during continuing Fe(II) oxidation in phosphate-depleted silicate-free electrolytes with $(P/Fe)_{init} < (P/Fe)_{crit}$ (Voegelin et al., 2013). This spectrum could not be isolated from individual sample spectra, but preliminary LCF analysis of the six spectra of precipitates formed in the Na and Ca electrolytes at $(P/Fe)_{init}$ of ~ 0.2 , ~ 0.3 , and ~ 0.4 using the respective endmember spectra FeP* or CaFeP* and pcLp* indicated that this transformation product was best represented by the HFO spectrum (rather than the Fh spectrum, calculated spectra corresponding to HFO/Fh mixtures with ratios from 90/10 to 10/90, or the Fh-Si* endmember spectrum). For the six tested samples, inclusion of the HFO spectrum reduced the NSSR by 30-65% relative to the LCF with the respective endmember spectra alone and visually improved the fits in the second-shell region (not shown).

3.2.3. Quantification of distinct precipitate fractions and their P/Fe ratios

As described in the preceding sections, the endmember spectra derived from the sample spectra offered a better spectral representation of the different structural endmembers in our sample set than the reference spectra used to characterize local Fe coordination. To quantify the different precipitate fractions, the sample spectra were therefore reanalyzed by LCF using the endmember spectra. As indicated in Table 4, only the two endmember spectra were required to analyze the samples from the Na+Si and Ca+Si electrolytes. In the case of the Na, Mg, and Ca electrolytes, the two endmember spectra and the HFO reference were used for data analysis. In the case of the low Ca series, we used the spectrum lowCaFeP* (which corresponds to a linear combination of the endmember spectra FeP* and CaFeP*, Table 4, Fig. 6) to represent the Ca-Fe(III)-phosphate fraction. The detailed LCF results for individual

samples are provided in the electronic annex (Tables EA3-5; Fig. EA9). The LCF-derived endmember fractions interpolated over $(P/Fe)_{init}$ are shown in Fig. 8.

Based on the precipitate P/Fe ratios of precipitates formed at $(P/Fe)_{init}$ of 0.2 to 0.75 (Fig. 2bdf) and the fractions pcLp*, HFO or Fh-Si* and FeP*, CaFeP* or lowCaFeP* (Fig. 8, Tables EA3-5), the specific P/Fe ratios of poorly-crystalline lepidocrocite (in silicate-free electrolytes), the ferrihydrite-type precipitate fraction, and (Ca-)Fe(III)-phosphate in each electrolyte were derived by multiple linear regressions (Table 2, $R^2 \geq 0.990$ for all series, regression equations EA1 and EA2 in section EA11; results in Fig EA11). Because multiple linear regressions for the silicate-free series consistently returned a P/Fe ratio for pcLp* of 0 (constrained lower limit) and because pcLp* was absent in precipitates formed in silicate-containing electrolytes, only the P/Fe ratios of the Fe(III)-phosphate (FeP*, CaFeP*, or lowCaFeP*) and ferrihydrite-type (HFO or Fh-Si*) precipitate fractions are listed in Table 2.

3.3. XRD patterns, Ca K-edge XAS and FTIR spectra of selected precipitates

3.3.1. X-ray diffraction patterns

The XRD patterns of Fe(III)-precipitates formed in Na and Ca electrolyte are shown in Fig. 9. For precipitates formed in the absence of phosphate, the XRD patterns indicated the formation of poorly-crystalline lepidocrocite, in line with earlier work on precipitate formation in (synthetic) natural waters (Schwertmann et al., 1984; Voegelin et al., 2010; van Genuchten et al., 2014b). Coherent scattering domain sizes of 24 nm (Na 0.00) and 22 nm (Ca 0.00) were estimated from the 200 peak (Scherrer equation), indicating that individual lepidocrocite crystals consisted of only few stacked sheets, as shown in earlier work (Schwertmann and Taylor, 1979; Cumplido et al., 2000; Voegelin et al., 2013; van Genuchten et al., 2014b). No goethite was detected by XRD in the phosphate-free precipitates, in line with preliminary LCF analyses including a goethite reference spectrum (not shown). For 1 mM Fe(II) oxidized in Na electrolyte, we previously observed the formation of a minor fraction of goethite in phosphate-

free electrolyte and effective inhibition of goethite formation at $(\text{P/Fe})_{\text{init}}$ of 0.03 (Voegelin et al., 2013). In the present study, the presence of 0.014 As(V)/Fe thus most probably inhibited goethite formation in the absence of phosphate and silicate. With increasing $(\text{P/Fe})_{\text{init}}$, the amplitude of the Lp peaks decreased and a broad peak characteristic for amorphous Fe(III)-phosphate (Thibault et al., 2009; Voegelin et al., 2013) appeared. In Na electrolyte, only the broad Fe(III)-phosphate peak was detected for $(\text{P/Fe})_{\text{init}} \geq 0.48$, whereas minor contributions of Lp were still visible in the sample Ca 0.51, in agreement with EXAFS results (Fig. 4 and Fig. 5). The XRD patterns of the samples Ca 0.78 and Ca 1.47 did not reveal any sharp peaks, indicating that no crystalline Ca-phosphate or Ca-Fe(III)-phosphate had formed.

3.3.2. *Ca K-edge XANES and EXAFS spectra*

In Fig. 10a, the first-derivative Ca K-edge XANES spectra of precipitates formed in the Ca and Ca+Si electrolytes at $(\text{P/Fe})_{\text{init}}$ of 0 and 1.50 are shown in comparison to reference spectra. The spectra Ca 0.00 and Ca 1.45 closely matched the spectra Ca+Si 0.00 and Ca+Si 1.50, respectively, suggesting that silicate had a minor impact on Ca coordination. Comparison of the sample and reference spectra suggested that neither hydroxyapatite nor mitridatite represented the dominant fraction of the co-precipitated Ca and allowed to exclude the formation of calcite. The spectra of the samples Ca 0.00 and Ca+Si 0.00 compared well with the reference spectrum of aqueous Ca^{2+} , suggesting that Ca in the absence of phosphate was mainly sorbed as hydrated cation. The spectral difference between the samples formed at $(\text{P/Fe})_{\text{init}}$ of 0 and 1.5, on the other hand indicated that phosphate caused changes in the mode of Ca uptake. In Fig. 10bc, the Fourier-transformed EXAFS spectra of the samples Ca+Si 0.00 and Ca 1.45 are compared to reference spectra. The two sample spectra did not exhibit a marked second shell signal, and comparison with the reference spectra of mitridatite and apatite clearly showed that these crystalline phases could not account for a major fraction of total Ca. The spectrum of the sample Ca+Si 0.00 on the other hand was similar to the spectrum

of aqueous Ca^{2+} , supporting the interpretation of the first-derivative XANES spectra that Ca in the absence of phosphate was mainly sorbed as hydrated cation. The spectrum Ca 1.45 in contrast exhibited a significantly lower first-shell peak with an amplitude similar to brushite ($\text{CaHPO}_4 \times 2\text{H}_2\text{O}$; 8-fold O-coordinated Ca polyhedra sharing 2 edges with 2 neighboring Ca polyhedra and 2 edges and 2 corners with 4 phosphate groups (Schofield et al., 2004)) or a 2:1 combination of the HAP and aqueous Ca^{2+} reference spectra. This suggested that co-precipitated Ca in the presence of high phosphate levels exhibited (at least partially) a Ca-phosphate-like local coordination, which may involve Ca-Ca and Ca-P linkage. Phosphate-Ca coordination in amorphous Ca-Fe(III)-phosphate has previously been identified by P K-edge XANES spectroscopy (Voegelin et al., 2010).

3.3.3. *Fourier-transform infrared spectra*

In general, the FTIR spectra of selected samples from the Na, Na+Si, Ca, and Ca+Si series revealed spectral features that were in line with the trends derived from Fe K-edge XAS and XRD analyses (see section EA13, Fig. EA13). In Fig. 11, the spectra of the samples Na+Si 1.39 and Ca+Si 1.50, i.e., of precipitates formed at high $(\text{P/Fe})_{\text{init}}$ in the absence and presence of Ca, are compared to selected reference spectra. The sample formed in the presence of Ca exhibited additional peaks in the regions from $500\text{-}600\text{ cm}^{-1}$ and $900\text{-}1150\text{ cm}^{-1}$, most probably from Ca-coordinated phosphate. Compared with the reference spectra of HAP, mitridatite, brushite, and β -TCP, the positions of the additional peaks most closely matched the spectrum of β -TCP. However, the additional peaks were much broader, indicating that they arise from an amorphous or highly disordered phase.

3.4. **Transmission electron microscopy**

Secondary electron (SE) images of selected precipitates that cover the observed range of precipitate morphologies are shown in Fig. 12, (corresponding high angle annular dark field (HAADF) images in Fig. EA14). In the absence of phosphate and silicate in Na and Ca

electrolyte (Fig. 12ab), the precipitates consisted of thin aggregated lepidocrocite platelets in line with earlier studies (Sahai et al., 2007; Kaegi et al., 2010; Voegelin et al., 2013). (Ca-)Fe(III)-phosphate-type precipitates formed at $(P/Fe)_{init}$ well above $(P/Fe)_{crit}$, on the other hand, consisted of spherical particles with smooth surfaces (Fig. 12gh), as observed previously (Kaegi et al., 2010; Voegelin et al., 2013). Examination of the precipitate Ca 1.47 at higher magnification did not provide any evidence for the existence of separate Ca-phosphate and Fe(III)-phosphate precipitates or the formation of crystalline mitridatite or another crystalline Ca-Fe(III)-phosphate within this sample (Fig. EA15). The precipitate formed in Na electrolyte at $(P/Fe)_{init}$ of 0.49 (close to $(P/Fe)_{crit}$, Table 2) resembled the precipitate formed at $(P/Fe)_{init}$ of 1.95 (Fig. 12dg). In contrast, the precipitate formed in Ca electrolyte at a $(P/Fe)_{init}$ 0.50 consisted of smooth spherical Ca-Fe(III)-phosphate particles covered with lepidocrocite platelets (Fig. 12e), indicating sequential precipitate formation at $(P/Fe)_{init} < (P/Fe)_{crit}$ as previously observed in Na electrolyte (Kaegi et al., 2010; Voegelin et al., 2013).

The precipitate formed in the absence of phosphate in the Ca+Si electrolyte consisted of spherical particles with coarser surface, suggesting that it consisted of aggregated ferrihydrite-type crystallites (Kaegi et al., 2010). The precipitate formed at $(P/Fe)_{init}$ of 0.19 in the same electrolyte also consisted of spherical particles with a similar surface structure as the precipitate formed in the phosphate-free electrolyte (Fig. 12cf). This indicated that the surface of the particles also consisted of aggregated ferrihydrite-type crystallites, rather than amorphous Ca-Fe(III)-phosphate that formed first (Fig. 1). Elemental distribution maps of the precipitate Ca+Si 0.19 were recorded to reveal the internal structure of the precipitates (Fig. 13). The Ca and P signal intensities were well correlated in the interior of individual particles (Fig. 13cf) and the Si signal intensities were higher in the outer zones of the spherical particles (Fig. 13e). This spatially heterogeneous element distribution is further evidenced by the tricolor Fe-P-Si map (Fig. 13d).

4. DISCUSSION

The complementary macroscopic, spectroscopic and microscopic results from this study indicated that Fe(III)-precipitate formation, structure and phosphate uptake markedly differed between initial dissolved P/Fe ratios above and below the critical P/Fe ratio of the individual electrolytes (Table 2). At $(P/Fe)_{init} > (P/Fe)_{crit}$, the oxidation of Fe(II) led to nearly exclusive formation of amorphous (Ca-)Fe(III)-phosphate precipitates whose structure was affected by the presence of Ca, and phosphate removal was limited by the uptake capacity of the amorphous (Ca-)Fe-phosphate precipitate. At $(P/Fe)_{init} < (P/Fe)_{crit}$, however, the precipitation of (Ca-)Fe(III)-phosphate was followed by ongoing Fe oxidation in the phosphate-depleted solution, and silicate influenced the phosphate uptake and the structure of the precipitates. In the following two sections, precipitate formation and phosphate uptake will therefore be separately discussed for $(P/Fe)_{init}$ above and below $(P/Fe)_{crit}$.

4.1. Amorphous (Ca-)Fe(III)-phosphate formed at $(P/Fe)_{init} > (P/Fe)_{crit}$

For $(P/Fe)_{init} > (P/Fe)_{crit}$, the evolution of precipitate color (Fig. 1) and Fe K-edge XAS (Fig. 5), XRD (Fig. 9) and STEM data (Fig. 12) revealed nearly exclusive formation of (Ca-)Fe(III)-phosphate over the course of Fe(II) oxidation. In this section, the structure and phosphate uptake of these precipitates is discussed with an emphasis on the role of Ca. Silicate is not considered here as it did not influence precipitate formation at $(P/Fe)_{init} > (P/Fe)_{crit}$.

4.1.1. Amorphous Fe(III)-phosphate formed in Ca-free electrolytes

In the Na and Na+Si electrolytes, $(P/Fe)_{crit}$ of 0.52-0.53 were observed (Table 2), in agreement with a $(P/Fe)_{crit}$ of 0.55 recently reported for precipitates formed under analogous conditions at 2-fold higher Fe concentration (Voegelin et al., 2013). For $(P/Fe)_{init} > (P/Fe)_{crit}$, the concentration of dissolved phosphate drastically increased with increasing $(P/Fe)_{init}$, suggesting that the phosphate uptake capacity of the precipitate was reached. Nevertheless, the

(P/Fe)_{ppt} still increased slightly to 0.61-0.63 at (P/Fe)_{init} of 1.5 ((P/Fe)_{1.5} in Table 2) and to 0.68 (Na) and 0.63 (Na+Si) at (P/Fe)_{init} of 1.95 and 1.84, respectively (Tables EA3 and EA5). These trends suggest that the phosphate uptake capacity of amorphous Fe(III)-phosphate formed by Fe(II) oxidation at near-neutral pH in Na-electrolyte at (P/Fe)_{soln} >> (P/Fe)_{crit} is close to 2/3, which corresponds to the P/Fe ratio of vivianite and its amorphous oxidation product santabarbarite (Pratesi et al., 2003). Due to competition between Fe(III) complexation with phosphate and Fe(III) hydrolysis, the (P/Fe)_{ppt} of amorphous Fe(III)-phosphate increases with decreasing pH (Hsu, 1973; Hsu, 1982). Considering this trend, an uptake capacity of ~2/3 P/Fe at pH 7.0 falls in line with a (P/Fe)_{ppt} ~0.42 for amorphous Fe(III)-phosphate formed at pH 7.5 by 0.5 mM Fe(II) in Na electrolyte containing 0.5 mM phosphate (van Genuchten et al., 2014b), a maximum (P/Fe)_{ppt} of ~0.49 for amorphous Fe(III)-phosphate formed at pH 7.2 by oxidation of 0.032 mM Fe(II) in K/Na electrolyte with (P/Fe)_{init} of 3 (Tessenow, 1974), a maximum (P/Fe)_{ppt} of 0.86 for amorphous Fe(III)-phosphate formed at pH 6.0 by Fe(II) oxidation in Na electrolyte with (P/Fe)_{init} of 3 (Châtellier et al., 2013) and a (P/Fe)_{ppt} of unity for amorphous Fe(III)-phosphate formed at pH ≤ 2 from a concentrated Fe(III) solution with (P/Fe)_{init} of 1.5 (Mikutta et al., 2014).

For this latter amorphous Fe(III)-phosphate formed at low pH, Mikutta et al. (2014) concluded from Fe K-edge EXAFS, Mössbauer spectroscopy, and total X-ray scattering data, that monomeric Fe(III) was 4-fold coordinated with phosphate (Fe-P distance ~3.25 Å) as in strengite (Fig. 14) and that Fe-Fe pairs were absent. The absence of Fe-Fe pairs can be attributed to the low synthesis pH and the P/Fe ratio >1 in the starting solution. A higher pH during precipitate formation, however as in the case of Fe(III)-precipitates formed in bicarbonate-buffered solutions at near-neutral pH, is expected to promote Fe(III) hydrolysis and polymerization and to concomitantly reduce phosphate uptake (Hsu, 1973; Hsu, 1982). The maximum P/Fe ratio of ~2/3 P/Fe observed for amorphous basic Fe(III)-phosphate in the

Na and Na+Si electrolytes thus indicated the presence of Fe oligomers. The structure of crystalline basic Fe(II/III)-phosphates with P/Fe of 2/3 may serve as a model for Fe-Fe coordination in amorphous basic Fe(III)-phosphate oligomers: Metavivianite (Dormann et al., 1982), is built from Fe monomers and edge-sharing dimers that are linked via corner-sharing phosphate groups (average edge-sharing Fe coordination number of 0.67), and ferristrunzite (Peacor et al., 1987) consists of Fe monomers and corner-sharing Fe-chains (average corner-sharing Fe coordination number of 1.5). Edge- and corner-sharing Fe(III) dimers with Fe-Fe distances of ~ 3.0 and ~ 3.6 Å derived from these minerals represent the most elementary representations of Fe oligomers in amorphous Fe(III)-phosphate (and related bridging phosphate coordination) (Fig. 14bc). For Fe(III)-polymers formed by neutralization of concentrated Fe(III) solution at P/Fe of 0.5, Fe-Fe linkage has been suggested to be limited to the stage of edge-sharing dimers based on Fe and P K-edge XAS data (Rose et al., 1996; Rose et al., 1997). Fe K-edge EXAFS results for amorphous Fe(III)-phosphate formed at pH 8.2 (FeP used as reference in the present study) (Voegelin et al., 2010) and more recently for amorphous Fe(III)-phosphate formed at pH 6.0 (Châtellier et al., 2013) point to Fe-Fe linkage in amorphous basic Fe(III)-phosphate (in analogy to amorphous basic Fe(III)-arsenate (Inskeep et al., 2004; Paktunc et al., 2008)), but also suggest that the extent of Fe polymerization in amorphous basic Fe(III)-phosphate is limited to the oligomeric stage.

Amorphous Fe(III)-phosphate formed in the Mg electrolyte exhibited slightly higher values for $(P/Fe)_{\text{crit}}$ and $(P/Fe)_{1.5}$ than Fe(III)-phosphate formed in the Na and Na+Si electrolytes (Table 2), in agreement with more effective phosphate removal reported for Fe oxidation products formed in $MgCl_2$ than NaCl electrolyte (van Genuchten et al., 2014b). From this latter study, a $(P/Fe)_{\text{ppt}}$ of ~ 0.7 was derived for Fe(III)-phosphate formed by oxidation of 0.5 mM Fe(II) at pH 7.5 in solution containing 1 mM $MgCl_2$ and 0.5 mM phosphate, which compared well to the $(P/Fe)_{1.5}$ of 0.71 found for the Mg electrolyte (Table 2). This $(P/Fe)_{1.5}$ is

close to the uptake capacity of $\sim 2/3$ P/Fe inferred for Fe(III)-phosphate formed in the Na and Na+Si electrolytes, as also evidenced by the plot of $(\text{P/Fe})_{\text{ppt}}$ versus P_{soln} in Fig. 3a. Furthermore, the nearly identical Fe K-edge XAS spectra MgFeP^* and FeP^* (Fig. 6) indicated that Mg did not markedly affect the degree of Fe polymerization. In combination, these results suggested that Mg promoted phosphate uptake relative to Na predominantly through favorable electrostatic interactions, but did not detectably change the structure (local Fe coordination) or enhance the phosphate uptake capacity of the Fe(III)-phosphate.

4.1.2. Amorphous Ca-Fe(III)-phosphate formed in Ca-containing electrolytes

The $(\text{P/Fe})_{\text{crit}}$ and $(\text{P/Fe})_{1.5}$ of the Ca-Fe(III)-phosphate formed in the Ca and Ca+Si electrolytes were significantly higher than the respective values of Fe(III)-phosphate formed in the Na and Na+Si electrolytes (Table 2). Phosphate uptake in the Ca electrolyte was also markedly higher than in the Mg electrolyte and also the $(\text{Ca/Fe})_{\text{ppt}}$ ratio increased to much higher values than the $(\text{Mg/Fe})_{\text{ppt}}$ ratio (Fig. 3b), as also evidenced by the respective $(\text{Ca/Fe})_{1.5}$ and $(\text{Mg/Fe})_{1.5}$ ratios (Table 2). These differences suggested that specific interactions between Ca and phosphate in addition to electrostatically favored co-precipitation contributed to enhanced Ca and phosphate uptake. As will be discussed in the following subsections, this may be attributed to Ca-induced formation of mitridatite-like Ca-Fe(III)-phosphate polymers and Ca-phosphate polymers in addition to Ca-containing Fe(III)-phosphate polymers with the same local Fe coordination as the amorphous Fe(III)-phosphate formed in Ca-free electrolytes.

4.1.2.1 Mitridatite-like Ca-Fe(III)-phosphate polymers (LCF fraction “Mitr”)

The difference between the EXAFS spectra CaFeP^* and FeP^* showed that Ca influenced the local Fe coordination in amorphous (Ca-)Fe(III)-phosphate, and the mitridatite reference spectrum provided a nearly perfect description of the spectral difference (Fig. 6, Fig. 7). Characterization of Ca-Fe(III)-phosphate formed in Ca electrolyte at $(\text{P/Fe})_{\text{init}} \sim 1.5$ by XRD (Fig. 9) and STEM (Fig. EA15) on the other hand allowed to exclude the formation of a

substantial fraction of crystalline Ca- or Ca-Fe(III)-phosphate. These findings are in line with total X-ray scattering data for a Ca-Fe(III)-phosphate formed under similar conditions and with similar composition (Ca/Fe=0.7, P/Fe=0.94) which indicated a coherently scattering domain size (CSD) <1 nm (van Genuchten et al., 2014a). Considering these results, the LCF-derived fraction of 15% Mitr in the spectrum CaFeP* (Table 4) was attributed to the formation of Ca-Fe(III)-phosphate polymers with mitridatite-like local coordination.

Mitridatite is a layered basic Ca-Fe(III)-phosphate built from octahedral Fe(III) sheets of interconnected triangular Fe(III) nonamers to which phosphate and Ca are bound (Moore and Araki, 1977) (Fig. EA1). The two trimeric Fe(III) units corresponding to the corner of a nonamer (Fig. 14d-f) or the contact between two nonamers (Fig. 14g-i) represent the smallest possible oligomers with mitridatite-like local Fe coordination, and could form by monomer attachment to a Fe(III) dimer. The 3 Fe atoms are bridged by double- and triple-corner sharing phosphate groups and edge-sharing Ca. Mitridatite-like Fe coordination was only observed in Ca-containing electrolytes, indicating that edge-sharing Ca is essential for the stabilization of mitridatite-like polymers. As a structural motif, the octahedral sheet of mitridatite also features an Fe(III) hexamer consisting of three edge-sharing Fe(III) dimers that are linked via corners (Moore and Araki, 1977) (Fig. EA1). A hypothetical Ca-Fe(III)-phosphate polymer based on this Fe(III) hexamer is shown in Fig. 14j-l. The basic structure of this polymer conforms with the structure of polyoxometalate ions with the general formula $[P_4M_6O_{34}]^{12-}$ ($M=W^{VI}$ or Mo^{VI}) studied in materials research (Ritchie et al., 2009; Wang et al., 2009; Niu et al., 2011) and it is conceivable that this polymer could readily form via Ca-induced linkage of edge-sharing dimers (Fig. 14b). The two Fe(III) trimers (Fig. 14d-i) and the Fe(III) hexamer (Fig. 14j-l) shown in Fig. 14 represent probable models of mitridatite-like polymers in amorphous Ca-Fe(III)-phosphate. However, these shown polymers are hypothetical, and other polymers with mitridatite-like local coordination could form as well.

Evaluation of the spectrum lowCaFeP* of Ca-Fe(III)-phosphate formed in the low Ca electrolyte with 0.5 mM Ca revealed a mitridatite-like Fe fraction of 6%, compared to 15% in Ca-Fe(III)-phosphate formed in the Ca/Ca+Si electrolytes with 4 mM Ca (section 3.2.2.1). Mitridatite-like Fe coordination thus increased with increasing Ca at constant phosphate and Fe concentration. To examine the dependence of mitridatite-like Ca-Fe(III)-phosphate formation on the initial Fe and phosphate concentration, we re-evaluated the spectrum of a Ca-Fe(III)-phosphate precipitate (Fe2-sGW) studied previously (Kaegi et al., 2010; Voegelin et al., 2010). This sample had been synthesized at a 14-times lower Fe concentration than used in the current work at $(P/Fe)_{init}$ of 1.8 (Ca/Mg+Si electrolyte bicarbonate-buffered to pH 7.0 with 2.5 mM Ca, 1.5 mM Mg, 0.71 mM silicate, 0.036 mM Fe, and 0.065 mM phosphate). Its spectrum perfectly matched the spectrum CaFeP* (Fig. EA10), showing that the fraction of mitridatite-like Fe depended mainly on the concentration of Ca. Considering that a mitridatite-like Fe fraction of 6% was inferred for the lowCaFeP* spectrum (0.5 mM Ca; section 3.2.2.1) and assuming a linear increase of the mitridatite-like Fe fraction with Ca concentration, a mitridatite-like Fe fraction of 15% as inferred for the sample Fe2-sGW (2.5 mM Ca) and the CaFeP* spectrum (4 mM Ca) would be reached at ~1.25 mM Ca. This suggests that the fraction of mitridatite-like Fe increases up to a certain Ca level, but remains constant at higher Ca concentrations.

With regard to the fraction of Fe in mitridatite-like polymers derived from LCF results, it should be noted that the coordination numbers (CN) of edge-and corner-sharing Fe in a 50:50 mixture of the two mitridatite-like trimers (Fig. 14d-f; Fig. 14g-i) or in the Fe hexamer (Fig. 14j-l) (CN=1 for edge- and corner-sharing linkage) correspond to only half their values in crystalline mitridatite (CN=2; section EA1). Since the mitridatite reference spectrum mainly accounted for spectral differences in the second shell (Fig. 6, Fig. 7), the effective fraction of Fe in mitridatite-like Ca-Fe(III)-phosphate polymers may be up to factor two higher than

indicated by the LCF-derived mitridatite fraction. Thus, assuming that the fraction of Fe in mitridatite-like polymers in Ca-Fe(III)-phosphate in the Ca and Ca+Si electrolytes ranged between 15-30% and that these polymers on average exhibited the same P/Fe and Ca/Fe ratios as crystalline mitridatite (2/3 and 1, respectively), about 15-30% of the total phosphate and 14-29% of the total Ca in the precipitate formed at $(P/Fe)_{init}$ of 1.5 in the Ca and Ca+Si electrolytes were tentatively estimated to be associated with mitridatite-like polymers (Table EA7). A spectral contribution from 14% Ca in mitridatite was around the detection limit of Ca K-edge XAS (Fig. 10b). Furthermore, Ca in mitridatite-like polymers may exhibit a less intense second-shell signal than Ca in mitridatite (lower coordination numbers, higher disorder). Thus, the Ca XAS data did not allow to confirm or exclude the incorporation of up to 29% Ca in mitridatite-like polymers, but suggested that the fraction mitridatite-like polymers probably did not substantially exceed the upper estimate derived from Fe K-edge LCF results.

4.1.2.2 Amorphous Fe(III)-phosphate-like Ca-Fe(III)-polymers (LCF fraction “FeP”)

The LCF-analysis of the spectrum CaFeP* suggested that the major fraction of 85-70% of the total Fe exhibited a similar degree of Fe polymerization as in the Na, Na+Si and Mg electrolytes (up to 15% of the LCF-derived FeP fraction together with 155 Mitr may represent mitridatite-like polymers). This in turn suggested that the P/Fe ratio of this Fe fraction may not significantly exceed the highest $(P/Fe)_{1.5}$ of Fe(III)-phosphate formed in the Ca-free electrolytes. In a recent study investigating amorphous Ca-Fe(III)-phosphate with a composition (Ca/Fe=0.70, P/Fe=0.94) closely matching the $(Ca/Fe)_{1.5}$ and $(P/Fe)_{1.5}$ of Ca-Fe(III)phosphate formed in the Ca and Ca+Si electrolytes (Table 2), 0.22 Ca/Fe (and no phosphate) was found to be extractable by 1 M NaCl (van Genuchten et al., 2014a). This ratio is remarkably similar to the $(Mg/Fe)_{1.5}$ of 0.25 of Fe(III)-phosphate formed in the Mg electrolyte, supporting the notion that a similar amount of Ca as Mg can be taken up by the FeP-fraction of the Ca-Fe(III)-phosphate. We therefore considered the $(Mg/Fe)_{1.5}$ and $(P/Fe)_{1.5}$

of Fe(III)-phosphate formed in Mg electrolyte suitable lower estimates for the respective $(\text{Ca}/\text{Fe})_{1.5}$ and $(\text{P}/\text{Fe})_{1.5}$ in the non-mitridatite Fe-phosphate fraction of Ca-Fe(III)-phosphate formed in the Ca and Ca+Si electrolytes. Noting that Ca in the low Ca electrolyte already detectably affected local Fe coordination (Fig. 6), the respective $(\text{Ca}/\text{Fe})_{1.5}$ and $(\text{P}/\text{Fe})_{1.5}$ ratios were taken as upper estimates for Ca and phosphate associated with non-mitridatite Fe. Combining these lower and upper estimates with non-mitridatite Ca-Fe(III)-phosphate fractions of 85-70% estimated from the LCF results, between 60-53% of the total phosphate in Ca-Fe(III)-phosphate formed at $(\text{P}/\text{Fe})_{\text{init}}$ of 1.5 in the Ca and Ca+Si electrolytes was estimated to be bound to non-mitridatite Fe(III)-phosphate polymers and 30-37% of the total Ca was estimated to be associated with this fraction via electrostatic interactions or more covalent bonding to Fe(III)-coordinated phosphate groups (Table EA7).

4.1.2.3 Ca-phosphate polymers

Only 45-64% of the total Ca and 75-82% of the total phosphate in Ca-Fe(III)-phosphate formed at $(\text{P}/\text{Fe})_{\text{init}}$ of 1.5 in the Ca and Ca+Si electrolytes can be attributed to mitridatite-like (14-29% and 15-30%) and Fe(III)-phosphate-like Fe (30-37% and 60-53%) (Table EA7). The remaining unaccounted Ca and phosphate fractions correspond to a Ca/P ratio of 1.51-1.35, which falls into the range of Ca/P ratios of common Ca-phosphates (HAP 1.67, β -TCP 1.5, octacalciumphosphate (OCP) 1.33, brushite 1). These calculations, although based on numerous assumptions, thus point to the formation of Fe-free Ca-phosphate polymers in the Ca and Ca+Si electrolytes at $(\text{P}/\text{Fe})_{\text{init}}$ of ~ 1.5 . Formation of Ca-phosphate polymers in the Ca and Ca+Si electrolytes was also indicated by the strong increase of $(\text{Ca}/\text{Fe})_{\text{ppt}}$ and $(\text{P}/\text{Fe})_{\text{ppt}}$ in the Ca and Ca+Si electrolytes from $(\text{P}/\text{Fe})_{\text{init}}$ of ~ 0.75 to ~ 2 (Fig. 3b) without concomitant changes in local Fe coordination at $(\text{P}/\text{Fe})_{\text{init}} \geq 1$ (identical Fe K-edge EXAFS spectra). From the linear regression of the $(\text{Ca}/\text{Fe})_{\text{ppt}}$ over $(\text{P}/\text{Fe})_{\text{ppt}}$ ratios of precipitates formed at $(\text{P}/\text{Fe})_{\text{init}} \geq 0.75$ in the Ca and Ca+Si electrolytes, a $(\text{Ca}/\text{P})_{\text{ppt}}$ of 1.22 (± 0.17) was derived for Ca-phosphate polymers

(Fig. 3b), in reasonable agreement with a Ca/P ratio of 1.51-1.35 of the Ca and phosphate fractions that were not associated with Fe (Table EA7). Spectroscopically, the formation of amorphous Ca-phosphate polymers at high phosphate and Ca concentrations was in line with FTIR data indicating that Ca induced a shift in phosphate bands consistent with contributions from amorphous Ca-phosphate (Fig. 11), and with the Ca K-edge XAS spectrum of the sample Ca 1.45, which exhibited a first-shell Ca-O peak amplitude similar to brushite or a ~2:1 mixture of HAP and aqueous Ca^{2+} (Fig. 10).

The Ca and Ca+Si starting solutions with 4 mM Ca (at pH 7.0) reached saturation with respect to β -TCP, OCP and brushite at a $(\text{P/Fe})_{\text{init}}$ of about 0.08, 0.3 and 1.0 (0.04, 0.15 and 0.5 mM phosphate), respectively. The low Ca starting solution with 0.5 mM Ca, on the other hand, reached saturation with respect to β -TCP at $(\text{P/Fe})_{\text{init}} \sim 1$, but remained undersaturated with respect to brushite and OCP even at $(\text{P/Fe})_{\text{init}}$ of 2. Considering that the trends in $(\text{Ca/Fe})_{\text{ppt}}$ as a function of $(\text{P/Fe})_{\text{ppt}}$ (Fig. 3b) pointed to Ca-phosphate precipitation at high $(\text{P/Fe})_{\text{init}}$ in the Ca and Ca+Si electrolytes but not in the low Ca electrolyte, these thermodynamic calculations suggest that oversaturation with respect to brushite or OCP is required for Ca-phosphate polymer formation under our experimental conditions over 4 h reaction time. Indeed, experiments in Ca electrolyte with up to 1 mM phosphate and without Fe(II) addition did not reveal any Ca-phosphate precipitation. Thus, even at the highest $(\text{P/Fe})_{\text{init}}$ of 2, Ca-phosphate polymer formation over the 4 h reaction time was dominantly due to co-precipitation with Fe, in line with the relatively slow kinetics of Ca-phosphate precipitation under comparable conditions (Wright et al., 2011). Noting that the formation of amorphous Ca-phosphate may proceed via the aggregation of pre-nucleation clusters (Posner and Betts, 1975; Dey et al., 2010) of <1 nm size (Fig. 14m), we hypothesize that relatively fast oxidation and precipitation of Fe in solutions that are oversaturated with respect to brushite or OCP triggers the co-

precipitation of Ca-phosphate polymers into amorphous Ca-Fe(III)-phosphate under conditions where Ca-phosphate precipitation in the absence of Fe is still slow.

4.2. Sequential precipitate formation at $(P/Fe)_{init} < (P/Fe)_{crit}$

At initial dissolved P/Fe ratios $< (P/Fe)_{crit}$, the changes in suspension color over the course of Fe oxidation (Fig. 1) in combination with the Fe K-edge XAS results (Fig. 5) showed that the initial precipitation of (Ca-)Fe(III)-phosphate was followed by the formation of other types of precipitates, mainly lepidocrocite in the absence of silicate and a ferrihydrite-like precipitate in the presence of silicate (Fig. 15). In the following subsections, we will first discuss the initial formation of (Ca-)Fe(III)-phosphate at $(P/Fe)_{init} < (P/Fe)_{crit}$, followed by three subsections addressing subsequent precipitate formation in the absence and presence of silicate and incipient precipitate aging over the 4 h reaction period.

4.2.1. Initial formation of amorphous (Ca)-Fe(III)-phosphate

Amorphous (Ca-)Fe(III)-phosphates did not only form at $(P/Fe)_{init} > (P/Fe)_{crit}$ but were also the first phase precipitating at lower $(P/Fe)_{init}$ ratios (except the phosphate-free treatment). In previous studies, the initial precipitation of (Ca-)Fe(III)-phosphate during Fe(II) oxidation was inferred from changes in dissolved Fe(II) and phosphate concentrations (Einsele, 1938; Tessenow, 1974; Deng, 1997; Gunnars et al., 2002; Voegelin et al., 2013; van Genuchten et al., 2014a). In this study, we did not monitor the changes in solution and precipitate composition or in precipitate structure over time, but the changes in suspension color (Fig. 1) confirmed the initial formation of (Ca-)Fe(III)-phosphate precipitates. The P/Fe ratios of the amorphous (Ca-)Fe(III)-phosphate formed at intermediate $(P/Fe)_{init}$ from 0.2 to 0.75 were estimated by multiple linear regressions of $(P/Fe)_{ppt}$ over the LCF-derived fractions of FeP*, CaFeP* or lowCaFeP* and HFO or Fh-Si* (see section 3.2.3 and Fig. EA11). The resulting $(P/Fe)_{((low)Ca)FeP^*}$ ratios closely matched the $(P/Fe)_{crit}$ of the respective electrolytes (Table 2;

Fig. EA11b), indicating that amorphous (Ca-)Fe(III)-phosphate formed at $(P/Fe)_{\text{init}} \leq (P/Fe)_{\text{crit}}$ exhibited a $(P/Fe)_{\text{ppt}}$ ratio similar to $(P/Fe)_{\text{crit}}$.

4.2.2. Transformation of initial (Ca)-Fe(III)-phosphate and formation of lepidocrocite in the absence of silicate

In a recent study on the dynamics of Fe precipitate formation during Fe(II) oxidation in the presence of phosphate in Na background electrolyte (Voegelin et al., 2013), we concluded that initial Fe(III)-phosphate formation was followed by its (partial to complete) transformation into a phosphate-rich ferrihydrite-type precipitate with P/Fe of 0.25 during continuing Fe(II) oxidation and concomitant lepidocrocite precipitation. One manifestation of the transformation of initially formed Fe(III)-phosphate was that the final Fe(III)-phosphate fraction derived from Fe K-edge XAS results was smaller than estimated based on the assumption that the initially formed Fe(III)-phosphate does not transform during continuing Fe oxidation and precipitation (Voegelin et al., 2013). In the present study, the same trend was observed when comparing the EXAFS-derived Fe(III)-phosphate fraction of precipitates formed in Na electrolyte with fractions estimated by assuming the formation of non-transforming Fe(III)-phosphate (Fig. 8). A similar extent of Fe(III)-phosphate transformation was observed for the Mg electrolyte. The LCF-derived Ca-Fe(III)-phosphate fractions in the Ca electrolyte on the other hand were slightly closer to the estimated fractions. This may suggest that the structural incorporation of Ca into Ca-Fe(III)-phosphate with a higher degree of Fe(III) polymerization reduces the susceptibility of the precipitate to undergo further polymerization and transformation.

Irrespective of the extent to which the initially formed (Ca-)Fe(III)-phosphate was transformed during ongoing Fe(II) oxidation, the $(P/Fe)_{\text{HFO}}$ of the ferrihydrite-type transformation products in the Na, Mg, Ca and low Ca electrolytes derived from linear regressions ranged between 0.21 ± 0.06 and 0.30 ± 0.05 (Table 2), in good agreement with a phosphate sorption capacity of ~ 0.25 P/Fe reported for ferrihydrite-type precipitates (Lijklema,

1 1980; Gerke, 1993; Voegelin et al., 2013). Because nearly all phosphate was initially taken up
2 by the (Ca-)Fe(III)-phosphate precipitate, the phosphate-saturated ferrihydrite-type precipitate
3 must have formed by (partial) transformation of (Ca-)Fe(III)-phosphate. Most probably, the
4 transformation of (Ca-)Fe(III)-phosphate into phosphate-saturated ferrihydrite-type precipitate
5 thus proceeded by Fe(II) oxidation on the (Ca-)Fe(III)-phosphate-/ferrihydrite particles,
6 resulting in a gradual decrease of the average $(P/Fe)_{ppt}$ ratio and concomitant increase of the
7 average degree of Fe(III) polymerization.

8 The Fe K-edge EXAFS (Fig. 5), XRD (Fig. 9) and STEM (Fig. 12) results also
9 confirmed the parallel formation of poorly-crystalline lepidocrocite that accumulated on the
10 surface of the (transformed) Fe(III)-phosphate/ferrihydrite particles (Fig. 15a). The multiple
11 linear regressions of the $(P/Fe)_{ppt}$ against $pcLp^*$, HFO and FeP^* , $CaFeP^*$ or $lowCaFeP^*$
12 returned $(P/Fe)_{pcLp^*}$ of 0. This indicates that phosphate was effectively retained within the
13 Fe(III)-phosphate/ferrihydrite particles and is qualitatively in line with TEM-EDX data
14 indicating that the P/Fe ratio of poorly-crystalline lepidocrocite formed around transformed
15 Fe(III)-phosphate is low (Voegelin et al., 2013).

16 4.2.3. Transformation of initial (Ca)-Fe(III)-phosphate and formation of ferrihydrite-like 17 precipitate in the presence of silicate

18 In the silicate-containing electrolytes Na+Si and Ca+Si, the evolution of precipitate color
19 (Fig. 1) and Fe K-edge XAS results (Fig. 5) indicated that a ferrihydrite-type precipitate
20 formed after initial (Ca-)Fe(III)-phosphate formation, in line with the known effect of silicate
21 on the structure of Fe(III)-precipitates formed by Fe(II) oxidation in phosphate-free solutions
22 (Schwertmann and Thalmann, 1976; Voegelin et al., 2010).

23 In both silicate-containing electrolytes, the LCF-derived (Ca-)Fe(III)-phosphate fractions
24 in the final precipitate closely followed the estimates calculated on the assumption of a non-
25 transforming (Ca-)Fe(III)-phosphate precipitate (Fig. 8). Silicate thus effectively inhibited the

transformation of the initially formed (Ca-)Fe(III)-phosphate and thereby the resolubilization of phosphate, even in the absence the Ca (Fig. 2ae). The $(P/Fe)_{Fh-Si^*}$ ratios obtained from linear regressions of $(P/Fe)_{ppt}$ ratios against $Fh-Si^*$ and FeP^* or $CaFeP^*$ fractions of precipitates formed at $(P/Fe)_{init}$ of $\sim 0.2-0.75$ (Table 2) indicated that hardly any phosphate was taken up by the $Fh-Si^*$ precipitate fraction, which instead was stabilized by the uptake of ~ 0.1 Si/Fe according to digestion results (Table 3). Considering that dissolved phosphate exhibits a much higher sorption affinity for Fe(III)-precipitates than dissolved silicate (Roberts et al., 2004), these observations suggest that the uptake of silicate by the $Fh-Si^*$ precipitate was enabled by the effective retention of phosphate within the initially formed (Ca-)Fe(III)-phosphate. The uptake of ~ 0.1 Si/Fe by the $Fh-Si^*$ in turn seemed to reduce its effectiveness as a sink for phosphate that could drive the transformation of initially formed Fe(III)-phosphate (McLaughlin and Syers, 1978).

Considering this sequence of events, the resulting precipitate was expected to consist of cores of Ca-Fe(III)-phosphate surrounded by silicate-containing ferrihydrite. Independent and direct evidence for the formation of such structured precipitate particles that reflect their formation history was obtained by STEM-EDX analysis of a precipitate formed at $(P/Fe)_{init}$ 0.19 in the Ca+Si electrolyte (Fig. 13). These results also highlight that the analysis of such Fe(III)-precipitates using bulk spectroscopic techniques is prone to incorrect structural interpretations if their complex structure and the presence of multiple amorphous to poorly crystalline phases is not explicitly taken into account (Fig. 15b).

4.2.4. *Phosphate resolubilization due to incipient precipitate aging*

In the silicate-free electrolytes, the fraction of residual dissolved phosphate increased for decreasing $(P/Fe)_{init}$ from $(P/Fe)_{crit}$ to 0.05 (Fig. 2). This trend was attributed to incipient precipitate aging. In a time-resolved experiment in Na electrolyte at $(P/Fe)_{init}$ of ~ 0.3 , we previously observed that dissolved phosphate started to increase as soon as Fe(II) oxidation

1 was nearly complete (after about 2 h), i.e., as soon as no further Fe(III) was added to the solid
2 that could scavenge phosphate released from the slowly transforming Fe(III)-phosphate
3 (Voegelin et al., 2013). This increase reflected that precipitate formation immediately
4 transitioned into precipitate aging and associated phosphate release, as previously observed for
5 amorphous Fe(III)-precipitate formed in the presence of phosphate and arsenate (Hsu, 1982;
6 Fuller et al., 1993; Mayer and Jarrell, 2000). The release of a larger fraction of total phosphate
7 at lower $(P/Fe)_{init}$ may reflect that phosphate at lower $(P/Fe)_{init}$ less effectively inhibits the
8 continuing polymerization and crystallization of Fe(III) (Galvez et al., 1999). In the Ca
9 electrolyte, phosphate resolubilization appeared slightly less pronounced than in the Na
10 electrolyte (Fig. 2a). This may be due to a stabilization of the initially formed Ca-Fe(III)-
11 phosphate by structurally incorporated Ca or due to incipient slow formation of a Ca-phosphate
12 precipitate (Wright et al., 2011).

13 In the silicate containing electrolytes, no analogous increase in dissolved phosphate
14 fractions was observed (Fig. 2e), in line with an earlier study on the effect of silicate on
15 phosphate uptake and retention by Fe oxidation products (Mayer and Jarrell, 2000). This can
16 be attributed to the formation of a ferrihydrite precipitate around the initially formed (Ca-
17)Fe(III)-phosphate (Fig. 13), which acts as a much more effective containment for phosphate
18 released from aging (Ca-)Fe(III)-phosphate than surrounding lepidocrocite formed in the
19 absence of silicate.

20 **4.3. Environmental implications**

21 The formation of Ca- and P-rich Fe(III)-precipitates critically affects phosphate dynamics
22 in aquatic systems, for example at the oxic-anoxic boundary in the water column or the
23 sediments of lakes (Leppard et al., 1988; Buffle et al., 1989; Deike et al., 1997; Lienemann et
24 al., 1999; Och et al., 2012; Cosmidis et al., 2014) or in oxygenated groundwater (Wolthoorn et
25 al., 2004; Griffioen, 2006; Voegelin et al., 2010; van Genuchten et al., 2014a). Based on field

1 and laboratory observations, the uptake of phosphate and Ca by such precipitates has been
2 attributed to adsorption processes or to formation of Ca-, Fe- or mixed Ca-Fe-phosphate
3 precipitates (Tipping et al., 1989; Deike et al., 1997; Matthiesen et al., 2001; Gunnars et al.,
4 2002; Griffioen, 2006; Voegelin et al., 2010; van Genuchten et al., 2014a). With respect to the
5 interpretation of data on the composition and structure of Ca- and phosphate-rich Fe(III)-
6 precipitates, our results point out that is essential to consider whether the respective
7 precipitates formed under conditions leading to exclusive amorphous (Ca-)Fe(III)-phosphate
8 precipitation ($(P/Fe)_{init} > (P/Fe)_{crit}$) or under conditions leading to the sequential formation of
9 (Ca-)Fe(III)-phosphate followed by other Fe(III)-precipitates (Fig. 15). Our results further
10 show that amorphous basic (Ca-)Fe(III)-phosphates formed by Fe(II) oxidation in near-neutral
11 water can be described as mixtures of different polymeric units, namely Fe(III)-phosphate
12 polymers with sorbed Ca, mitridatite-like Ca-Fe(III)-phosphate polymers with structural Ca,
13 and Ca-phosphate polymers (Fig. 14), whose fractions vary with solution chemistry. This
14 polymer mixing concept allows to rationalize the findings of Griffioen (2006) that the extent of
15 phosphate removal during oxygenation of phosphate-rich anoxic groundwater did not
16 correlated with $(P/Fe)_{init}$ alone, but that also the saturation index of hydroxyapatite had to be
17 included in a descriptive linear regression model. The presented polymer mixing model has
18 been derived from experiments performed at pH 7.0, but may also prove useful to assess
19 aspects such as the effect of solution pH on the structure and composition of amorphous basic
20 (Ca-)Fe(III)-phosphate or the mode of trace element uptake.

21 Mitridatite has been stated to be “quite stable and possible one of the most important
22 ferric phosphates formed under rather neutral conditions and ambient temperatures” (Moore
23 and Araki, 1977). In lacustrine deposits, mitridatite formation has been attributed to the
24 transformation of vivianite formed in anoxic sediment by reaction with Ca-rich water into
25 anapaite (Ca-Fe(II)-phosphate) followed by Fe(II) oxidation under oxic conditions (Stamatakis

1 and Koukoulas, 2001). The observation of mitridatite-like polymers in freshly precipitated
2 amorphous Ca-Fe(III)-phosphate suggests that the basic structural unit of mitridatite can also
3 directly form during Fe(II) oxidation in near-neutral Ca- and phosphate-containing solutions. If
4 and under which conditions and over which timescales mitridatite-like polymers may transform
5 into crystalline mitridatite is currently not known.

6 In the context of water treatment and nutrient and contaminant dynamics in
7 environmental systems, the uptake of arsenic, phosphate, and other ions by Fe oxidation
8 products is commonly modelled as an adsorption process on a single "hydrous ferric oxide
9 phase" (Wilkie and Hering, 1996; Meng et al., 2002; Roberts et al., 2004; Li et al., 2012; Mao
10 et al., 2012). Such models allow to quantify ion uptake by fresh Fe(III)-precipitates under
11 specific chemical conditions, but do not account for the structural complexity of Fe oxidation
12 products. To study and quantify aspects such as the impact of Ca on precipitate structure and
13 ion uptake, selective ion uptake by individual precipitate types, or differences in the colloidal
14 and chemical stability of individual precipitate types and their impact on co-transformed
15 elements, Fe oxidation products formed in near-neutral water should be described as mixtures
16 of three types of Fe(III)-precipitates whose fractions depend on formation conditions and
17 whose individual physicochemical properties need to be taken into account: (i) Amorphous
18 basic (Ca-)Fe(III)-phosphate consisting of variable proportions of different polymeric units
19 (Fig. 14), (ii) Ferrihydrite-type precipitates with properties similar to well-studied synthetic
20 two-line ferrihydrite (Dzombak and Morel, 1990; Jambor and Dutrizac, 1998) and (iii) poorly-
21 crystalline lepidocrocite (and goethite) with much lower ion sorption capacity than ferrihydrite.

22 For precipitates formed over the course of complete Fe(II) oxidation in near-neutral
23 water at initial dissolved phosphate/Fe(II) ratios below $(P/Fe)_{crit}$, this study reveals how the
24 sequential formation of different precipitate types and precipitate transformation affect the
25 spatial arrangement of the different precipitate types within individual precipitate particles

(Fig. 15). These findings apply to precipitates formed during complete Fe(II) oxidation in mixed suspensions, for example aerated groundwater or Fe(II)-spiked water in a tank or exfiltrating groundwater in a stream. In other situations, however, Fe(II) oxidation and sequential precipitate formation may also lead to the spatially separated formation of different precipitate types, for example in water flowing through porous media with concomitant precipitate attachment (e.g., in aquifers or sand filters) or along opposing diffusion gradients of Fe(II) and O₂ (e.g., at the redoxcline in lake water columns). Different precipitate types may also result from continuous Fe(II) input and Fe(III)-precipitate removal in aerated mixed batch reactors (e.g., in wastewater treatment plants using Fe(II) as coagulant). In any case, in addition to the formation of different precipitate types, their spatial arrangement within individual precipitate particles (Fig. 15) or their formation along spatial gradients needs to be taken into account when addressing the effect of dissolved Fe oxidation and precipitate formation on the cycling of major and trace elements in aquatic systems.

5. ACKNOWLEDGEMENTS

Irene Brunner, Thomas Rüttimann and Numa Pfenninger (Eawag, Switzerland) are acknowledged for assistance with laboratory experiments and analyses. The Angströmquelle Karlsruhe (ANKA, Karlsruhe, Germany) and the Swiss Norwegian Beamline (SNBL, ESRF, Grenoble, France) are acknowledged for providing synchrotron XAS beamtime. We thank Herman Emerich and Wouter van Beek (SNBL, ESRF) for their help during XAS data acquisition. The Electron Microscopy Centre of the ETH Zurich (EMEZ) is acknowledged for access to electron microscopes. Three anonymous reviewers and the associate editor are acknowledged for their detailed and constructive comments which helped to improve the quality of the manuscript. This project was financially supported by the Swiss National Science Foundation under contracts No. 200021-132123 and 200020-152993.

6. REFERENCES

- Raiswell and Canfield, 2012Bonneville, S., Van Cappellen, P., Behrends, T. (2004). Microbial reduction of iron(III) oxyhydroxides: effects of mineral solubility and availability. *Chem. Geol.* **212**, 255-268.
- Buffle, J., De Vitre, R.R., Perret, D., Leppard, G.G. (1989). Physico-chemical characteristics of a colloidal iron phosphate species formed at the oxic-anoxic interface of a eutrophic lake. *Geochim. Cosmochim. Acta* **53**, 399-408.
- Châtellier, X., Grybos, M., Abdelmoula, M., Kemner, K.M., Leppard, G.G., Mustin, C., West, M.M., Paktunc, D. (2013). Immobilization of P by oxidation of Fe(II) ions leading to nanoparticle formation and aggregation. *Appl. Geochem.* **35**, 325-339.
- Cornell, R.M., Schwertmann, U. (2003) *The Iron Oxides: Structure, Properties, Reactions, Occurrences and Uses*. Wiley-VCH, Weinheim.
- Cosmidis, J., Benzerara, K., Morin, G., Busigny, V., Lebeau, O., Jézéquel, D., Noël, V., Dublet, G., Othmane, G. (2014). Biomineralization of iron-phosphates in the water column of Lake Pavin (Massif Central, France). *Geochim. Cosmochim. Acta* **126**, 78-96.
- Cumplido, J., Barrón, V., Torrent, J. (2000). Effect of phosphate on the formation of nanophase lepidocrocite from Fe(II) sulfate. *Clays Clay Min.* **48**, 503-510.
- Deike, R.G., Granina, L., Callender, E., McGee, J.J. (1997). Formation of ferric iron crusts in Quaternary sediments of Lake Baikal, Russia, and implications for paleoclimate. *Mar. Geol.* **139**, 21-46.
- Deng, Y. (1997). Formation of iron(III) hydroxides from homogeneous solutions. *Water Research* **31**, 1347-1354.
- Dey, A., Bomans, P.H.H., Müller, F.A., Will, J., Frederik, P.M., de With, G., Sommerdijk, N.A.J.M. (2010). The role of prenucleation clusters in surface-induced calcium phosphate crystallization. *Nat Mater* **9**, 1010-1014.
- Doelsch, E., Rose, J., Masion, A., Bottero, J.Y., Nahon, D., Bertsch, P.M. (2000). Speciation and crystal chemistry of iron(III) chloride hydrolyzed in the presence of SiO₄ ligands. 1. An Fe K-edge EXAFS study. *Langmuir* **16**, 4726-4731.
- Dormann, J., Gasperin, M., Poullen, J.F. (1982). Etude structurale de la sequence d'oxydation de la vivianite Fe₃(PO₄)₂*8H₂O. *Bulletin de Minéralogie* **105**, 147-116.
- Dzombak, D.A., Morel, F.M.M. (1990) *Surface Complexation Modeling, Hydrous Ferric Oxide*. John Wiley and Sons, New York.
- Einsele, W. (1938). Über chemische und kolloidchemische Vorgänge in Eisen-Phosphat-Systemen unter limnochemischen und limnogeologischen Gesichtspunkten. *Arch. Hydrobiol.* **33**, 361-387.
- Fuller, C.C., Davis, J.A., Waychunas, G.A. (1993). Surface chemistry of ferrihydrite: Part 2. Kinetics of arsenate adsorption and coprecipitation. *Geochim. Cosmochim. Acta* **57**, 2271-2282.
- Galvez, N., Barron, V., Torrent, J. (1999). Effect of phosphate on the crystallization of hematite, goethite, and lepidocrocite from ferrihydrite. *Clays Clay Min.* **47**, 304-311.
- Gerke, J. (1993). Phosphate adsorption by humic/Fe-oxide mixtures aged at pH 4 and 7 and by poorly ordered Fe-oxide. *Geoderma* **59**, 279-288.
- Griffioen, J. (2006). Extent of immobilisation of phosphate during aeration of nutrient-rich, anoxic groundwater. *Journal of Hydrology* **320**, 359-369.
- Gunnars, A., Blomqvist, S., Johansson, P., Andersson, C. (2002). Formation of Fe(III) oxyhydroxide colloids in freshwater and brackish seawater, with incorporation of phosphate and calcium. *Geochim. Cosmochim. Acta* **66**, 745-758.
- Hassellöv, M., von der Kammer, F. (2008). Iron oxides as geochemical nanovectors for metal transport in soil-river systems. *Elements* **4**, 401-406.
- Hsu, P.H. (1973). Complementary role of iron(III), sulfate and calcium in precipitation of phosphate from solution. *Environmental Letters* **5**, 115-136.
- Hsu, P.H. (1982). Crystallization of iron(III) phosphate at room temperature. *Soil Sci. Soc. Am. J.* **46**, 928-932.

- 1 Inskeep, W.P., Macur, R.E., Harrison, G., Bostick, B.C., Fendorf, S. (2004). Biomineralization of
2 As(V)-hydrous ferric oxyhydroxide in microbial mats of an acid-sulfate-chloride geothermal
3 spring, Yellowstone National Park. *Geochim. Cosmochim. Acta* **68**, 3141-3155.
- 4 Jambor, J.L., Dutrizac, J. (1998). Occurrence and constitution of natural and synthetic ferrihydrite, a
5 widespread iron oxyhydroxide. *Chemical Reviews* **98**, 2549-2585.
- 6 Kaegi, R., Voegelin, A., Folini, D., Hug, S.J. (2010). Effect of phosphate, silicate, and Ca on the
7 morphology, structure and elemental composition of Fe(III)-precipitates formed in aerated Fe(II)
8 and As(III) containing water. *Geochim. Cosmochim. Acta* **74**, 5798-5816.
- 9 King, D.W. (1998). Role of carbonate speciation on the oxidation rate of Fe(II) in aquatic systems.
10 *Environmental Science & Technology* **32**, 2997-3003.
- 11 Leppard, G.G., Buffle, J., de Vitre, R., Perret, D. (1988). The ultrastructure and physical characteristics
12 of a distinctive colloidal iron particulate isolated from a small eutrophic lake. *Arch. Hydrobiol.*
13 **113**, 405-424.
- 14 Li, L., van Genuchten, C.M., Addy, S.E.A., Yao, J., Gao, N., Gadgil, A.J. (2012). Modeling As(III)
15 oxidation and removal with iron electrocoagulation in groundwater. *Environmental Science &*
16 *Technology* **46**, 12038-12045.
- 17 Lienemann, C.-P., Monnerat, M., Dominik, J., Perret, D. (1999). Identification of stoichiometric iron-
18 phosphorus colloids produced in a eutrophic lake. *Aquat. Sci.* **61**, 133-149.
- 19 Lijklema, L. (1980). Interaction of orthophosphate with iron(III) and aluminum hydroxides.
20 *Environmental Science & Technology* **14**, 537-541.
- 21 Mao, Y., Ninh Pham, A., Xin, Y., David Waite, T. (2012). Effects of pH, floc age and organic
22 compounds on the removal of phosphate by pre-polymerized hydrous ferric oxides. *Separation and*
23 *Purification Technology* **91**, 38-45.
- 24 Marcus, M.A., Macdowell, A.A., Celestre, R.S., Manceau, A., Miller, T., Padmore, H.A., Sublett, R.E.
25 (2004). Beamline 10.3.2 at ALS: a hard X-ray microprobe for environmental and materials
26 sciences. *J. Synchrotron Rad.* **11**, 239-247.
- 27 Matthiesen, H., Leipe, T., Laima, M.J.C. (2001). A new experimental setup for studying the formation
28 of phosphate binding iron oxides in marine sediments. Preliminary results. *Biogeochemistry* **52**,
29 79-92.
- 30 Mayer, D.T., Jarrell, W.M. (1996). Formation and stability of iron(II) oxidation products under natural
31 concentrations of dissolved silica. *Water Research* **30**, 1208-1214.
- 32 Mayer, D.T., Jarrell, W.M. (2000). Phosphorus sorption during iron(II) oxidation in the presence of
33 dissolved silica. *Water Research* **34**, 3949-3956.
- 34 McLaughlin, J.R., Syers, J.K. (1978). Stability of ferric phosphates. *Journal of Soil Science* **29**, 499-
35 504.
- 36 Meng, X.G., Korfiatis, G.P., Bang, S.B., Bang, K.W. (2002). Combined effects of anions on arsenic
37 removal by iron hydroxides. *Toxicol. Lett.* **133**, 103-111.
- 38 Mikutta, C., Schröder, C., Marc Michel, F. (2014). Total X-ray scattering, EXAFS, and Mössbauer
39 spectroscopy analyses of amorphous ferric arsenate and amorphous ferric phosphate. *Geochim.*
40 *Cosmochim. Acta* **140**, 708-719.
- 41 Millero, F.J., Sotolongo, S., Izaguirre, M. (1987). The oxidation kinetics of Fe(II) in seawater.
42 *Geochim. Cosmochim. Acta* **51**, 793-801.
- 43 Momma, K., Izumi, F. (2011). VESTA 3 for three-dimensional visualization of crystal, volumetric and
44 morphology data. *Journal of Applied Crystallography* **44**, 1272-1276.
- 45 Moore, P.B., Araki, T. (1977). Mitridatite, $\text{Ca}_6(\text{H}_2\text{O})_6[\text{FeIII}_9\text{O}_6(\text{PO}_4)_9] \cdot 3\text{H}_2\text{O}$. A noteworthy
46 octahedral sheet structure. *Am. Min.* **16**, 1096-1106.
- 47 Niu, J., Ma, J., Zhao, J., Ma, P., Wang, J. (2011). A new 2D network polyoxometalate constructed from
48 Strandberg-type phosphomolybdates linked through binuclear Ca(II) clusters. *Inorganic Chemistry*
49 *Communications* **14**, 474-477.
- 50 Och, L.M., Müller, B., Voegelin, A., Ulrich, A., Göttlicher, J., Steiniger, R., Mangold, S., Vologina,
51 E.G., Sturm, M. (2012). New insights into the formation and burial of Fe/Mn accumulations in
52 Lake Baikal sediments. *Chem. Geol.* **330-331**, 244-259.

- 1 Paktunc, D., Dutrizac, J., Gertsman, V. (2008). Synthesis and phase transformations involving
2 scorodite, ferric arsenate and arsenical ferrihydrite: Implications for arsenic mobility. *Geochim.*
3 *Cosmochim. Acta* **72**, 2649-2672.
- 4 Parkhurst, D.L., Appelo, C.A.J. (1999) *User's guide to PHREEQC (Version 2) - a computer program*
5 *for speciation, batch-reaction, one-dimensional transport, and inverse geochemical calculations.*
6 U.S. Geological Survey, Denver, CO.
- 7 Peacor, D.R., Dunn, P.J., Simmons, W.B., Ramik, R.A. (1987). Ferristrunzite, a new member of the
8 strunzite group, from Blaton, Belgium. *Neues Jahrbuch für Mineralogie - Monatshefte*, 433-440.
- 9 Posner, A.S., Betts, F. (1975). Synthetic amorphous calcium phosphate and its relation to bone mineral
10 structure. *Accounts of Chemical Research* **8**, 273-281.
- 11 Pratesi, G., Cipriani, C., Giuli, G., Birch, W.D. (2003). Santabarbaraite: a new amorphous phosphate
12 mineral. *European Journal of Mineralogy* **15**, 185-192.
- 13 Raiswell, R., Canfield, D.E. (2012). The iron biogeochemical cycle past and present. *Geochemical*
14 *Perspectives* **1**, 1-2.
- 15 Raiswell, R., Vu, H.P., Brinza, L., Benning, L.G. (2010). The determination of labile Fe in ferrihydrite
16 by ascorbic acid extraction: Methodology, dissolution kinetics and loss of solubility with age and
17 de-watering. *Chem. Geol.* **278**, 70-79.
- 18 Ravel, B., Newville, M. (2005). ATHENA, ARTEMIS, HEPHAESTUS: data analysis for X-ray
19 absorption spectroscopy using IFEFFIT. *J. Synchrotron Rad.* **12**, 537-541.
- 20 Rietra, R.P.J.J., Hiemstra, T., Van Riemsdijk, W.H. (2001). Interaction between calcium and phosphate
21 adsorption on goethite. *Environ. Sci. Technol.* **35**, 3369-3374.
- 22 Ritchie, C., Li, F., Pradeep, C.P., Long, D.-L., Xu, L., Cronin, L. (2009). A functional hybrid
23 polyoxometalate framework based on a 'trilacunary' heteropolyanion
24 $[(P_4W_6O_{34})_2Co_2Na_2(H_2O)_2]^{18-}$. *Dalton Transactions*, 6483-6486.
- 25 Roberts, L.C., Hug, S.J., Ruettimann, T., Billah, M.M., Khan, A.W., Rahman, M.T. (2004). Arsenic
26 removal with iron(II) and iron(III) in waters with high silicate and phosphate concentrations.
27 *Environ. Sci. Technol.* **38**, 307-315.
- 28 Rose, J., Flank, A.-M., Masion, A., Bottero, J.Y., Emerich, P. (1997). Nucleation and growth
29 mechanisms of Fe oxyhydroxide in the presence of PO_4 ions. 2. P K-edge EXAFS study. *Langmuir*
30 **13**, 1827-1834.
- 31 Rose, J., Manceau, A., Bottero, J.Y., Masion, A., Garcia, F. (1996). Nucleation and growth mechanisms
32 of Fe oxyhydroxide in the presence of PO_4 ions. 1. Fe K-edge EXAFS study. *Langmuir* **12**, 6701-
33 6707.
- 34 Sahai, N., Lee, Y.J., Xu, H., Ciardelli, M., Gaillard, J.-F. (2007). Role of Fe(II) and phosphate in
35 arsenic uptake by coprecipitation. *Geochim. Cosmochim. Acta* **71**, 3193-3210.
- 36 Schofield, P.F., Knight, K.S., Houwen, J.A.M.v.d., Valsami-Jones, E. (2004). The role of hydrogen
37 bonding in the thermal expansion and dehydration of brushite, di-calcium phosphate dihydrate.
38 *Physics and Chemistry of Minerals* **31**, 606-624.
- 39 Schwertmann, U., Carlson, L., Fechter, H. (1984). Iron oxide formation in artificial ground waters.
40 *Schweizerische Zeitschrift für Hydrologie* **46**, 185-191.
- 41 Schwertmann, U., Taylor, R.M. (1979). Natural and synthetic poorly crystallized lepidocrocite. *Clay*
42 *Minerals* **14**, 285-293.
- 43 Schwertmann, U., Thalmann, H. (1976). The influence of $[Fe(II)]$, $[Si]$, and pH on the formation of
44 lepidocrocite and ferrihydrite during oxidation of aqueous $FeCl_2$ solutions. *Clay Minerals* **11**, 189-
45 200.
- 46 Stamatakis, M.G., Koukoulas, N.K. (2001). The occurrence of phosphate minerals in lacustrine clayey
47 diatomite deposits, Thessaly, Central Greece. *Sedimentary Geology* **139**, 33-47.
- 48 Stumm, W., Lee, G.F. (1961). Oxygenation of Ferrous Iron. *Industrial & Engineering Chemistry* **53**,
49 143-146.
- 50 Stumm, W., Sulzberger, B. (1992). The cycling of iron in natural environments: Considerations based
51 on laboratory studies of heterogeneous redox processes. *Geochim. Cosmochim. Acta* **56**, 3233-
52 3257.
- 53 Tamura, H., Goto, K., Nagayama, M. (1976). The effect of ferric hydroxide on the oxygenation of
54 ferrous ions in neutral solutions. *Corrosion Science* **16**, 197-207.

- 1 Taylor, K.G., Konhauser, K.O. (2011). Iron in Earth surface systems: A major player in chemical and
2 biological processes. *Elements Magazine* **7**, 83-88.
- 3 Tessenow, U. (1974). Lösungs-, Diffusions- und Sorptionsprozesse in der Oberschicht von
4 Seesedimenten. IV. Reaktionsmechanismen und Gleichgewichte im System Eisen-Mangan-
5 Phosphat im Hinblick auf die Vivianitakkumulation im Ursee. *Arch. Hydrobiol. Suppl.* **47**, 1-79.
- 6 Thibault, P.-J., Rancourt, D.G., Evans, R.J., Dutrizac, J. (2009). Mineralogical confirmation of a near-
7 P:Fe = 1:2 limiting stoichiometric ratio in colloidal P-bearing ferrihydrite-like hydrous ferric oxide.
8 *Geochim. Cosmochim. Acta* **73**, 364-376.
- 9 Tipping, E., Thompson, D.W., Woof, C. (1989). Iron oxide particulates formed by the oxygenation of
10 natural and model lakewaters containing Fe(II). *Arch. Hydrobiol. Suppl.* **115**, 59-70.
- 11 van Genuchten, C.M., Gadgil, A.J., Peña, J. (2014a). Fe(III) Nucleation in the Presence of Bivalent
12 Cations and Oxyanions Leads to Subnanoscale 7 Å Polymers. *Environmental Science &*
13 *Technology* **48**, 11828-11836.
- 14 van Genuchten, C.M., Peña, J., Amrose, S.E., Gadgil, A.J. (2014b). Structure of Fe(III) precipitates
15 generated by the electrolytic dissolution of Fe(0) in the presence of groundwater ions. *Geochim.*
16 *Cosmochim. Acta* **127**, 285-304.
- 17 Voegelin, A., Kaegi, R., Frommer, J., Vantelon, D., Hug, S.J. (2010). Effect of phosphate, silicate, and
18 Ca on Fe(III)-precipitates formed in aerated Fe(II)- and As(III)-containing water studied by X-ray
19 absorption spectroscopy. *Geochim. Cosmochim. Acta* **74**, 164-186.
- 20 Voegelin, A., Senn, A.-C., Kaegi, R., Hug, S.J., Mangold, S. (2013). Dynamic Fe-precipitate formation
21 induced by Fe(II) oxidation in aerated phosphate-containing water. *Geochim. Cosmochim. Acta*
22 **117**, 216-231.
- 23 Wang, J., Zhao, J., Ma, P., Ma, J., Yang, L., Bai, Y., Li, M., Niu, J. (2009). A novel type of
24 heteropolyoxoanion precursors $\{[\text{Ca}(\text{H}_2\text{O})]_6[\text{P}_4\text{M}_6\text{O}_{34}]_2\}^{12-}$ ($\text{M} = \text{W}^{\text{VI}}, \text{Mo}^{\text{VI}}$) constructed by two
25 $[\text{P}_4\text{M}_6\text{O}_{34}]^{12-}$ subunits via a rare hexa-calcium cluster. *Chemical Communications*, 2362-2364.
- 26 Waychunas, G.A., Kim, C.S., Banfield, J.F. (2005). Nanoparticulate iron oxide minerals in soils and
27 sediments: unique properties and contaminant scavenging mechanisms. *J. Nanopart. Res.* **2005**,
28 409-433.
- 29 Wilkie, J.A., Hering, J.G. (1996). Adsorption of arsenic onto hydrous ferric oxide: Effects of
30 adsorbate/adsorbent ratios and co-occurring solutes. *Coll. Surf. A* **107**, 97-110.
- 31 Wolthoorn, A., Temminghoff, E.J.M., van Riemsdijk, W.H. (2004). Colloid formation in groundwater
32 by subsurface aeration: characterisation of the geo-colloids and their counterparts. *Appl. Geochem.*
33 **19**, 1391-1402.
- 34 Wright, K., Hartmann, T., Fujita, Y. (2011). Inducing mineral precipitation in groundwater by addition
35 of phosphate. *Geochem Trans* **12**, 1-13.

7. TABLES

Table 1

Overview over combinations of background electrolytes and P/Fe ratios studied and analytical techniques used for solution analysis and precipitate characterization^a

Series ^b	(P/Fe) _{init} ^c (with Fe = 0.5 mM)											
	0.0	0.05	0.1	0.2	0.3	0.4	0.5	0.6	0.75	1.0	1.5	2.0
Na ^d	IKSX ^d	IKF	IKX	IKS ^d	IKX ^d	IK ^d	IKSX ^d	IK ^d	IKSXF ^d	IK ^d	IKXF ^d	IKS ^d
Ca	IKSX	IKF	IKX	IKS	IKX	IK	IKSX	IK	IKSXF	IK	IKXF	IKS
Mg	IK	IK	IK	IK	IK	IK	IK	IK	IK	IK	IK	IK
low Ca	IK	IK	IK	IK	IK	IK	IK	IK	IK	IK	IK	IK
Na+Si	IKD	IKF	IKD	IKD	IK	IKD	IK	IK	IKF	IK	IKF	IK
Ca+Si	IKD	IKF	IKD	IKD	IK	IKD	IK	IK	IKF	IK	IKF	IK

^a For each of the 72 combinations, the initial and final suspensions were analyzed by ICP-MS (unfiltered/filtered) (I), and the corresponding precipitates by Fe K-edge EXAFS (K) spectroscopy. Additionally, selected precipitates were studied by digestion (D), STEM (S), FTIR (F) and XRD (X).

^b Na: 8 mM NaHCO₃; Ca: 4mM Ca(HCO₃)₂; low Ca: 7 mM NaHCO₃ + 0.5 mM Ca(HCO₃)₂; Mg: 4 mM Mg(HCO₃)₂; Na+Si: 8 mM NaHCO₃ + 0.5 mM Na₂SiO₃; Ca+Si: 4 mM Ca(HCO₃)₂ + 0.5 mM Na₂SiO₃. Ca(HCO₃)₂ and Mg(HCO₃)₂ refer to CaCO₃ and MgO dissolved in CO₂-saturated water.

^c Molar phosphate/Fe(II) ratio in the starting solution.

^d Precipitates formed in Na electrolyte at 16 (P/Fe)_{init} from 0 to 1.91 with 1 mM initial Fe(II) have been investigated by Voegelin et al. (2013).

Table 2

Molar element/Fe ratios of Fe(III)-phosphate- and ferrihydrite-type precipitates.

	Fe(III)-phosphate			ferrihydrite	
	ICP-MS			ICP-MS and EXAFS LCF	
Series	(P/Fe) _{crit} ^a	(P/Fe) _{1.5} ^b	((Ca,Mg)/Fe) _{1.5} ^c	(P/Fe) _{((low)Ca)FeP*} ^d	(P/Fe) _{HFO, Fh-Si*} ^d
Na	0.52 (0.01)	0.63 (0.01)	---	0.52 (0.02)	0.22 (0.06)
Ca	0.86 (0.03)	0.99 (0.03)	0.63 (0.03)	0.83 (0.03)	0.21 (0.06)
Mg	0.66 (0.03)	0.71 (0.03)	0.25 (0.01)	0.67 (0.03)	0.23 (0.06)
low Ca	0.65 (0.02)	0.76 (0.02)	0.37 (0.01)	0.63 (0.01)	0.30 (0.05)
Na+Si	0.53 (0.01)	0.61 (0.01)	---	0.53 (0.02)	0.02 (0.05)
Ca+Si	0.87 (0.03)	1.03 (0.03)	0.76 (0.18)	0.81 (0.04)	0.00 (0.00)

^a Critical molar P/Fe ratio calculated by extrapolating the linear regression of (P/Fe)_{ppt} ratios at (P/Fe)_{init} of ~1.0, ~1.5 and ~2.0 to condition (P/Fe)_{ppt} = (P/Fe)_{init}. Numbers in parentheses correspond to the standard error values for the coefficients calculated by the linear regression.

^b (P/Fe)_{ppt} at (P/Fe)_{init} = 1.5 calculated by interpolating the linear regression of (P/Fe)_{ppt} ratios at (P/Fe)_{init} of ~1.0, ~1.5 and ~2.0 to (P/Fe)_{init} = 1.5.

^c Molar (Ca/Fe)_{ppt} and (Mg/Fe)_{ppt} at (P/Fe)_{init} = 1.5 calculated by interpolating the respective linear regressions for (Ca/Fe)_{ppt} and (Mg/Fe)_{ppt} at (P/Fe)_{init} of ~1.0, ~1.5 and ~2.0 to (P/Fe)_{init} = 1.5. (Ca/Fe)_{ppt} of samples from low Ca, Ca and Ca+Si electrolytes derived from suspension data (total initial and final filtered concentrations), (Mg/Fe)_{ppt} of samples from Mg electrolyte from digestion of dried precipitate.

^d Molar (P/Fe)_{ppt} of ((low)Ca)FeP* and of HFO or Fh-Si* calculated from multiple linear regressions of (P/Fe)_{ppt} over LCF-derived ((low)Ca)FeP* and HFO or Fh-Si* fractions for (P/Fe)_{init} from ~0.2 to ~0.75 (derivation of ((low)Ca)FeP* and HFO or Fh-Si* described in section 3.2.2 and 3.2.3, details on the derivation of the respective P/Fe ratios in section EA11).

Table 3

Molar (Ca/Fe)_{ppt}, (P/Fe)_{ppt} and (Si/Fe)_{ppt} of precipitates formed in Na+Si and Ca+Si electrolytes determined by acid digestion of precipitates.

Series	(P/Fe) _{init}	Ca/Fe	P/Fe	Si/Fe	Oxy/Fe ^a
Na+Si	0.00	---	0.00	0.11	0.12
	0.10	---	0.09	0.09	0.20
	0.20	---	0.19	0.08	0.28
	0.41	---	0.38	0.03	0.42
Ca+Si	0.00	0.22	0.00	0.10	0.12
	0.10	0.21	0.10	0.10	0.21
	0.20	0.25	0.19	0.08	0.29
	0.41	0.33	0.38	0.06	0.46

^a Oxy/Fe = (P+Si+As)/Fe; As/Fe ~0.014 in all treatments.

- 1 Table 4
- 2 Endmember-spectra derived from averaged sample spectra. Characterization by LCF based on reference spectra and indication of their use
- 3 for LCF analysis of samples from different background electrolytes.

	LCF analysis of endmember spectra based on reference spectra							Endmember spectra used for LCF of spectra from different electrolytes					
	Lp	Fh	HFO	FeP	Mitr	Sum	NSSR (x1000)	Na	Ca	lowCa	Mg	Na+Si	Ca+Si
FeP*	--	--	--	1.00	--	1.01	4.63	X			X	X	
CaFeP*	--	--	--	0.86	0.14	1.03	4.00		X				X
lowCaFeP*	0.60 FeP*+ 0.40 CaFeP*					0.98	1.36			X			
pcLp*	0.67	0.33	--	--	--	1.10	3.10	X	X	X	X		
Fh-Si*	--	0.52	0.21	0.27	--	1.04	5.64					X	X
HFO ^a	--	--	1.00		--	1.00	0.00	X	X	X	X		

4 ^a HFO reference spectrum included to account for transformation of (Ca)FeP in Si-free series (see section 3.2.2.4).

5

8. FIGURES

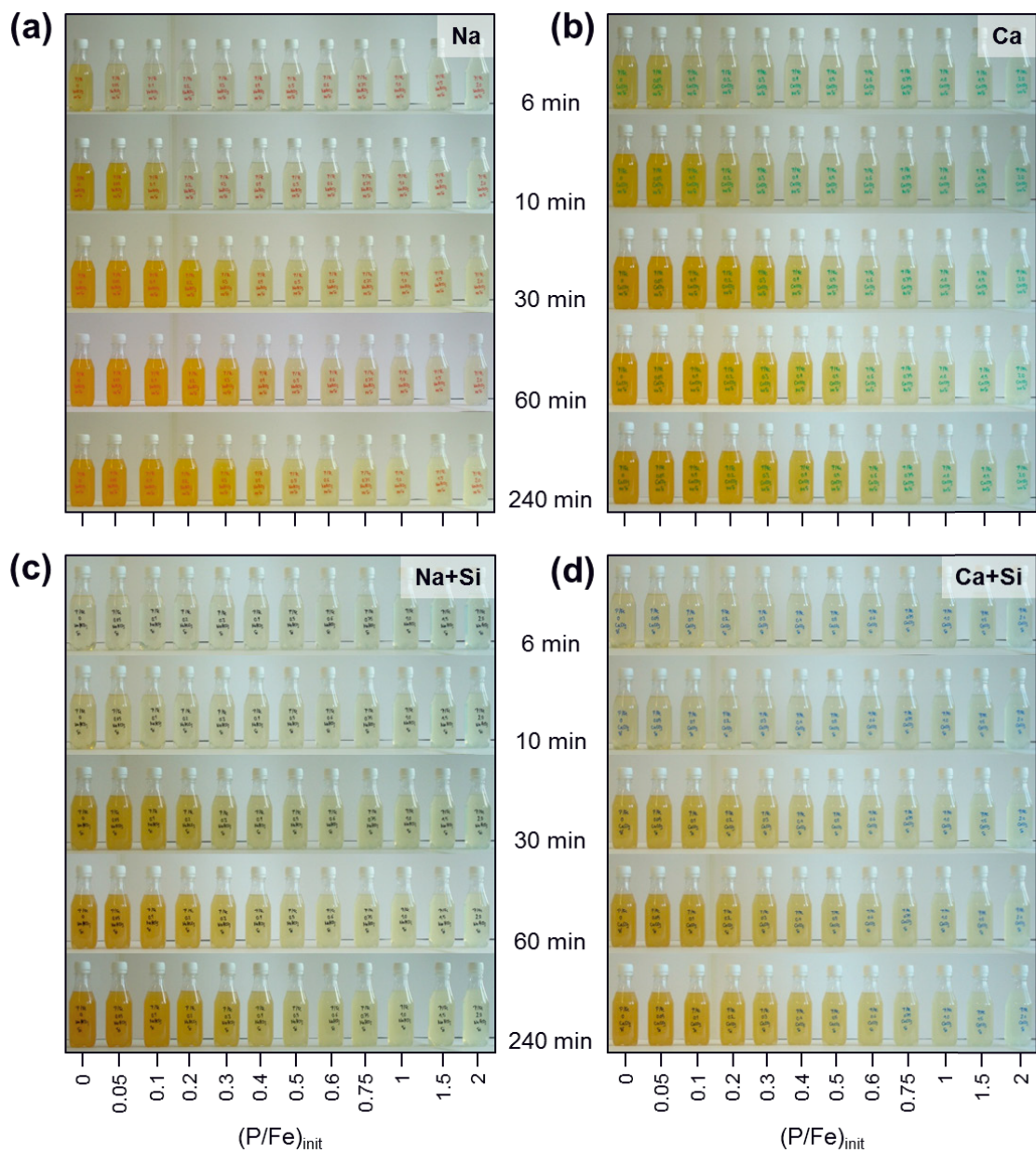


Fig. 1. Evolution of suspension color as a function of time after Fe(II) addition and of initial dissolved P/Fe ratio $(P/Fe)_{init}$ in the background electrolytes (a) Na, (b) Ca, (c) Na+Si and (d) Ca+Si.

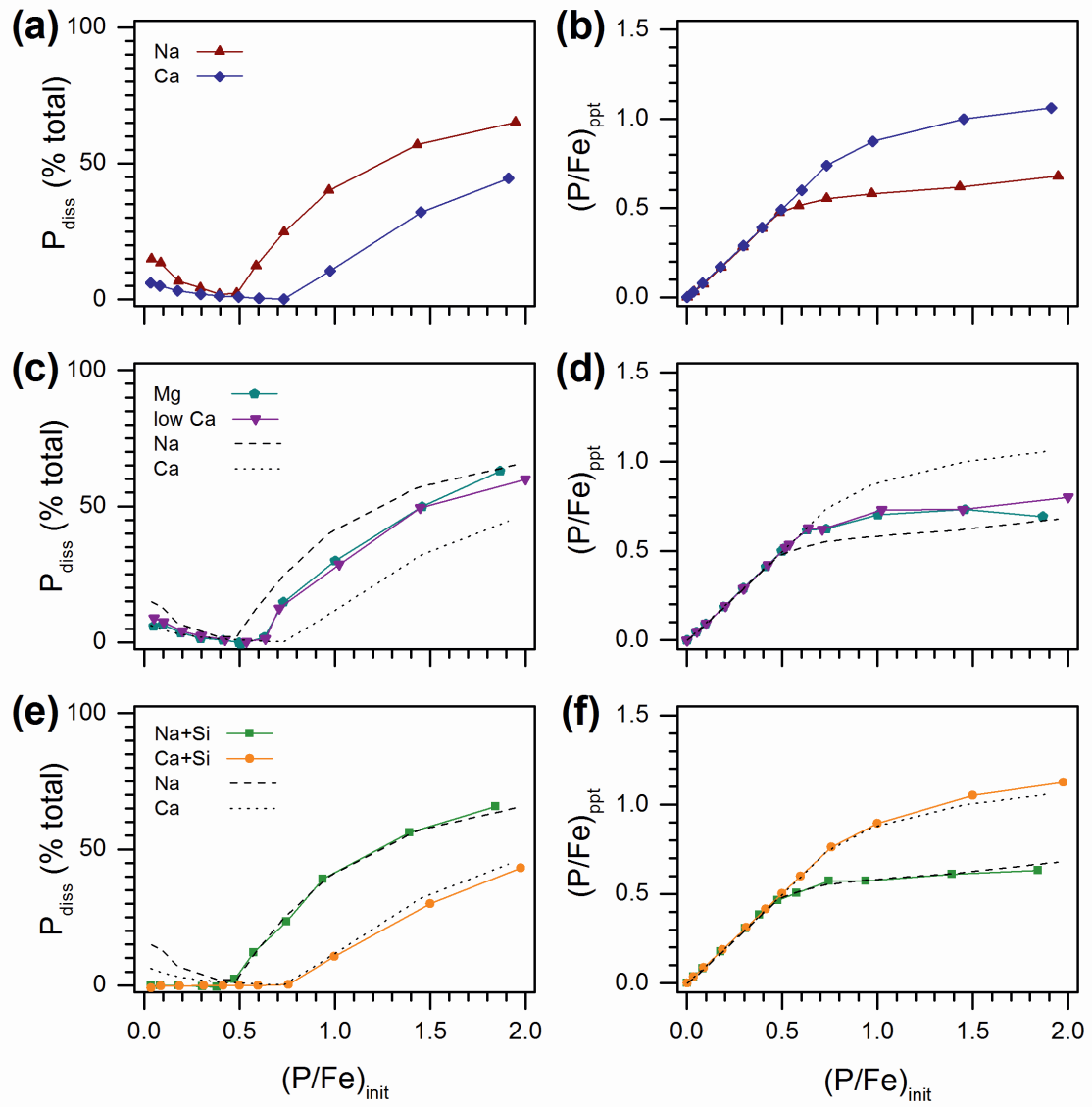


Fig. 2. (a,c,e) Fraction of dissolved phosphate and (b,d,f) molar precipitate P/Fe ratio in the reaction suspensions after 4 hours as a function of molar initial dissolved P/Fe ratio in (a,b) Na and Ca, (c,d) low Ca and Mg and (e,f) Na+Si and Ca+Si background electrolytes. For comparison, dashed and dotted lines in panels c-f indicate data for Na and Ca electrolytes, respectively.

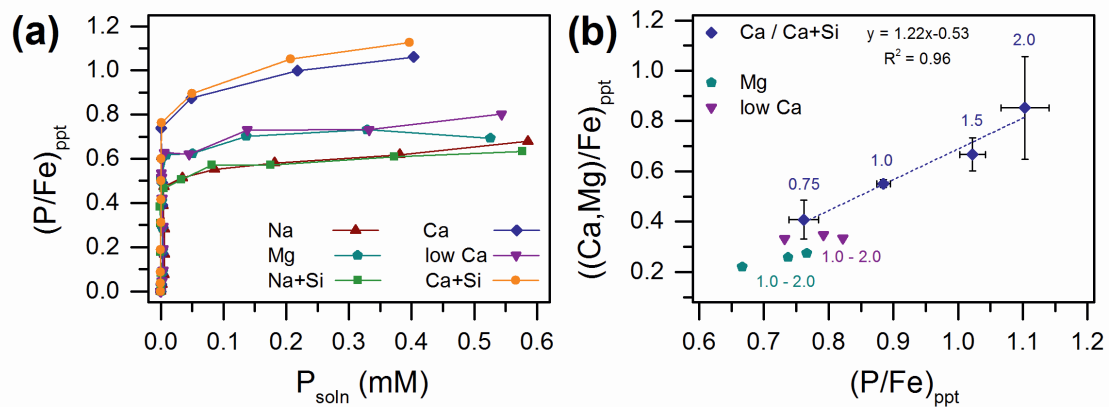


Fig. 3. (a) Molar precipitate P/Fe ratios $((P/Fe)_{ppt})$ as a function of dissolved phosphate concentrations after 4 h reaction time (P_{soln}). (b) Molar $(Ca/Fe)_{ppt}$ or $(Mg/Fe)_{ppt}$ ratios versus $(P/Fe)_{ppt}$ ratios for precipitates formed in the Ca and Ca+Si electrolytes at $(P/Fe)_{init}$ of 0.75, 1, 1.5 and 2 (error bars correspond to standard deviation from 3-6 samples) and for precipitates formed in low Ca and Mg electrolytes at $(P/Fe)_{init}$ from 1 to 2 (detailed results in Table EA6).

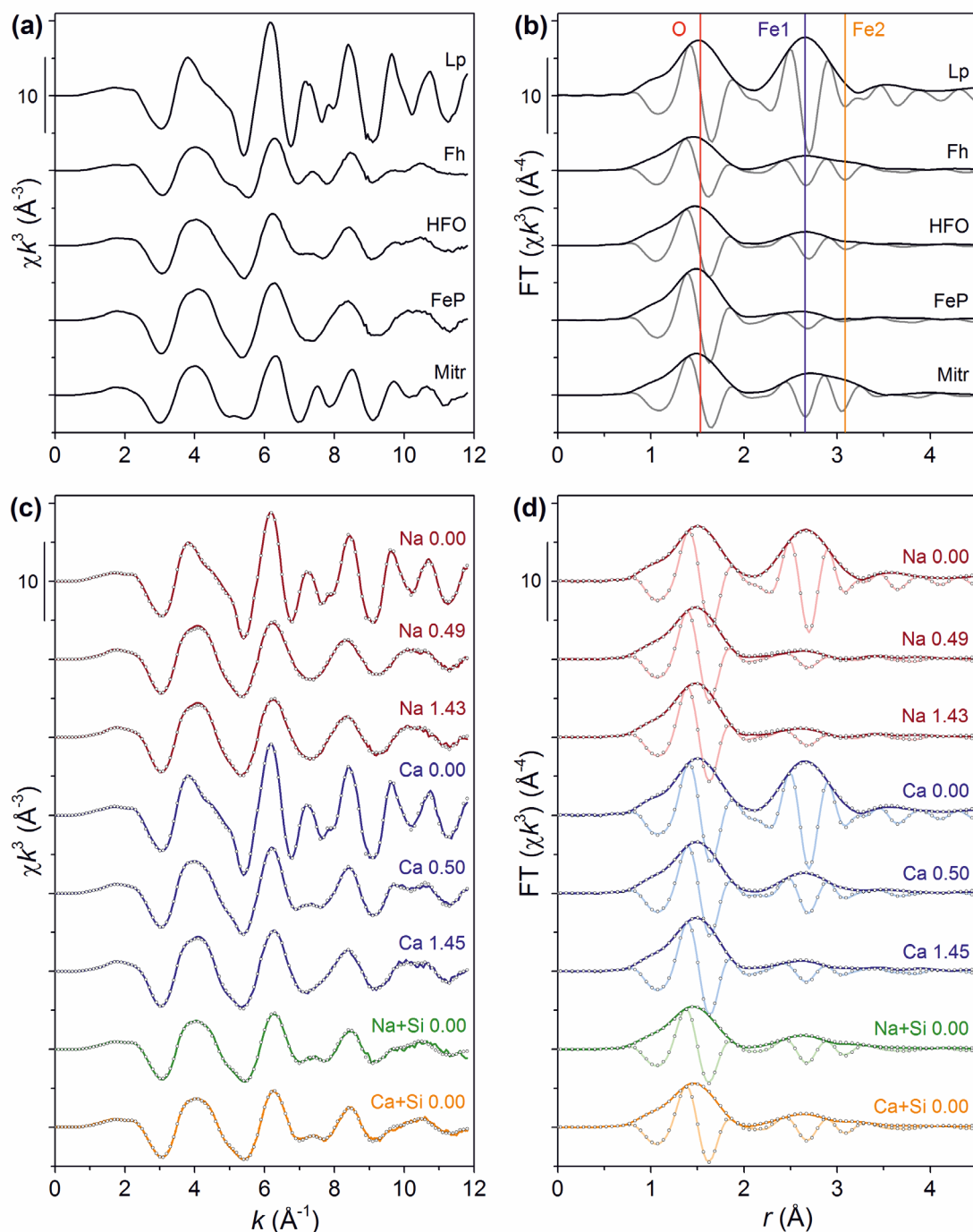


Fig. 4. (a) Fe K-edge EXAFS spectra of references used for linear combination fitting (LCF) and (b) their respective Fourier-transformed spectra (magnitude (black solid lines) and imaginary part (grey solid lines)). (c) Fe K-edge EXAFS spectra of selected samples (solid lines) and the corresponding LCF spectra (open circles) and (d) the respective Fourier-transformed spectra. Lp = lepidocrocite; Fh = ferrihydrite; HFO = hydrous ferric oxide; FeP = amorphous Fe(III)-phosphate; Mitr = mitridatite (crystalline $\text{Ca}_2\text{Fe}_3(\text{PO}_4)_3\text{O}_2(\text{H}_2\text{O})_3$). Reference spectra Lp, Fh (2L-Fh), HFO (fHFO-Si) and FeP (Fe4-P4) are from Voegelin et al. (2010) (original labels in parentheses).

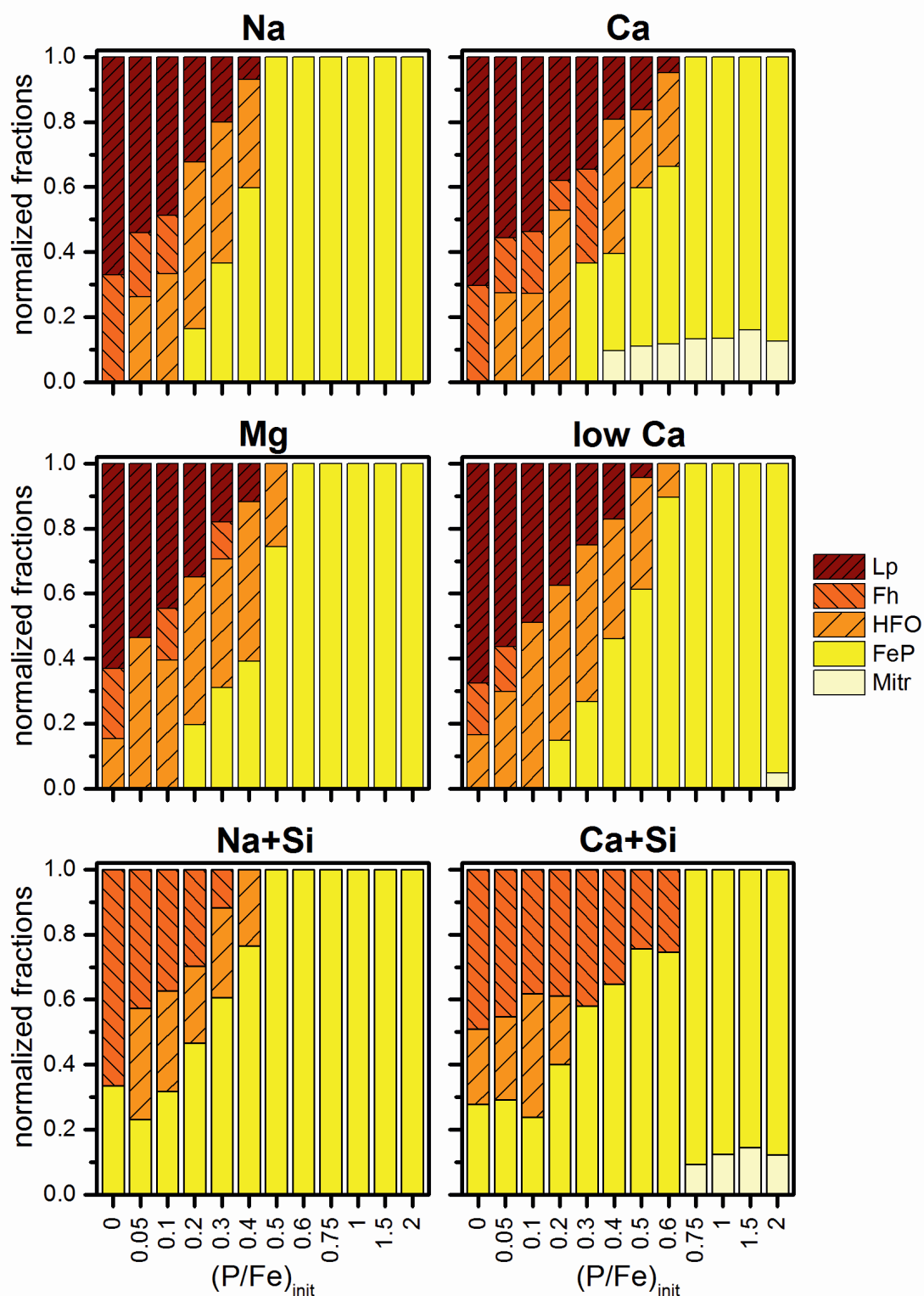


Fig. 5. Results from LCF analysis of Fe K-edge EXAFS spectra of Fe(III)-precipitates formed in Na, Ca, Mg, low Ca, Na+Si and Ca+Si electrolyte. The fitted fractions were normalized to a sum of 1. The detailed LCF results are provided in Tables EA3-5. Statistical fit uncertainties were typically (90th percentile) <0.03 for Lp, <0.04 for Fh and HFO, <0.02 for FeP and <0.01 for Mitr. Detailed absolute and relative uncertainties of fits are summarized in Table EA2.

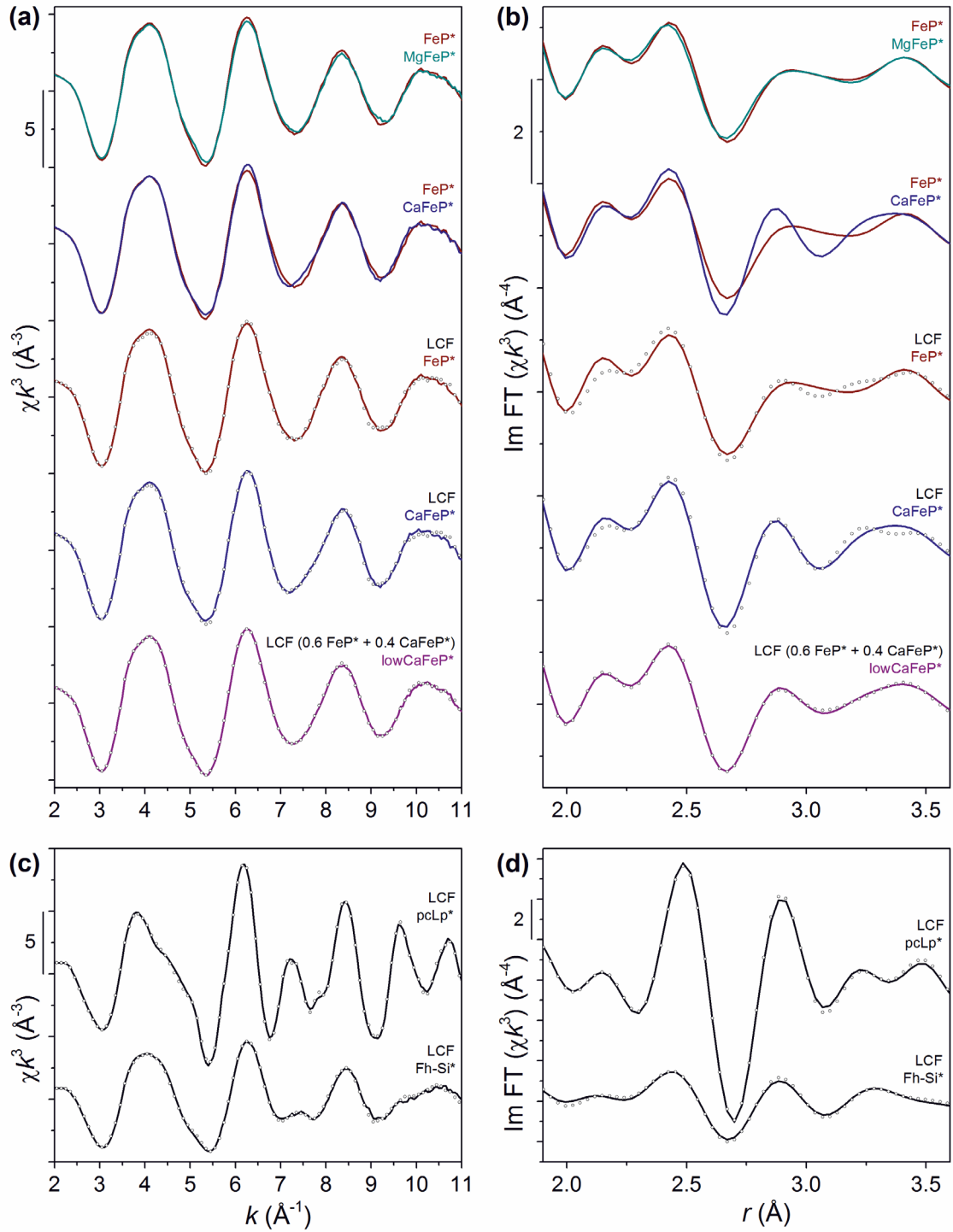


Fig. 6. (a, b) Comparison of the Fe K-edge EXAFS endmember spectrum FeP* with the spectrum MgFeP* and the endmember spectrum CaFeP* and of the spectra FeP*, CaFeP* and lowCaFeP* (solid lines) with reconstructed LCF spectra (open circles) in k -space and r -space (imaginary part of Fourier-transformed spectrum). (c, d) Comparison of the endmember spectra pcLp* and Fh-Si* (solid lines) with reconstructed LCF spectra (open circles) in k -space and r -space (imaginary part of Fourier-transformed spectrum). All LCF results listed in Table 4.

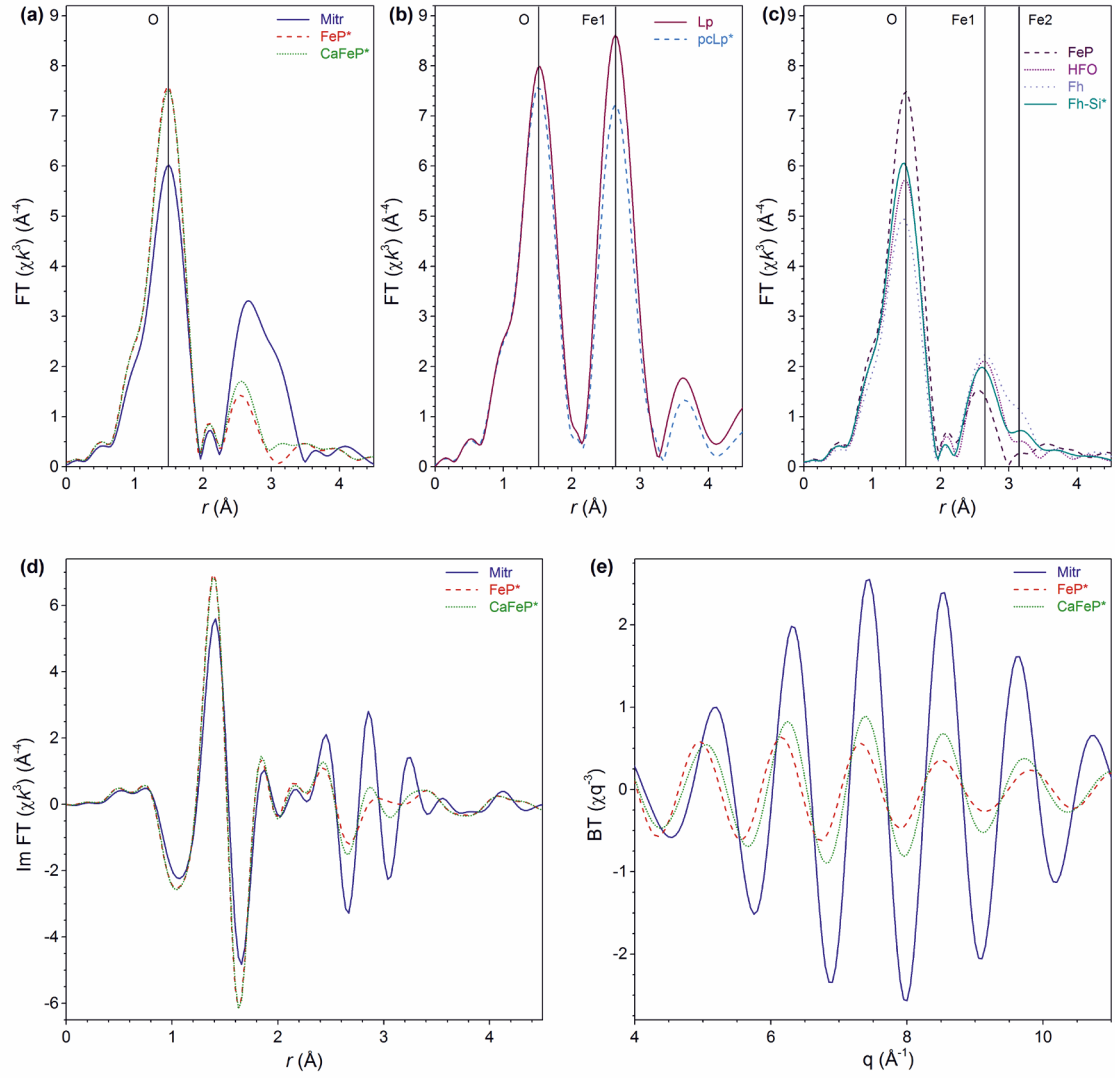


Fig. 7. Comparison of the Fe K-edge EXAFS endmember spectra with reference spectra. Magnitude of Fourier-transformed spectra of (a) Mitr, FeP* and CaFeP*, (b) Lp and pcLp* and (c) FeP, HFO, Fh and Fh-Si*. (d) Imaginary part of Fourier-transformed spectra of Mitr, FeP* and CaFeP* and (e) back-transform over r -range 2.3-3.4 Å.

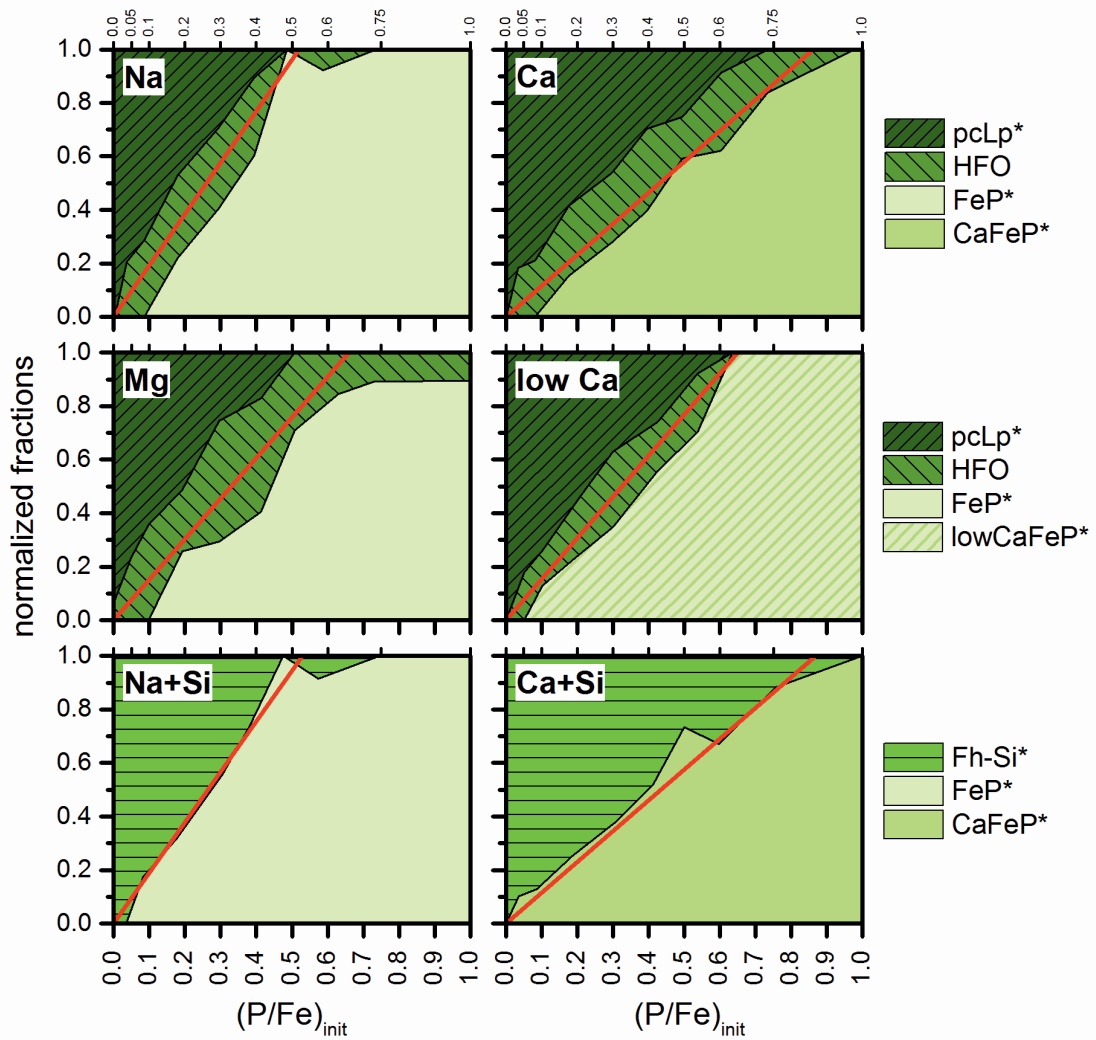


Fig. 8. Fractions pcLp*, HFO or Fh-Si* and FeP* / CaFeP* or lowCaFeP* derived by LCF analysis of the sample spectra with endmember-spectra (sections 3.2.2 and 3.2.3). The fractions for individual samples are listed in Tables EA3-5 and shown in Fig. EA9. The red solid lines extend from the origin to unity at $(P/Fe)_{crit}$ (Table 2). They represent the FeP*, CaFeP* or lowCaFeP* fractions that should occur if initially formed (Ca-)Fe(III)-phosphate at $(P/Fe)_{init} < (P/Fe)_{crit}$ had a $(P/Fe)_{ppt}$ of $(P/Fe)_{crit}$ and did not transform during continuing Fe(II) oxidation after dissolved phosphate depletion. ((low)Ca)FeP* fractions lower than the red line suggest that some (Ca-)Fe(III)-phosphate transformation occurred during continuing Fe(II) oxidation after phosphate depletion. Statistical fit uncertainties were typically (90th percentile) 0.00 for pcLp* and Fh-Si*, <0.03 for HFO and <0.02 for FeP*, CaFeP* and lowCaFeP*. The absolute and relative uncertainties of the fits are summarized in Table EA2.

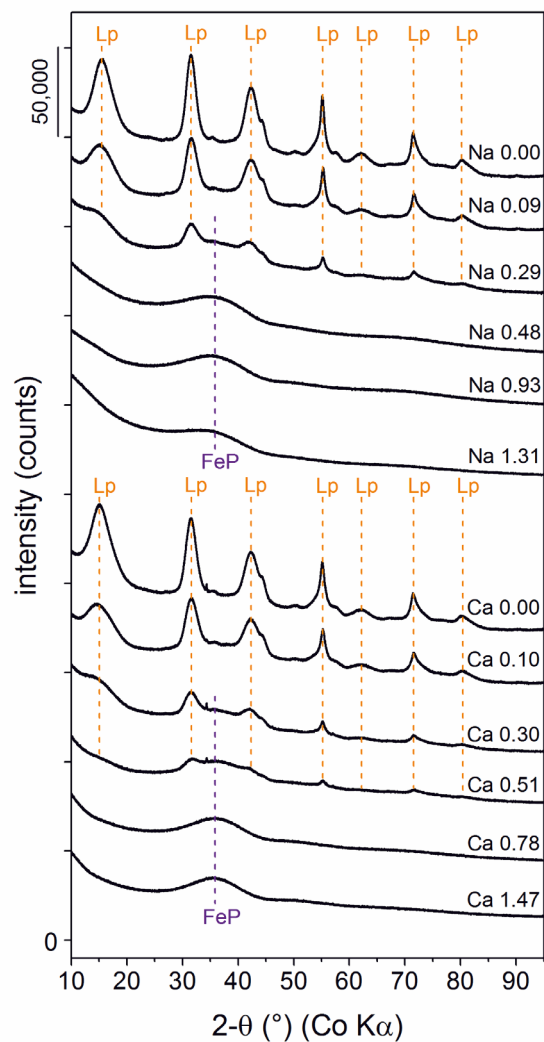


Fig. 9. X-ray diffraction spectra of selected Fe(III)-precipitates formed in Na and Ca electrolyte at different $(P/Fe)_{init}$. Dashed vertical lines correspond to dominant peaks of lepidocrocite (Lp) and Fe(III)-phosphate (FeP).

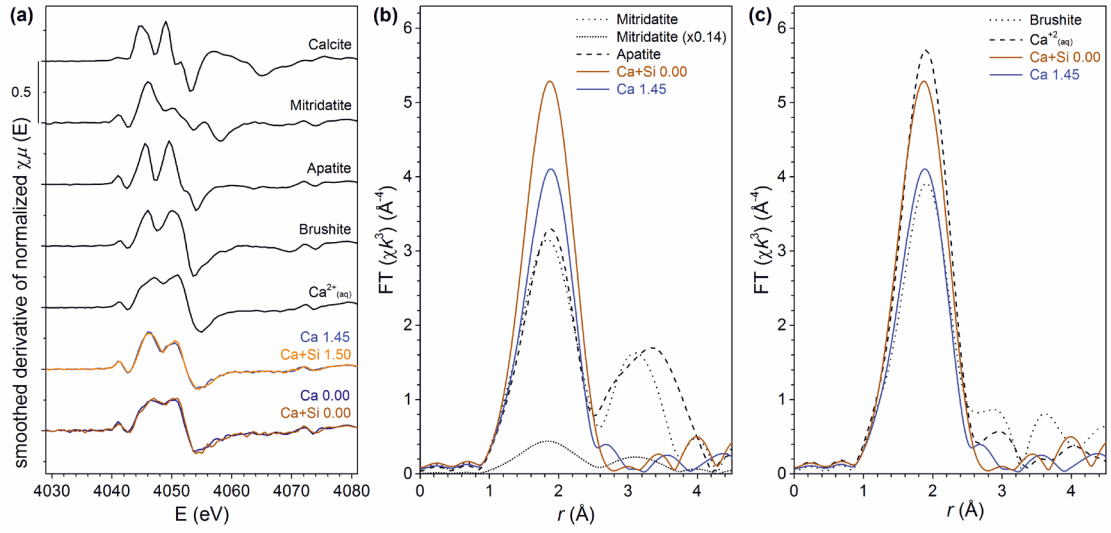


Fig. 10. (a) First-derivative Ca K-edge XANES spectra of reference materials and the samples formed at $(\text{P/Fe})_{\text{init}}$ of 0 and ~ 1.5 in the Ca and Ca+Si electrolytes. (b,c) Comparison of the Fourier-transformed EXAFS spectra of the samples Ca+Si 0.00 and Ca 1.45 to the reference spectra of mitridatite, apatite, brushite and aqueous Ca^{2+} . The normalized XANES and the EXAFS spectra are shown in Fig. EA12.

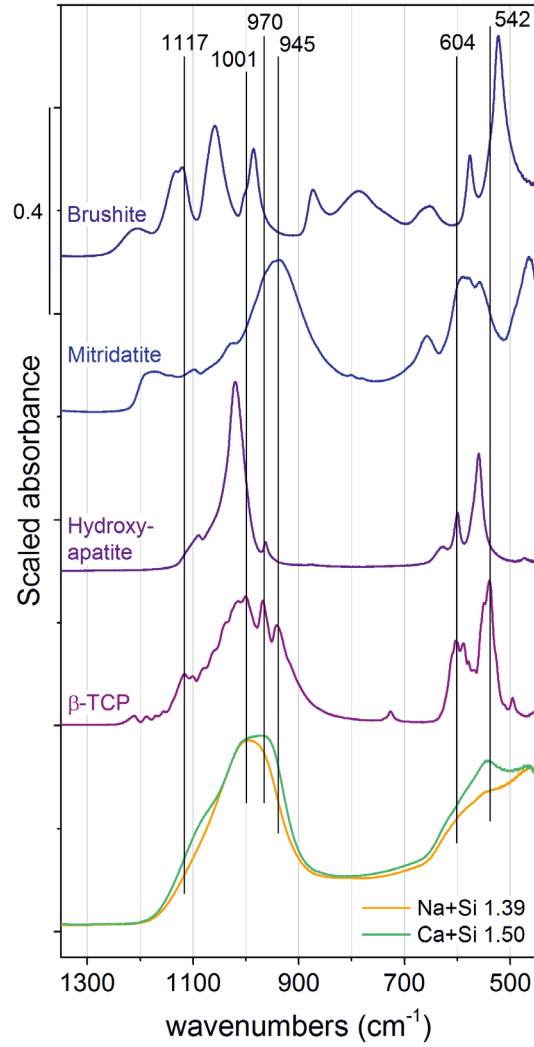


Fig. 11. Fourier-transform IR spectra of precipitates formed at high $(P/Fe)_{init}$ in Na+Si and Ca+Si electrolyte. The sample spectra were scaled and the reference spectra offset by 0.4 absorbance units for clarity. A larger set of FTIR reference and sample spectra is shown and discussed in section EA13.

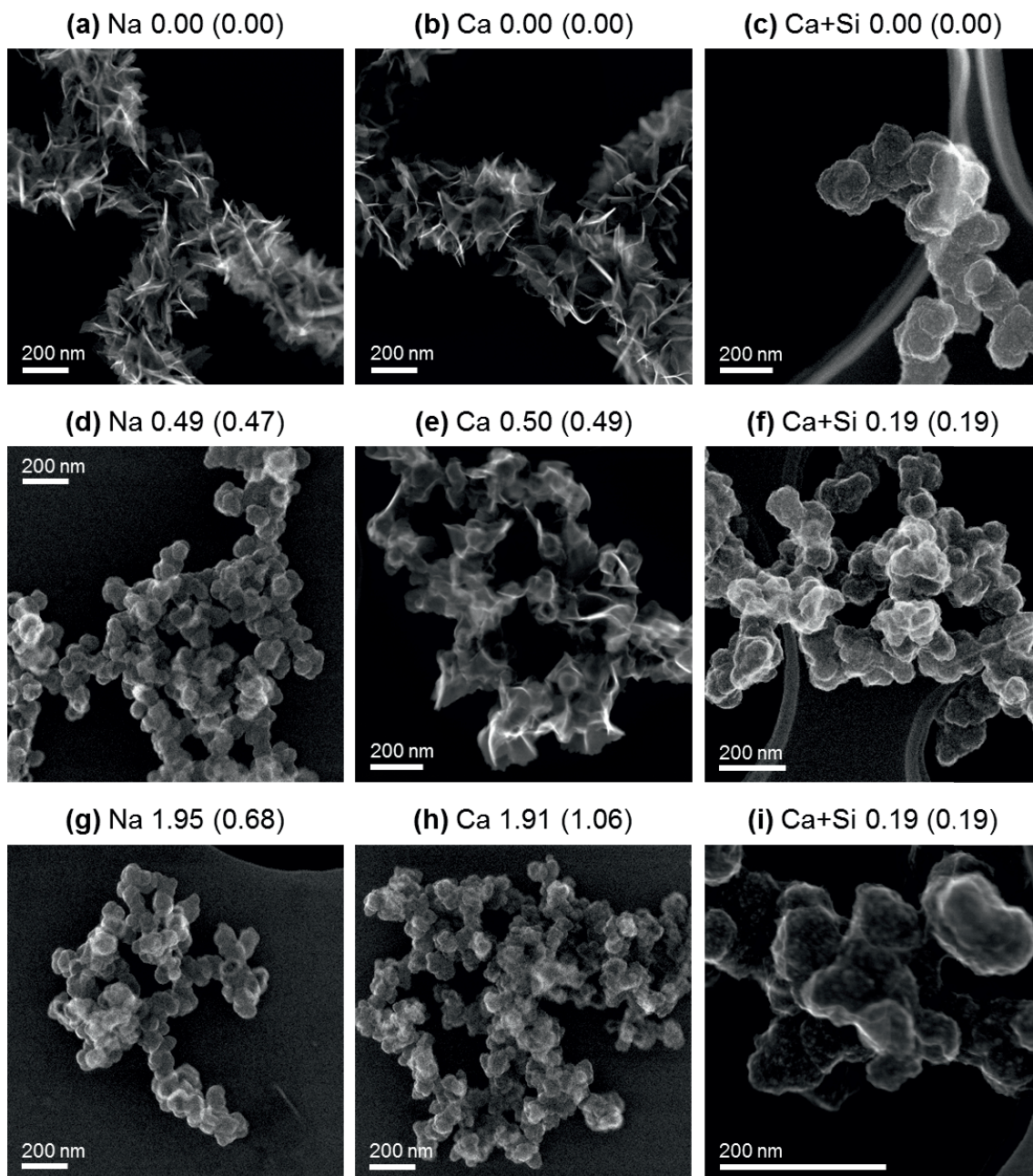


Fig. 12. Secondary electron (SE) STEM images indicating the morphology of selected Fe(III)-precipitates formed in (a,d,g) Na-, (b,e,h) Ca- and (c,f,i) Ca+Si-electrolyte at different $(P/Fe)_{init}$ ($(P/Fe)_{ppt}$ in parentheses). The corresponding high-angle annular dark-field (HAADF) images are shown in Fig. EA14.

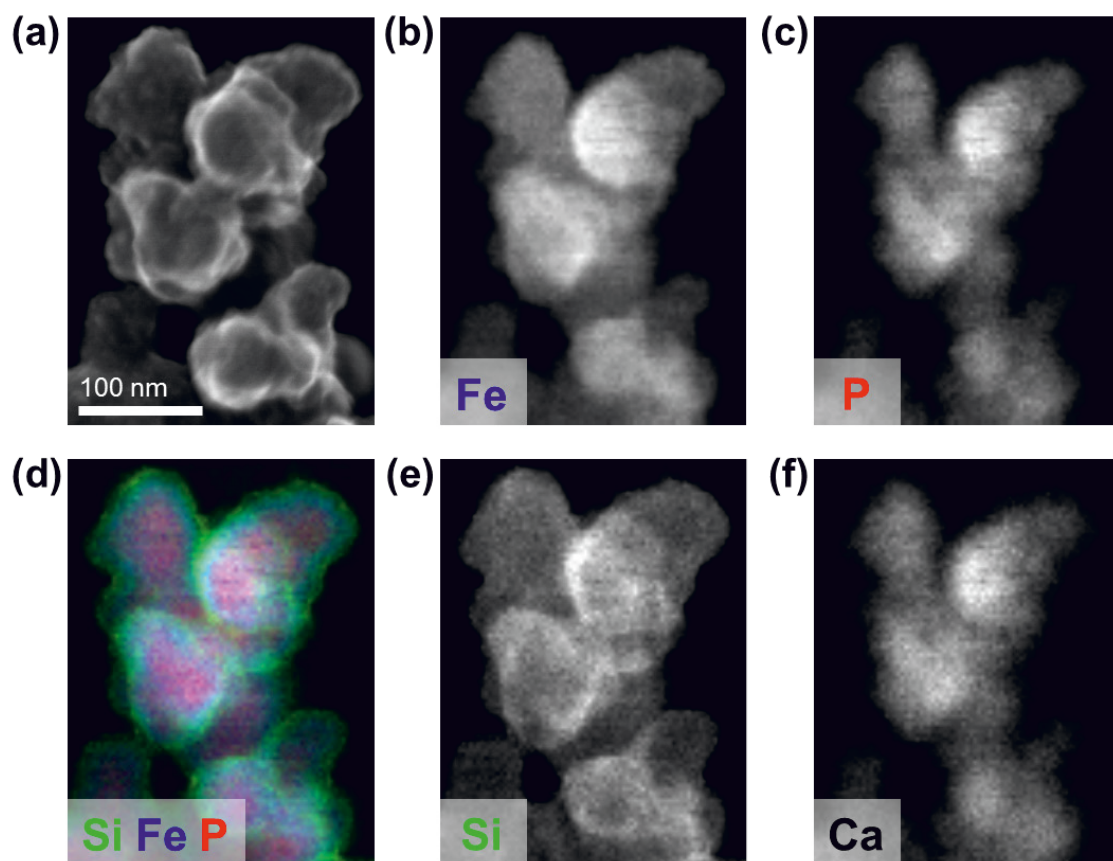


Fig. 13. (a) SE image , element distribution maps for (b) Fe, (c) P, (e) Si and (f) Ca and (d) the resulting tricolor map for Fe, P and Si for Fe(III)-precipitate Ca+Si 0.19.

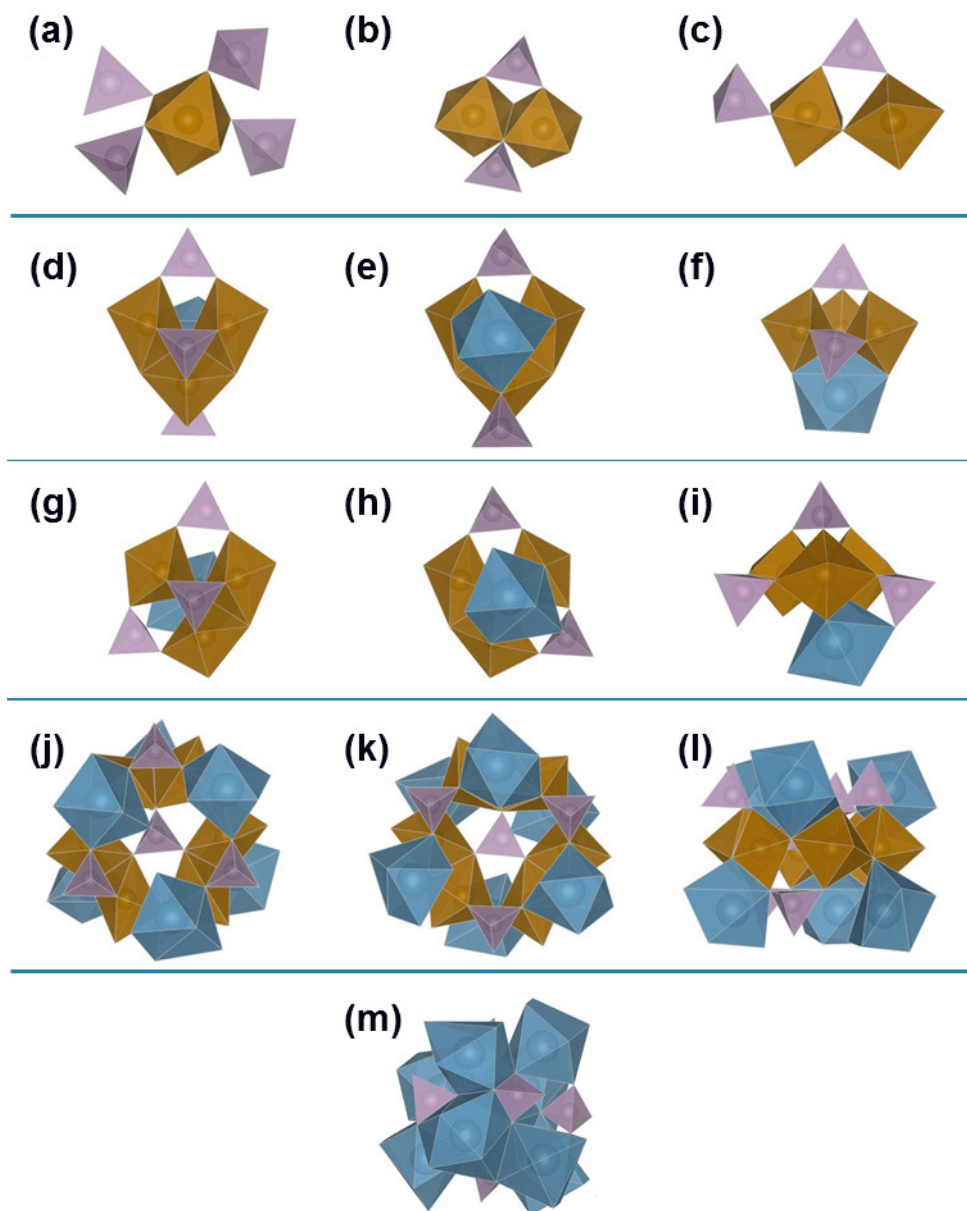


Fig. 14. Polyhedral representation of (a) monomeric Fe with corner-sharing phosphate, (b) edge-sharing Fe dimer (Fe-Fe ~ 3.0 Å) and (c) corner-sharing Fe dimer (Fe-Fe ~ 3.6 Å) with single and double corner-sharing (bridging) phosphate, of (d-f) and (g-i) two smallest-possible mitridatite-like Ca-Fe(III)-polymers viewed from different sides, of (j-l) mitridatite-like polymer composed of three edge-sharing Fe dimers linked via corners viewed from top, bottom and side and of (m) apatite-like Ca-phosphate polymer. Fe octahedra are shown in brown, phosphate tetrahedra in violet, and Ca polyhedra in blue. Mitridatite-like polymers based on mitridatite structure (Moore and Araki, 1977) (Fig. EA1). Polymers visualized using VESTA (Momma and Izumi, 2011).






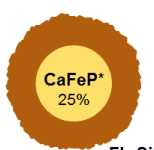
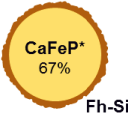

	$(P/Fe)_{init} = 0.0$	$(P/Fe)_{init} = 0.2$	$(P/Fe)_{init} = 0.6$	$(P/Fe)_{init} = 1.5$
(a) Na electrolyte $(Si/Fe)_{init} = 0$ $(P/Fe)_{ppt}$ $P_{dissolved} \text{ (mM)}$	 0.00 --	 0.17 0.00	 0.51 0.04	 0.62 0.38
(b) Ca+Si electrolyte $(Si/Fe)_{init} = 1$ $(P/Fe)_{ppt}$ $P_{dissolved} \text{ (mM)}$	 0.00 --	 0.19 <1.5·10⁻⁴	 0.60 <1.5·10⁻⁴	 1.05 0.21

Fig. 15. Schematic representation of the different types of Fe(III)-precipitates formed by Fe(II) oxidation in silicate- and Ca-free Na electrolyte and silicate- and Ca-containing Ca+Si electrolyte as a function of $(P/Fe)_{init}$ (pH 7.0, 8 mM HCO_3^- , 0.5 mM Fe(II)). (a) In the Na electrolyte, amorphous Fe(III)-phosphate (FeP^*) formed at $(P/Fe)_{init} > (P/Fe)_{crit}$. At $(P/Fe)_{init} < (P/Fe)_{crit}$, initially formed Fe(III)-phosphate has (partly) transformed into a phosphate-saturated ferrihydrite-type precipitate (HFO) which was surrounded by poorly crystalline lepidocrocite ($pcLp^*$). At $(P/Fe)_{init} = 0$, only poorly crystalline lepidocrocite formed. (b) In the Ca+Si electrolyte, amorphous Ca-Fe(III)-phosphate ($CaFeP^*$) formed at $(P/Fe)_{init} > (P/Fe)_{crit}$. Below $(P/Fe)_{crit}$, initially formed Ca-Fe(III)-phosphate was surrounded by silicate-containing ferrihydrite ($Fh-Si^*$) with $Si/Fe \sim 0.1$. At $(P/Fe)_{init} = 0$, only ferrihydrite formed.

Composition and structure of Fe(III)-precipitates formed by Fe(II) oxidation in water: Interdependent effects of phosphate, silicate and Ca

Anna-Caterina Senn^{a,b}, Ralf Kaegi^a, Stephan J. Hug^a, Janet G. Hering^{a,b,c},
Stefan Mangold^d, Andreas Voegelin^{a,*}

^a Eawag, Swiss Federal Institute of Aquatic Science and Technology, Ueberlandstrasse 133, CH-8600 Duebendorf, Switzerland

^b Department of Environmental Sciences, Institute of Biogeochemistry and Pollutant Dynamics, ETH, Swiss Federal Institute of Technology, Zurich, Switzerland

^c School of Architecture Civil and Environmental Engineering, EPFL, École Polytechnique Fédérale de Lausanne, Switzerland

^d Karlsruhe Institute of Technology, Institute of Synchrotron Radiation, Hermann-von-Helmholtz Platz 1, D-76344 Eggenstein-Leopoldshafen, Germany

* Corresponding author. E-mail address: andreas.voegelin@eawag.ch, phone +41 58 765 54 70, fax +41 58765 52 10

CONTENTS (24 pages, 7 tables, 15 figures)

EA1. Structure of mitridatite and shell-fit analysis of its Fe K-edge EXAFS	2
EA2. Recoveries of total Ca, Mg, P and Fe in suspensions after 4 h reaction time	5
EA3. Dissolved phosphate after 4 h reaction time	5
EA4. Precipitate P/Fe ratios, Fe K-edge EXAFS LCF results using reference and endmember spectra, and P/Fe ratios of endmembers	6
EA5. Molar P/Fe, Ca/Fe and Mg/Fe ratios of Fe(III)-phosphates	10
EA6. Principal component analysis (PCA)	12
EA7. Fe K-edge EXAFS sample spectra and reconstructed spectra based on LCF with reference spectra	14
EA8. Comparison of sample spectra averaged to obtain endmember spectra	15
EA9. Results of LCF analysis of Fe K-edge EXAFS spectra with endmember spectra	16
EA10. Comparison of Fe ₂ -sGW with CaFeP*	17
EA11. Molar P/Fe ratios of Fe(III)-phosphate- and ferrihydrite-type precipitate fractions	18
EA12. Ca K-edge XANES and EXAFS spectra and LCF analyses	19
EA13. FTIR analyses	20
EA14. Estimated Ca and phosphate fractions in Ca-Fe(III)-phosphate formed at (P/Fe) _{init} of 1.5 in Ca and Ca+Si electrolytes	22
EA15. Transmission electron microscopy	23
EA16. References	25

EA1. Structure of mitridatite and shell-fit analysis of its Fe K-edge EXAFS

The mitridatite structure has been resolved and described by (Moore and Araki, 1977). It consists of octahedral Fe(III) sheets with coordinated phosphate groups that are held together by a layer of Ca dimers (Fig. EA1). The octahedral Fe(III) sheets are composed of edge-sharing Fe(III)-nonamers that form trigonal rings. Each Fe atom is connected to 2 neighboring Fe atoms via edge-sharing linkage with an average Fe-Fe distance of ~ 3.05 Å. Owing to the shape of the nonamers and the linkage between nonamers, each Fe atom also shares 2 corners with neighboring Fe atoms at an average distance of ~ 3.44 Å. Phosphate is closely associated with the octahedral Fe(III) sheet, with each phosphate group being coordinated to 3 Fe atoms, bridging corner- and edge-sharing Fe octahedra. Consequently, each Fe atom is coordinated with 2 P at a distance of ~ 3.15 Å and 2 P at a distance of ~ 3.28 Å. The phosphate-coordinated octahedral Fe(III) sheets are connected via edge-sharing dimers of 7-fold O-coordinated Ca. As a results, each Fe is also coordinated to two Ca at an average distance of ~ 3.43 Å.

The mitridatite spectrum was modelled with a shell-fit using the software code Artemis (Ravel and Newville, 2005). All first-shell and second-shell single scattering paths were calculated using Feff 8 (Ankudinov et al., 1998) based on the structure of mitridatite (Moore and Araki, 1977). All first- and second-shell single scattering paths were included in the fit (Table EA1). The coordination numbers were fixed to their crystallographic values. The first-shell Fe-O distance and Debye Waller factor were fit. In the second-shell, paths for the same atom at similar distances were grouped, resulting in 5 paths with a coordination number of 2 each: Fe-Fe1 (~ 3.05 Å; edge-sharing), short Fe-P1 (~ 3.15 Å), long Fe-P2 (~ 3.28 Å), Fe-Fe2 (~ 3.44 Å; corner-sharing), and Fe-Ca (~ 3.43 Å; edge-sharing). The distances of second-shell paths were fixed to the average crystallographic values, and one common Debye Waller parameter for all second-shell paths was fit. In addition, the amplitude correction factor and energy shift were fit.

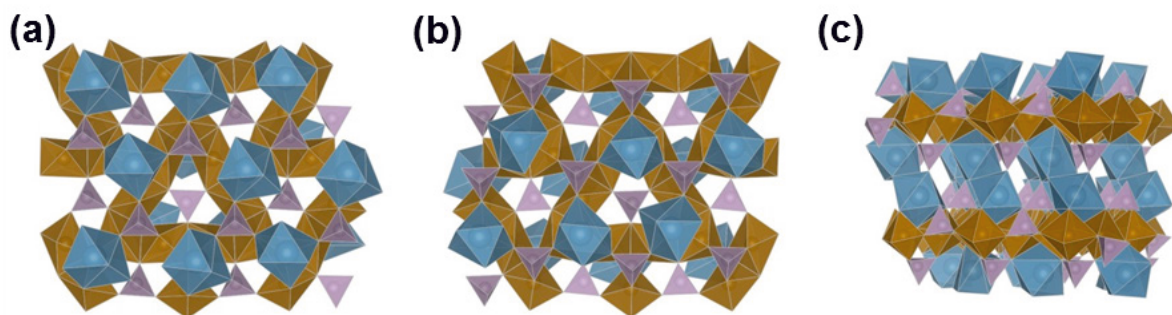


Fig. EA1. Polyhedral representation of (a,b) single mitridatite-type octahedral Fe sheet with associated phosphate and Ca viewed from top and bottom, and of (c) mitridatite structure viewed perpendicular to c-axis. Fe octahedra are shown in brown, phosphate tetrahedra in violet, and Ca polyhedral (7-fold O coordinated) in blue. Mitridatite-like polymer and mitridatite-type octahedral Fe sheet based on mitridatite structure (Moore and Araki, 1977). Polyhedral representations visualized using VESTA (Momma and Izumi, 2011).

Comparison of the experimental and fitted spectrum in Fig. EA2a showed that the structurally constrained fit model was able to satisfactorily reproduce the first- and second-shell peaks of the mitridatite reference spectrum. In Fig. EA2b, the imaginary parts of the 5 second-shell paths are shown. The 5 paths exhibit significant overlap with both constructive and destructive interference between individual paths. The numerous paths and their interferences limit the possibility to extract reliable structural information from shell-fits of spectra of analogous Ca-Fe(III)-phosphate phases with unknown local coordination.

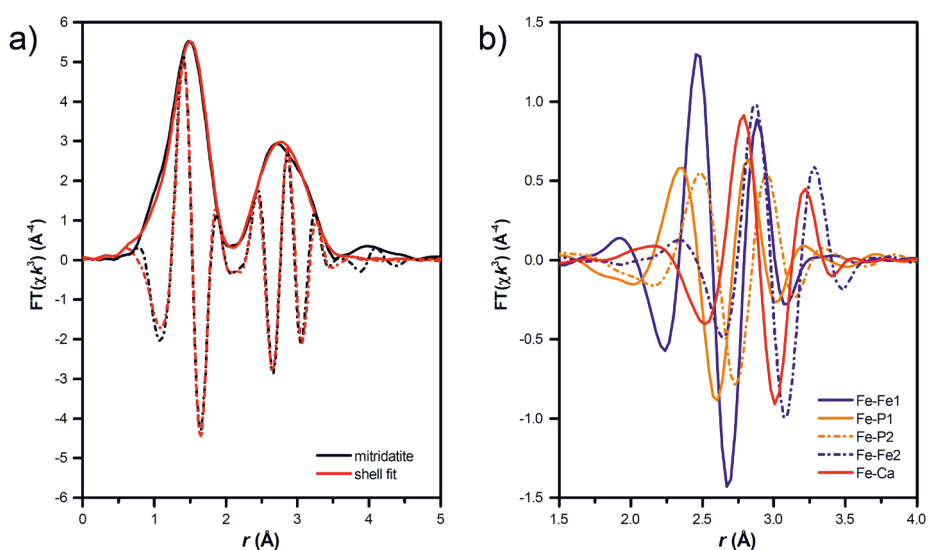


Fig. EA2. (a) Comparison of the experimental mitridatite spectrum (black) and the shell fit (red) based on parameters listed in Table EA1 (magnitude as solid line, imaginary part as dash-dotted line). (b) Imaginary parts of individual second-shell paths included in the fit.

Table EA1. Results from shell-fit analysis of the k^3 -weighted Fourier-transformed Fe K-edge EXAFS spectrum of mitridatite in r -space.^a

Path	^b CN	^c DW (\AA^{-2})	^d R (\AA)	^e S_0^2 ^f ΔE_0 (eV)	^g N _{idp} ^h N _{par}	ⁱ Red χ^2 ^j NSSR
Fe-O	6	0.009±0.001	2.00±0.01	0.69±0.07	13	775
Fe-Fe1	2	0.010±0.001	3.05	-11.4±0.5	5	0.05 %
Fe-P1	2	0.010±0.001	3.15			
Fe-P2	2	0.010±0.001	3.28			
Fe-Fe2	2	0.010±0.001	3.44			
Fe-Ca	2	0.010±0.001	3.43			

^aThe k^3 -weighted EXAFS spectrum was Fourier-transformed over k -range 2.5-10.5 \AA^{-1} (Kaiser-Bessel window; sill-width 2.5 \AA^{-1}) and analyzed over r -range 0.9-3.5 \AA . ^bCoordination numbers were fixed to values expected for mitridatite. ^cDebye Waller parameter was constrained to be the same for all second-shell paths (Fe-Fe1, Fe-P, Fe-P2, Fe-Fe2, Fe-Ca) ^dRadial distance, for second-shell paths fixed to average of their crystallographic values. ^eAmplitude correction factor. ^fEnergy shift. ^gNumber of independent data points. ^hNumber of adjustable parameters. ⁱReduced χ^2 . ^jNormalized sum of squared residuals (NSSR= $\sum(\text{data}_i - \text{fit}_i)^2 / \sum \text{data}_i^2$).

EA2. Recoveries of total Ca, Mg, P and Fe in suspensions after 4 h reaction time

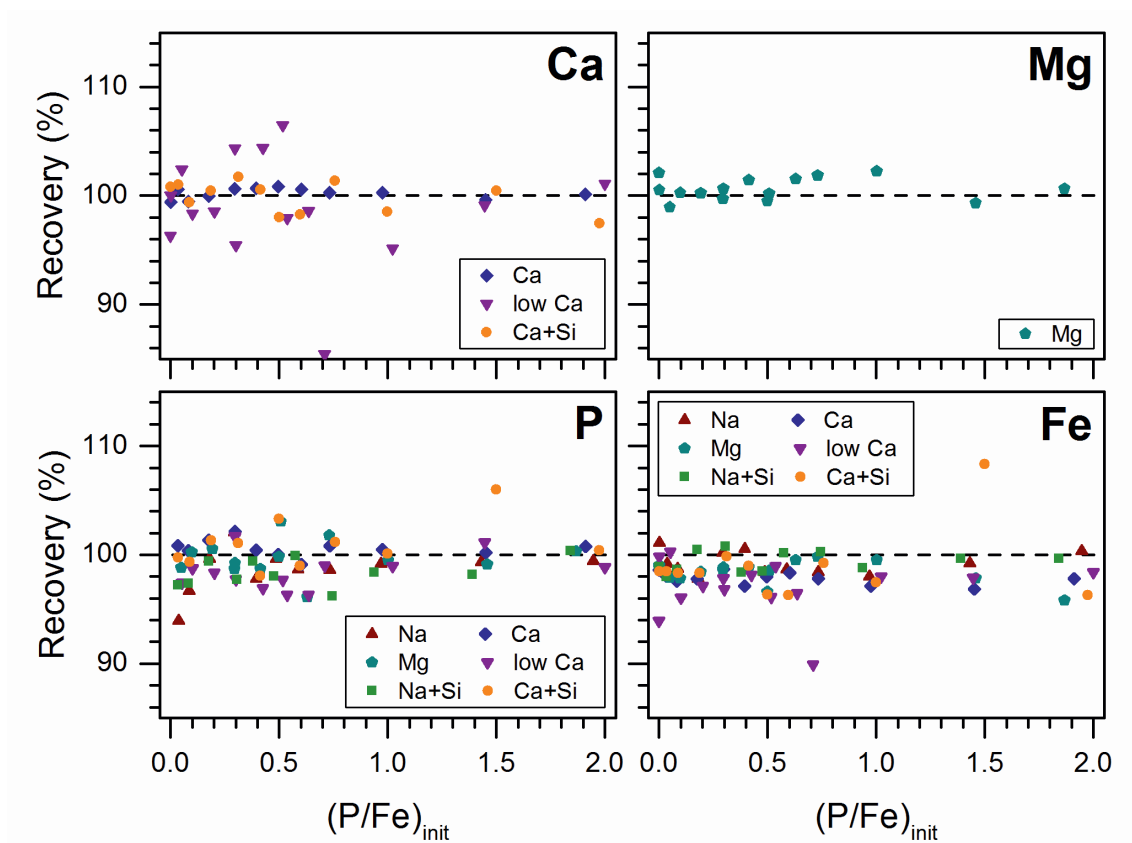


Fig. EA3. Total element recoveries in the reaction suspensions after 4 hours for the six different background electrolytes. Calculated by dividing total Ca, P and Fe concentrations after 4 hours ($[unfilt]_{end}$) by total initial Ca, P and Fe concentrations ($[unfilt]_{init}$), measured by ICP-MS.

EA3. Dissolved phosphate after 4 h reaction time

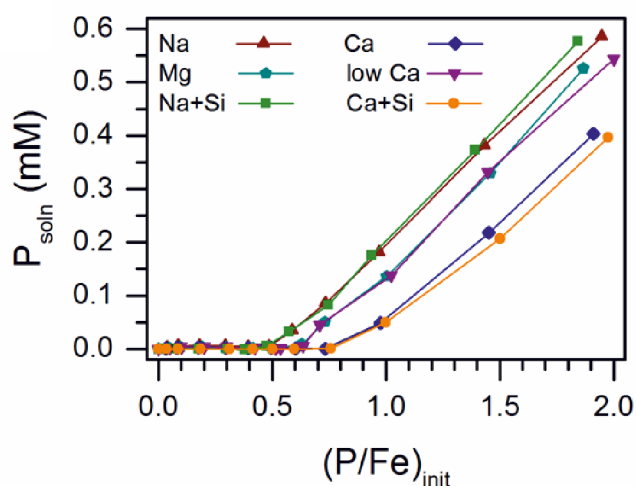


Fig. EA4. Dissolved phosphate concentrations after 4 h reaction time (P_{soln}) as a function of the initial molar (P/Fe) ratio $((P/Fe)_{init})$.

EA4. Precipitate P/Fe ratios, Fe K-edge EXAFS LCF results using reference and endmember spectra, and P/Fe ratios of endmembers

In Tables EA3 to EA5, initial and precipitate P/Fe ratios obtained by ICP-MS and Fe K-edge EXAFS LCF results obtained with reference spectra (Mitr, FeP, HFO, Fh, Lp) and with endmember spectra (FeP*, CaFeP*, lowCaFeP*, Fh-Si*, pcLp*) are listed (sections 3.2.2 and 3.2.3 in the manuscript). Absolute and relative uncertainties for individual reference or endmember fractions derived from LCF are summarized in Table EA2 (average, standard deviation, 90th percentile and maximum of absolute and relative uncertainty for each reference or endmember fraction). In general, the absolute and relative fit uncertainties were low, with 4 exceptions related to fits with reference spectra: inclusion of Fh in best LCF of samples Ca 0.18 and Na+Si 0.31, and of Lp in the best LCF of samples Na 0.39 and low Ca 0.54.

Table EA2. Absolute and relative uncertainties in linear combination fits based reference or endmember spectra^a: Average, standard deviation, 90th percentile and maximal uncertainty of each reference (considering best LCF where reference was included).

	LCF based on reference spectra										LCF based on endmember spectra											
	Mitr		FeP		HFO		Fh		Lp		FeP*		CaFeP*		lowCaFeP*		HFO		Fh-Si*		pcLp*	
	abs	rel	abs	rel	abs	rel	abs	rel	abs	rel	abs	rel	abs	rel	abs	rel	abs	rel	abs	rel	abs	rel
Average	0.01	11%	0.01	3%	0.03	10%	0.03	13%	0.02	10%	0.01	3%	0.01	3%	0.01	4%	0.02	10%	0.00	1%	0.00	1%
Standard deviation	0.00	5%	0.01	4%	0.01	5%	0.01	9%	0.02	16%	0.01	4%	0.01	3%	0.01	6%	0.01	6%	0.00	4%	0.00	3%
90 th percentile	0.01	16%	0.02	8%	0.04	18%	0.04	21%	0.03	21%	0.02	6%	0.02	7%	0.02	11%	0.03	17%	0.00	0%	0.00	0%
Maximum	0.02	23%	0.03	18%	0.05	20%	0.05	39%	0.04	75%	0.03	15%	0.02	8%	0.03	17%	0.04	24%	0.01	17%	0.00	14%

^aThe values correspond to fits where it was ensured that NSSR of the best $n+1$ -component was at least 10% (relative) lower than the NSSR of the best n -component fit.

1 Table EA3. Precipitate P/Fe ratios, Fe K-edge EXAFS LCF results, LCF with endmember spectra, and corresponding P/Fe ratios for
2 precipitates formed in Na- and Ca electrolytes. All sample and reconstructed LCF spectra are shown in Fig. EA7, LCF results and
3 transformed fractions are shown in Figs. 4-6, Fig. 8 and Fig. EA9. Note that in Si-free solutions the endmember Fh-Si* is not needed.

	ICP-MS		LCF with reference spectra ^a							LCF with endmember spectra ^b					
Series	(P/Fe) _{init}	(P/Fe) _{ppt}	Mitr	FeP	HFO	Fh	Lp	Sum	NSSR (x1000)	FeP*	CaFeP*	HFO	pcLp*	Sum	NSSR (x1000)
Na	0.00	0.00	--	--	--	0.33	0.67	1.12	3.20	--	--	--	1.00	1.01	0.76
	0.04	0.03	--	--	0.26	0.20	0.54	1.10	2.83	--	--	0.21	0.79	1.02	1.07
	0.09	0.07	--	--	0.33	0.18	0.49	1.12	3.21	--	--	0.29	0.71	1.04	1.22
	0.18	<u>0.17</u>	--	0.16	0.51	--	0.32	1.07	1.87	<u>0.22</u>	--	<u>0.31</u>	<u>0.47</u>	1.02	0.74
	0.29	<u>0.28</u>	--	0.36	0.44	--	0.20	1.06	3.18	<u>0.41</u>	--	<u>0.30</u>	<u>0.29</u>	1.02	1.78
	0.39	<u>0.39</u>	--	0.60	0.33	--	0.07	1.03	2.51	<u>0.60</u>	--	<u>0.29</u>	<u>0.10</u>	1.01	0.87
	0.49	<u>0.47</u>	--	1.00	--	--	--	0.97	6.54	<u>1.00</u>	--	--	--	0.97	2.86
	0.59	<u>0.51</u>	--	1.00	--	--	--	0.98	5.46	<u>0.92</u>	--	<u>0.08</u>	--	0.99	1.32
	0.73	<u>0.55</u>	--	1.00	--	--	--	0.99	7.39	<u>1.00</u>	--	--	--	0.98	3.33
	0.97	0.58	--	1.00	--	--	--	1.01	7.67	1.00	--	--	--	1.00	3.82
	1.43	0.62	--	1.00	--	--	--	1.01	6.82	1.00	--	--	--	1.00	1.06
	1.95	0.68	--	1.00	--	--	--	1.01	4.59	1.00	--	--	--	1.00	0.96
Ca	0.00	0.00	--	--	--	0.30	0.70	1.13	4.00	--	--	--	1.00	1.05	1.27
	0.03	0.03	--	--	0.27	0.17	0.56	1.10	3.39	--	--	0.18	0.82	1.03	1.14
	0.08	0.08	--	--	0.27	0.19	0.54	1.13	3.13	--	--	0.21	0.79	1.05	1.41
	0.18	<u>0.17</u>	--	--	0.53	0.09	0.38	1.11	2.81	--	<u>0.15</u>	<u>0.26</u>	<u>0.58</u>	1.02	0.84
	0.30	<u>0.29</u>	--	0.37	--	0.29	0.35	1.07	2.43	--	<u>0.28</u>	<u>0.26</u>	<u>0.46</u>	1.03	2.52
	0.39	<u>0.39</u>	0.10	0.30	0.41	--	0.19	1.07	1.81	--	<u>0.40</u>	<u>0.31</u>	<u>0.30</u>	1.02	1.07
	0.50	<u>0.49</u>	0.11	0.49	0.24	--	0.16	1.04	3.39	--	<u>0.59</u>	<u>0.16</u>	<u>0.25</u>	1.00	1.98
	0.60	<u>0.60</u>	0.12	0.55	0.29	--	0.05	1.05	2.15	--	<u>0.62</u>	<u>0.29</u>	<u>0.09</u>	1.02	0.99
	0.73	<u>0.74</u>	0.13	0.87	--	--	--	1.02	6.43	--	<u>0.84</u>	<u>0.16</u>	--	1.02	3.80
	0.98	0.87	0.13	0.87	--	--	--	1.04	4.24	--	1.00	--	--	1.00	1.17
	1.45	1.00	0.16	0.84	--	--	--	1.03	5.38	--	1.00	--	--	1.00	1.62
	1.91	1.06	0.13	0.87	--	--	--	1.03	3.80	--	1.00	--	--	1.00	1.42

4 ^aDetails on LCF analysis in section 2.4.1. LCF-derived fractions normalized to a sum of 1 are listed together with the the effective sum of the
5 fitted fractions. NSSR: normalized sum of squared residuals ($NSSR = \sum(\text{data}_i - \text{fit}_i)^2 / \sum(\text{data}_i)^2$). ^bDerivation of FeP*, CaFeP*, HFO and
6 pcLp* described in sections 3.2.2 and 3.2.3 in the main manuscript. Fit uncertainties are listed in Table EA2.

1 Table EA4. Precipitate P/Fe ratios, Fe K-edge EXAFS LCF results, LCF with endmember spectra, and corresponding P/Fe ratios for
2 precipitates formed in Mg and low Ca electrolytes. All sample and reconstructed LCF spectra are shown in Fig. EA7, LCF results and
3 transformed fractions are shown in Figs. 4-6, Fig. 8 and Fig. EA9.

Series	ICP-MS		LCF with reference spectra ^a							LCF with endmember spectra ^b					
	(P/Fe) _{ini} t	(P/Fe) _{pp} t	Mitr	FeP	HFO	Fh	Lp	Sum	NSSR (x1000)	FeP*	lowCaFeP*	HFO	pcLp*	Sum	NSSR (x1000)
Mg	0.00	0.00	--	--	0.15	0.22	0.63	1.10	3.32	--	--	0.06	0.94	1.01	0.84
	0.05	0.05	--	--	0.46	--	0.54	1.07	3.45	--	--	0.23	0.77	1.01	2.11
	0.10	0.09	--	--	0.40	0.16	0.45	1.09	2.95	--	--	0.36	0.64	1.03	2.38
	0.19	<u>0.19</u>	--	0.20	0.45	--	0.35	1.04	3.69	<u>0.26</u>	--	<u>0.23</u>	<u>0.51</u>	0.99	2.61
	0.30	<u>0.29</u>	--	0.31	0.40	0.11	0.18	1.04	2.38	<u>0.29</u>	--	<u>0.45</u>	<u>0.25</u>	1.01	1.85
	0.41	<u>0.41</u>	--	0.39	0.49	--	0.12	1.04	2.06	<u>0.40</u>	--	<u>0.43</u>	<u>0.17</u>	1.02	1.45
	0.51	<u>0.51</u>	--	0.74	0.26	--	--	0.99	5.46	<u>0.71</u>	--	<u>0.29</u>	--	0.99	3.45
	0.63	<u>0.62</u>	--	1.00	--	--	--	0.95	6.20	<u>0.85</u>	--	<u>0.15</u>	--	0.98	2.80
	0.73	<u>0.62</u>	--	1.00	--	--	--	0.96	5.75	<u>0.89</u>	--	<u>0.11</u>	--	0.97	2.17
	1.00	0.70	--	1.00	--	--	--	0.96	5.27	0.89	--	0.11	--	0.98	1.84
	1.46	0.73	--	1.00	--	--	--	0.96	5.63	1.00	--	--	--	0.96	2.44
	1.87	0.69	--	1.00	--	--	--	0.96	6.57	1.00	--	--	--	0.95	2.89
low Ca	0.00	0.00	--	--	0.17	0.16	0.68	1.07	3.31	--	--	--	1.00	0.98	1.08
	0.05	0.05	--	--	0.30	0.14	0.56	1.09	2.78	--	--	0.18	0.82	1.02	1.73
	0.10	0.09	--	--	0.51	--	0.49	1.09	2.99	--	0.13	0.13	0.74	1.01	1.73
	0.20	<u>0.19</u>	--	0.15	0.48	--	0.37	1.07	4.15	--	<u>0.24</u>	<u>0.21</u>	<u>0.55</u>	1.01	2.89
	0.30	<u>0.29</u>	--	0.27	0.48	--	0.25	1.03	2.69	--	<u>0.35</u>	<u>0.28</u>	<u>0.37</u>	0.99	1.58
	0.43	<u>0.42</u>	--	0.46	0.37	--	0.17	1.03	3.85	--	<u>0.56</u>	<u>0.18</u>	<u>0.26</u>	1.00	2.46
	0.54	<u>0.54</u>	--	0.61	0.34	--	0.04	1.00	3.75	--	<u>0.70</u>	<u>0.22</u>	<u>0.08</u>	0.99	1.77
	0.64	<u>0.63</u>	--	0.90	0.10	--	--	0.97	4.59	--	<u>1.00</u>	--	--	0.97	1.84
	0.71	<u>0.62</u>	--	1.00	--	--	--	0.97	7.04	--	<u>1.00</u>	--	--	0.99	4.18
	1.02	0.73	--	1.00	--	--	--	0.98	4.08	--	1.00	--	--	0.99	0.87
	1.45	0.73	--	1.00	--	--	--	0.98	4.22	--	1.00	--	--	1.00	0.38
	2.00	0.80	0.05	0.95	--	--	--	1.00	3.79	--	1.00	--	--	1.00	0.52

4 ^aSee footnote of Table EA3. ^bDerivation of FeP*, lowCaFeP*, HFO and pcLp* described in sections 3.2.2 and 3.2.3 in the main manuscript.

5

1 Table EA5. Precipitate P/Fe ratios, Fe K-edge EXAFS LCF results, LCF with endmember spectra, and corresponding P/Fe ratios for
2 precipitates formed in Na+Si and Ca+Si electrolytes. All sample and reconstructed LCF spectra are shown in Fig. EA7, LCF results and
3 transformed fractions are shown in Figs. 4-6, Fig. 8 and Fig. EA9.

Series	ICP-MS		LCF with reference spectra ^a							LCF with endmember spectra ^b				
	(P/Fe) _{init}	(P/Fe) _{ppt}	Mitr	FeP	HFO	Fh	Lp	Sum	NSSR (x1000)	FeP*	CaFeP*	Fh-Si*	Sum	NSSR (x1000)
Na+Si	0.00	0.00	--	0.33	--	0.67	--	1.03	9.13	--	--	1.00	0.99	1.65
	0.04	0.04	--	0.23	0.34	0.43	--	1.04	3.61	--	--	1.00	1.00	4.87
	0.08	0.08	--	0.32	0.31	0.37	--	1.03	4.46	0.17	--	0.83	0.99	3.74
	0.18	<u>0.18</u>	--	0.47	0.24	0.30	--	1.01	4.52	<u>0.32</u>	--	<u>0.68</u>	0.98	2.61
	0.31	<u>0.31</u>	--	0.61	0.28	0.12	--	1.01	4.81	<u>0.56</u>	--	<u>0.44</u>	0.99	2.54
	0.38	<u>0.38</u>	--	0.76	0.24	--	--	0.98	4.22	<u>0.74</u>	--	<u>0.26</u>	0.98	1.56
	0.48	<u>0.46</u>	--	1.00	--	--	--	0.98	7.59	<u>1.00</u>	--	--	0.97	2.70
	0.57	<u>0.51</u>	--	1.00	--	--	--	0.98	5.08	<u>0.91</u>	--	<u>0.09</u>	0.99	1.41
	0.75	<u>0.57</u>	--	1.00	--	--	--	1.00	7.32	<u>1.00</u>	--	--	0.99	3.88
	0.94	0.57	--	1.00	--	--	--	1.00	5.17	1.00	--	--	1.00	1.22
	1.39	0.61	--	1.00	--	--	--	1.00	4.56	1.00	--	--	0.99	0.76
	1.84	0.63	--	1.00	--	--	--	1.01	4.57	1.00	--	--	1.00	1.20
Ca+Si	0.00	0.00	--	0.28	0.23	0.49	--	1.05	5.54	--	--	1.00	1.01	1.76
	0.04	0.04	--	0.29	0.26	0.45	--	1.03	4.55	--	0.10	0.90	0.98	2.66
	0.09	0.09	--	0.24	0.38	0.38	--	1.05	3.48	--	0.13	0.87	0.99	3.63
	0.19	<u>0.19</u>	--	0.40	0.21	0.39	--	1.03	3.62	--	<u>0.25</u>	<u>0.75</u>	0.98	1.94
	0.31	<u>0.31</u>	--	0.58	--	0.42	--	1.03	5.40	--	<u>0.38</u>	<u>0.62</u>	1.00	3.93
	0.41	<u>0.41</u>	--	0.65	--	0.35	--	1.01	3.94	--	<u>0.52</u>	<u>0.48</u>	0.98	2.89
	0.50	<u>0.50</u>	--	0.76	--	0.24	--	1.01	6.12	--	<u>0.73</u>	<u>0.27</u>	0.97	2.98
	0.60	<u>0.60</u>	--	0.75	--	0.25	--	1.02	3.14	--	<u>0.67</u>	<u>0.33</u>	0.99	1.45
	0.76	<u>0.76</u>	0.09	0.91	--	--	--	1.01	8.77	--	<u>0.88</u>	<u>0.12</u>	1.00	5.01
	1.00	0.90	0.12	0.88	--	--	--	1.03	4.45	--	1.00	--	1.00	1.67
	1.50	1.05	0.15	0.85	--	--	--	1.03	5.50	--	1.00	--	1.00	1.54
	1.98	1.13	0.12	0.88	--	--	--	1.03	4.04	--	1.00	--	1.00	1.22

^aSee footnote of Table EA3. ^bDerivation of FeP*, CaFeP* and Fh-Si* see sections 3.2.2 and 3.2.3 in the main manuscript.

EA5. Molar P/Fe, Ca/Fe and Mg/Fe ratios of Fe(III)-phosphates

TableEA6. Measured and calculated molar P/Fe, Ca/Fe and Mg/Fe ratios of precipitates formed in Mg, low Ca, Ca and Ca+Si electrolytes at (P/Fe)_{init} ~0.75, ~1, ~1.5 and ~2.

Electrolyte	(P/Fe) _{init}	(P/Fe) _{ppt} ^a	(Mg/Fe) _{ppt}	(Ca/Fe) _{ppt}	Comment ^b	LR ^c	Figures using data
Mg	1.00	<u>0.70</u>	na ^d	--	S		Figs. 2, 3a, EA3, EA4, EA11
	1.04	0.67	0.22	--	D	x	Figs 3b
	1.46	<u>0.73</u>	na ^d	--	S		Figs. 2, 3a, EA3, EA4, EA11
	1.58	0.74	0.26	--	D	x	Figs 3b
	1.87	<u>0.69</u>	na ^d	--	S		Figs. 2, 3a, EA3, EA4, EA11
	2.09	0.77	0.27	--	D	x	Figs 3b
low Ca	1.02	<u>0.73</u>	--	0.36	S	x	Figs. 2, 3a, EA3, EA4, EA11
	1.03	0.73	--	0.33	S		Figs 3b
	1.45	<u>0.73</u>	--	0.37	S	x	Figs. 2, 3a, EA3, EA4, EA11
	1.54	0.79	--	0.35	S		Figs 3b
	2.00	<u>0.80</u>	--	0.37	S	x	Figs. 2, 3a, EA3, EA4, EA11
	2.04	0.82	--	0.33	S		Figs 3b
Ca	0.73	0.74	--	0.49	S		Figs. 2, 3ab, EA3, EA4, EA11
	0.78	0.78	--	0.33	S		Fig. 3b
	0.98	<u>0.87</u>	--	0.55	S	x	Figs. 2, 3ab, EA3, EA4, EA11
	1.07	0.88	--	0.54	D		Fig. 3b
	1.45	<u>1.00</u>	--	0.60	S	x	Figs. 2, 3ab, EA3, EA4, EA11
	1.47	1.03	--	0.77	S		Fig. 3b
	1.46	1.03	--	0.72	S		Fig. 3b
	1.47	1.00	--	0.65	S		Fig. 3b
	1.66	1.03	--	0.66	D		Fig. 3b
	1.91	<u>1.06</u>	--	0.72	S	x	Figs. 2, 3ab, EA3, EA4, EA11
Ca+Si	2.15	1.12	--	0.75	D		Fig. 3b
	0.76	0.76	--	0.41	S		Figs. 2, 3ab, EA3, EA4, EA11
	1.00	<u>0.90</u>	--	0.54	S	x	
	1.50	<u>1.05</u>	--	0.61	S	x	
	1.98	<u>1.13</u>	--	1.09	S	x	

^aData used for linear regression of (P/Fe)_{ppt} versus (P/Fe)_{init} is underlined. ^bD: Molar (P/Fe)_{ppt} and ((Mg,Ca/Fe)_{ppt} were obtained from precipitate digestion. S: (P/Fe)_{ppt} and (Ca/Fe)_{ppt} were calculated from solution data (total initial and final filtered solutions). ^cx: Data on

$((\text{Ca,Mg})/\text{Fe})_{\text{ppt}}$ was used for linear regression of $((\text{Ca,Mg})/\text{Fe})_{\text{ppt}}$ versus $(\text{P/Fe})_{\text{init.}}^{\text{d}}$ na; not analyzed.

EA6. Principal component analysis (PCA)

PCA of the spectra of all samples (n=72)

For principal component analysis, software from beamline 10.3.2 of the Advanced light source was used (Marcus et al., 2004). The k^3 -weighted Fe K-edge EXAFS spectra of all 72 samples were analyzed over the k -range 2-11 \AA^{-1} . Based on visual examination, the first 4 components were considered to represent spectral features. These 4 components allowed to reproduce the 5 reference spectra used for LCF analysis of the sample spectra.

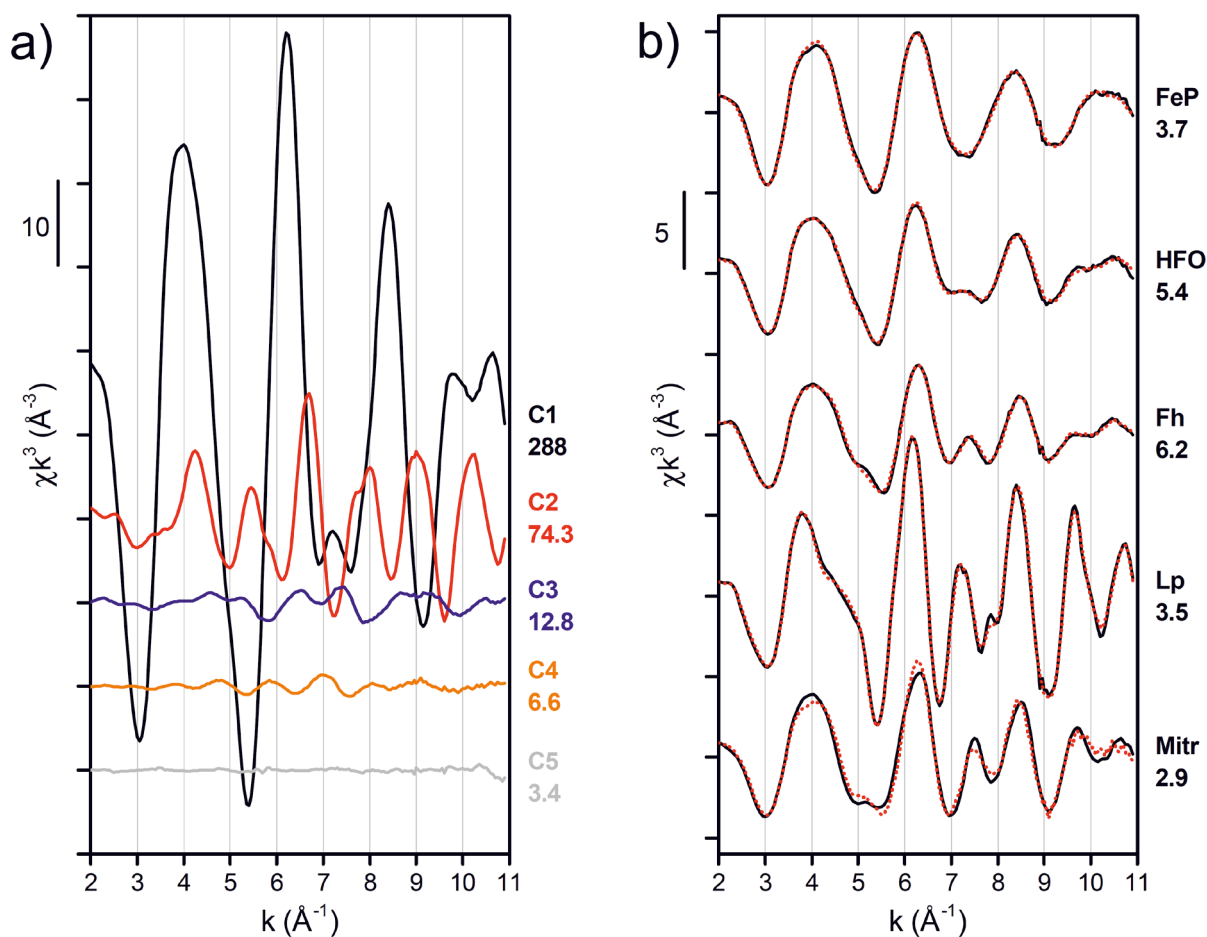


Fig. EA5. (a) First 5 components from PCA of all 72 Fe K-edge EXAFS sample spectra over k -range 2-11 \AA^{-1} (numbers below component labels indicate Eigenvalue). (b) Target transforms (red dotted lines) of reference spectra (black solid lines) used for LCF analysis based on the first 4 components from PCA (numbers below reference labels indicate NCSR \times 1000 of the target transform).

PCA of the spectra of samples formed at $(P/Fe)_{init}$ of ~ 1 and higher ($n=18$)

Evaluation of the k^3 -weighted Fe K-edge EXAFS spectra of the 18 spectra of samples formed at $(P/Fe)_{init}$ of ~ 1 and higher by PCA indicated that they contained two spectral components. Using the first two components, the reference spectrum FeP could be perfectly reproduced, and also the mitridatite reference spectrum could be reproduced well with respect to both the first and second shell, supporting the use of the mitridatite reference spectrum in combination with the FeP spectrum to describe spectral (and structural) differences between Fe(III)-phosphate precipitates formed in the absence and presence of Ca.

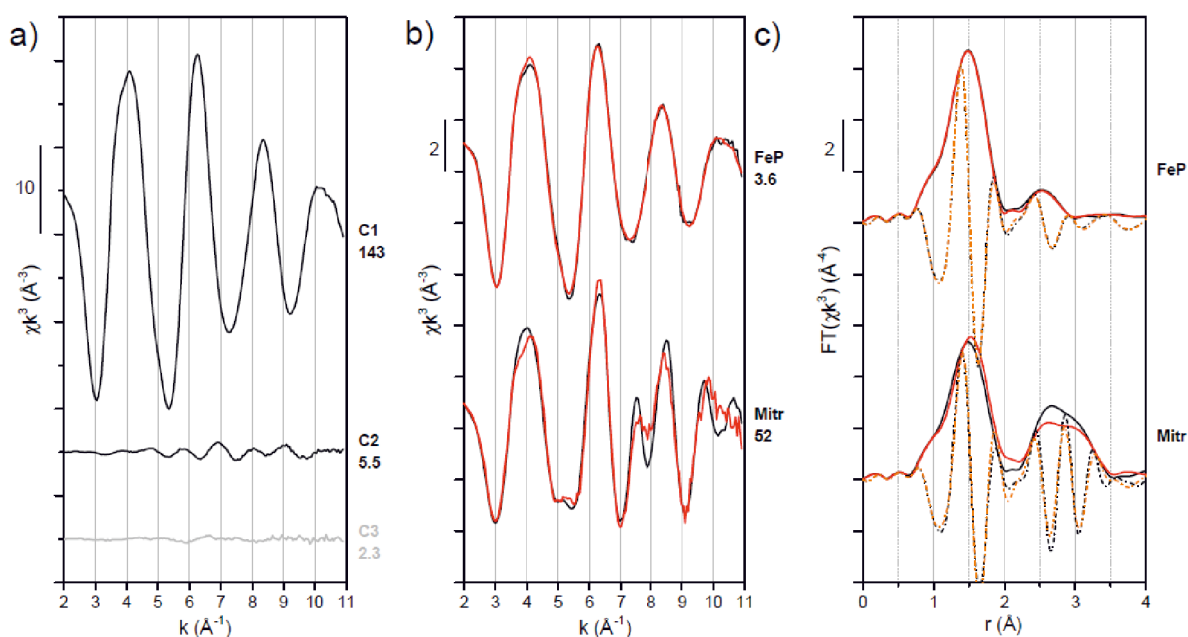


Fig. EA6. (a) First 3 components from PCA of the Fe K-edge EXAFS spectra of the 18 samples formed at $(P/Fe)_{init}$ of ~ 1 , ~ 1.5 and ~ 2 (numbers below component labels indicate Eigenvalue). (b) Target transforms (red dotted lines) of reference spectra FeP and Mitr (black solid lines) based on the first two components (numbers indicate $NSSR \times 1000$ of the target transform). (c) Fourier-transformed reference and target transform spectra (magnitudes as black and red solid lines; imaginary parts as black and orange dash-dotted lines, respectively).

EA7. Fe K-edge EXAFS sample spectra and reconstructed spectra based on LCF with reference spectra

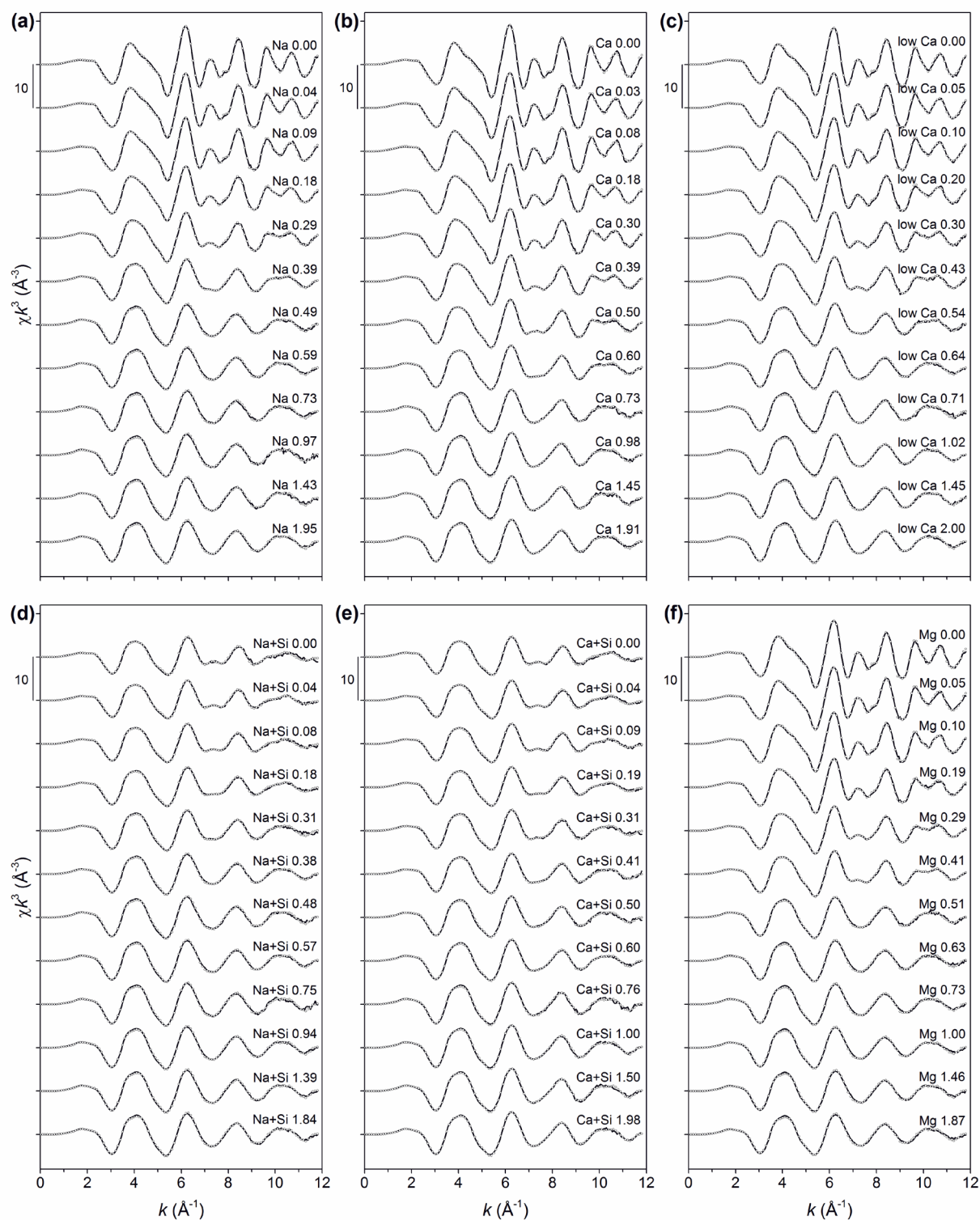


Fig. EA7. (a-f) Fe K-edge EXAFS spectra (solid lines) and reconstructed LCF spectra (open circles) of Fe(III)-precipitates formed in Na, Ca, low Ca, Mg, Na+Si, and Ca+Si electrolytes. Numbers at the right of the spectra indicate the background electrolyte and the molar initial dissolved P/Fe ratio ($(\text{P/Fe})_{\text{init}}$). Sample details and LCF results are listed in Tables EA3-5.

EA8. Comparison of sample spectra averaged to obtain endmember spectra

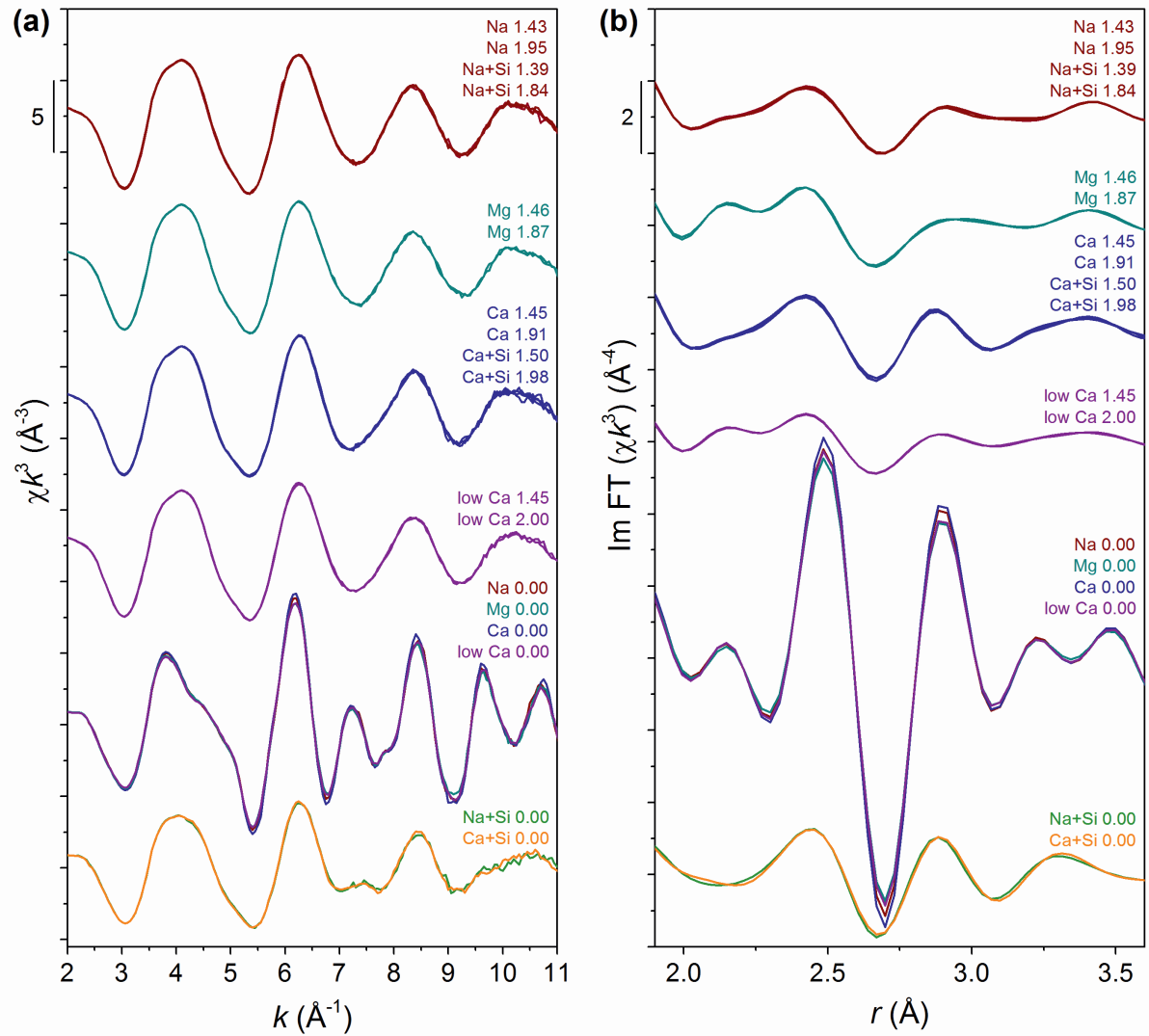
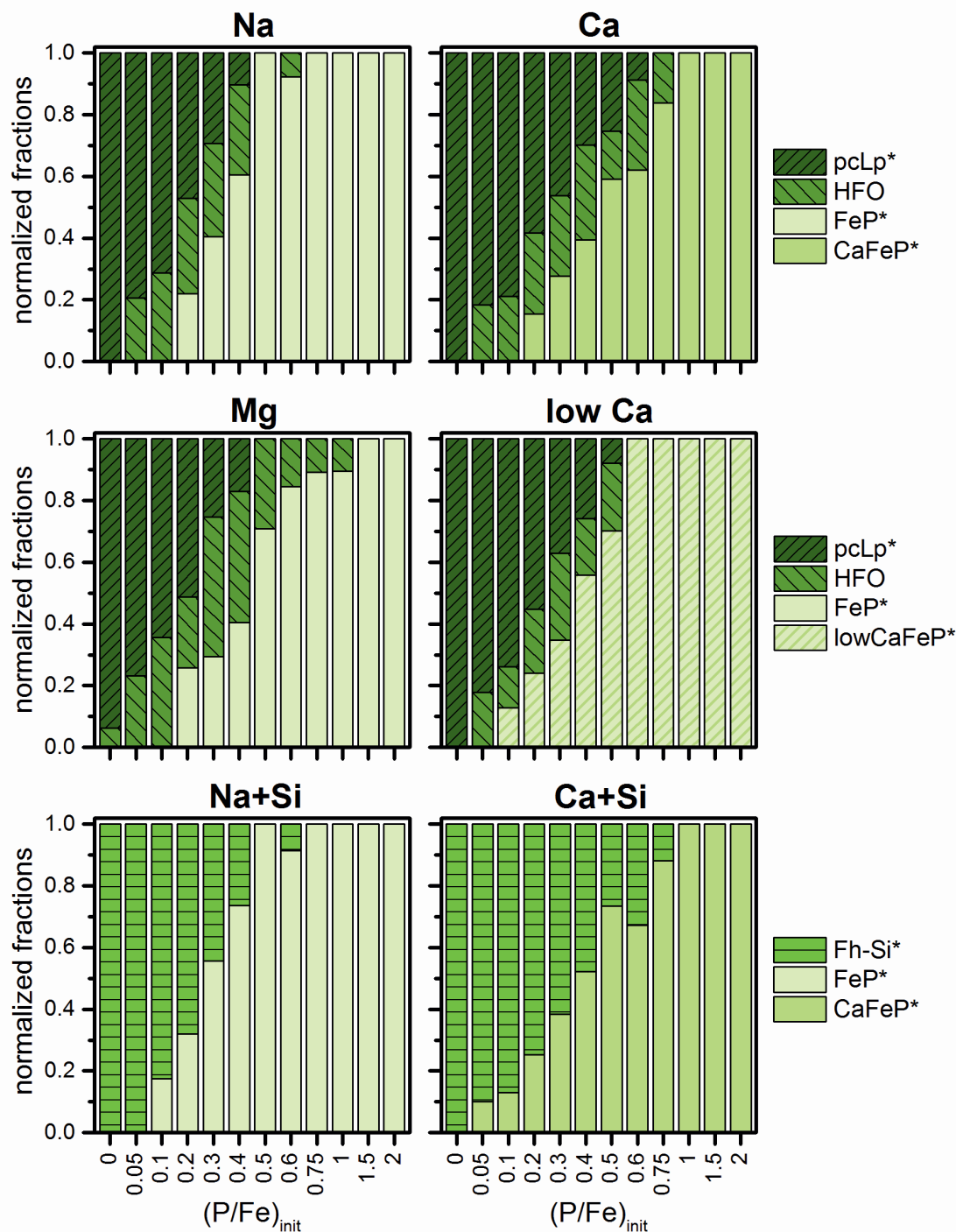


Fig. EA8. Comparison of Fe K-edge EXAFS spectra of precipitates formed at $(\text{P/Fe})_{\text{init}}$ of ~ 1.5 and ~ 2 in the Na and Na+Si electrolytes, Mg electrolyte, Ca and Ca+Si electrolytes, and low Ca electrolyte as well as of the spectra formed at $(\text{P/Fe})_{\text{init}}$ of 0.00 in absence (Na, Mg, Ca, and low Ca electrolytes) and presence of silicate (Na+Si and Ca+Si) electrolytes. (a) Spectra in k -space. (b) Imaginary parts of Fourier-transformed spectra in r -space. The grouped spectra exhibited a very high similarity and were averaged to obtain (from top) the spectra FeP*, MgFeP*, CaFeP*, lowCaFeP*, pcLp* and Fh-Si* (shown in Fig. 5ab).

EA9. Results of LCF analysis of Fe K-edge EXAFS spectra with endmember spectra



EA10. Comparison of Fe2-sGW with CaFeP*

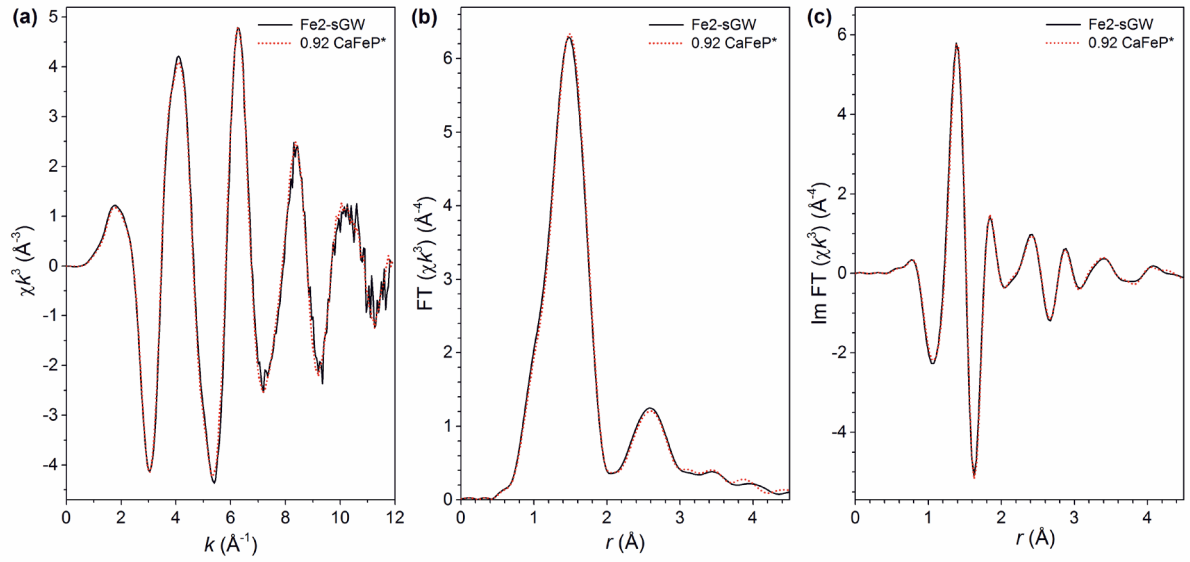


Fig. EA10. (a) Fe K-edge EXAFS spectra and corresponding Fourier-transformed spectra ((b) magnitude; (c) imaginary part) of precipitate Fe2-sGW from Kaegi et al. (2010) and Voegelin et al. (2010) in comparison to one component fit with 0.92 CaFeP*.

EA11. Molar P/Fe ratios of Fe(III)-phosphate- and ferrihydrite-type precipitate fractions

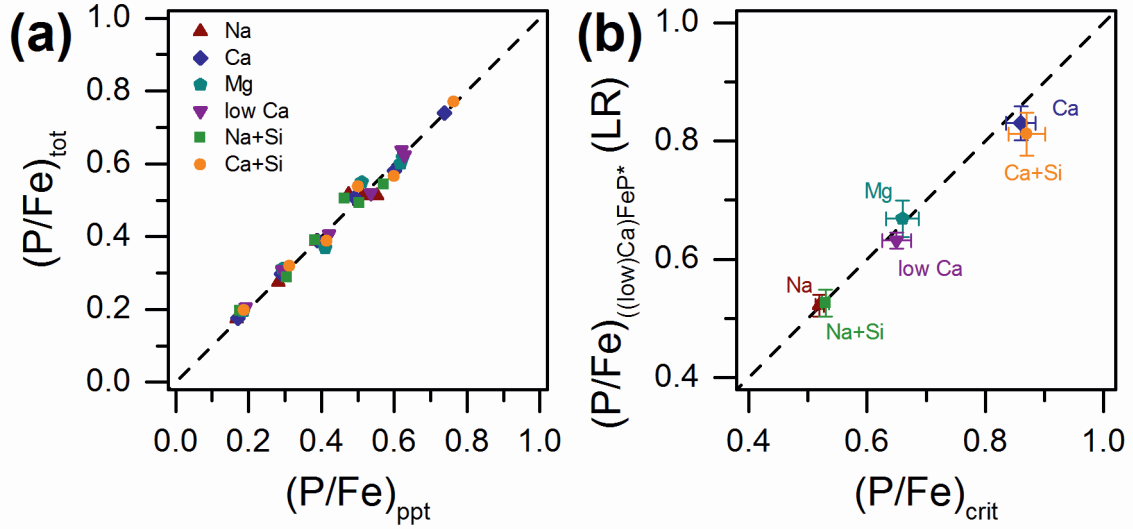


Fig. EA11. (a) Comparison of the $(P/Fe)_{ppt}$ measured by ICP-MS with the $(P/Fe)_{tot}$ calculated from the $(P/Fe)_{FeP^*/CaFeP^*/lowCaFeP^*}$ and $(P/Fe)_{HFO/Fh-Si^*}$ derived from multiple linear regression. (b) Comparison of the $(P/Fe)_{crit}$ ratios of individual electrolytes with the respective $(P/Fe)_{FeP^*}$, $(P/Fe)_{CaFeP^*}$ or $(P/Fe)_{lowCaFeP^*}$ ratios obtained by linear regression of $(P/Fe)_{ppt}$ over the fractions FeP^* , $CaFeP^*$ or $lowCaFeP^*$ and HFO or Fh-Si* (see text below).

Data used for multiple linear regression ($(P/Fe)_{ppt}$ ratios, FeP^* -/ $CaFeP^*$ -/ $lowCaFeP^*$ - and HFO-/Fh-Si*-fractions derived from LCF analysis) are underlined in Tables EA3-5. Only data from samples formed at intermediate $(P/Fe)_{init}$ (0.2-0.75) was used. Below $(P/Fe)_{init}$ of 0.2, the ferrihydrite-type precipitate fraction may not be saturated with phosphate, and above $(P/Fe)_{init}$ of 0.75, FeP^* -/ $CaFeP^*$ -/ $lowCaFeP^*$ is the only fraction obtained by LCF. The following regression equations were used to derive $(P/Fe)_{((low)Ca)FeP^*}$ and $(P/Fe)_{HFO^*/Fh-Si^*}$ in the silicate-free and silicate-containing electrolytes:

Silicate-free electrolytes (Na, Ca, Mg, low Ca):

$$(P/Fe)_{ppt} = [(P/Fe)_{((low)Ca)FeP^*} \times ((low)Ca)FeP^*] + [(P/Fe)_{HFO} \times HFO] + [(P/Fe)_{pcLp^*} \times pcLp^*] \quad \text{Eq. EA1}$$

Silicate-containing electrolytes (Na+Si, Ca+Si):

$$(P/Fe)_{ppt} = [(P/Fe)_{(Ca)FeP^*} \times (Ca)FeP^*] + [(P/Fe)_{Fh-Si^*} \times Fh-Si^*] \quad \text{Eq. EA2}$$

The coefficients of determination (R^2) of all multiple linear regressions were ≥ 0.99 (Na: 0.996; Ca: 0.999; Mg: 0.997; low Ca: 0.999; Na+Si: 0.994; Ca+Si: 0.990).

EA12. Ca K-edge XANES and EXAFS spectra and LCF analyses

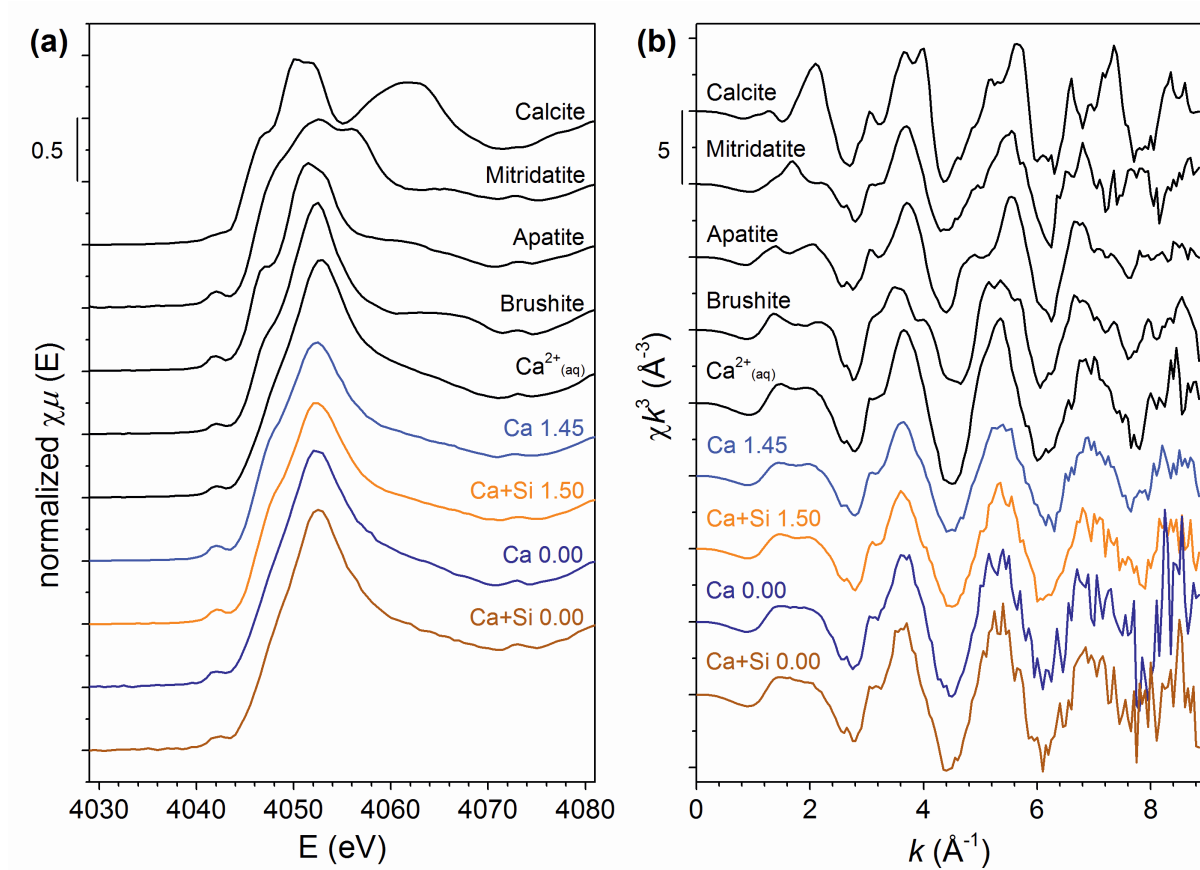


Fig. EA12. Ca K-edge XANES and EXAFS spectra of reference materials and samples.

EA13. FTIR analyses

The FTIR spectra of samples and references are shown in Fig. EA13. The precipitate formed at a $(P/Fe)_{init} \sim 0.05$ in the absence of Si (panel a) exhibit bands at 1018, 744 and 742 cm^{-1} that are characteristic for lepidocrocite (L) with platy morphology (Cornell and Schwertmann, 2003). No lepidocrocite bands were observed at $(P/Fe)_{init}$ of ~ 0.75 and ~ 1.50 . The marked broad band around 986 cm^{-1} in these spectra reflects the high phosphate content of the precipitates. In the Ca background electrolyte as compared to the Na electrolyte, this band was slightly broader at lower wavenumbers and exhibited a shoulder at higher wavenumbers. In addition, a band at 546 cm^{-1} was observed for the precipitate formed in the Ca electrolyte at the highest $(P/Fe)_{init}$ of ~ 1.5 and to a minor extent at $(P/Fe)_{init}$ of ~ 0.75 , which is absent in the corresponding spectra of precipitates formed in Na electrolyte. Comparison with the spectra of Ca-phosphate reference phases showed that these spectral differences most closely match to the spectrum of β -TCP, suggesting that they arise from vibrations of Ca-coordinated phosphate groups. On the other hand, the fact that the additional features were rather broad indicated that Ca did not induce the formation of a well-crystallized Ca-(Fe(III))-phosphate precipitate, in line with XRD results. Precipitates formed at $(P/Fe)_{init} \sim 0.05$ in the presence of Si (panel b) did not exhibit any lepidocrocite bands, but exhibited a band at 925 cm^{-1} arising from sorbed silicate. At the higher $(P/Fe)_{init}$ of 0.75 and 1.5, the band arising from silicate was absent, and the phosphate-related bands exhibited the same dependence on the presence/absence of Ca as in the Si-free background electrolytes. Bands at 1490, 1475 and 1382 cm^{-1} at low $(P/Fe)_{init}$ originate from adsorbed carbonate (C). The extent of carbonate sorption was promoted by silicate and to a lesser extent Ca in the electrolytes. The band at 1648 cm^{-1} was attributed to surface bound or structural water (W).

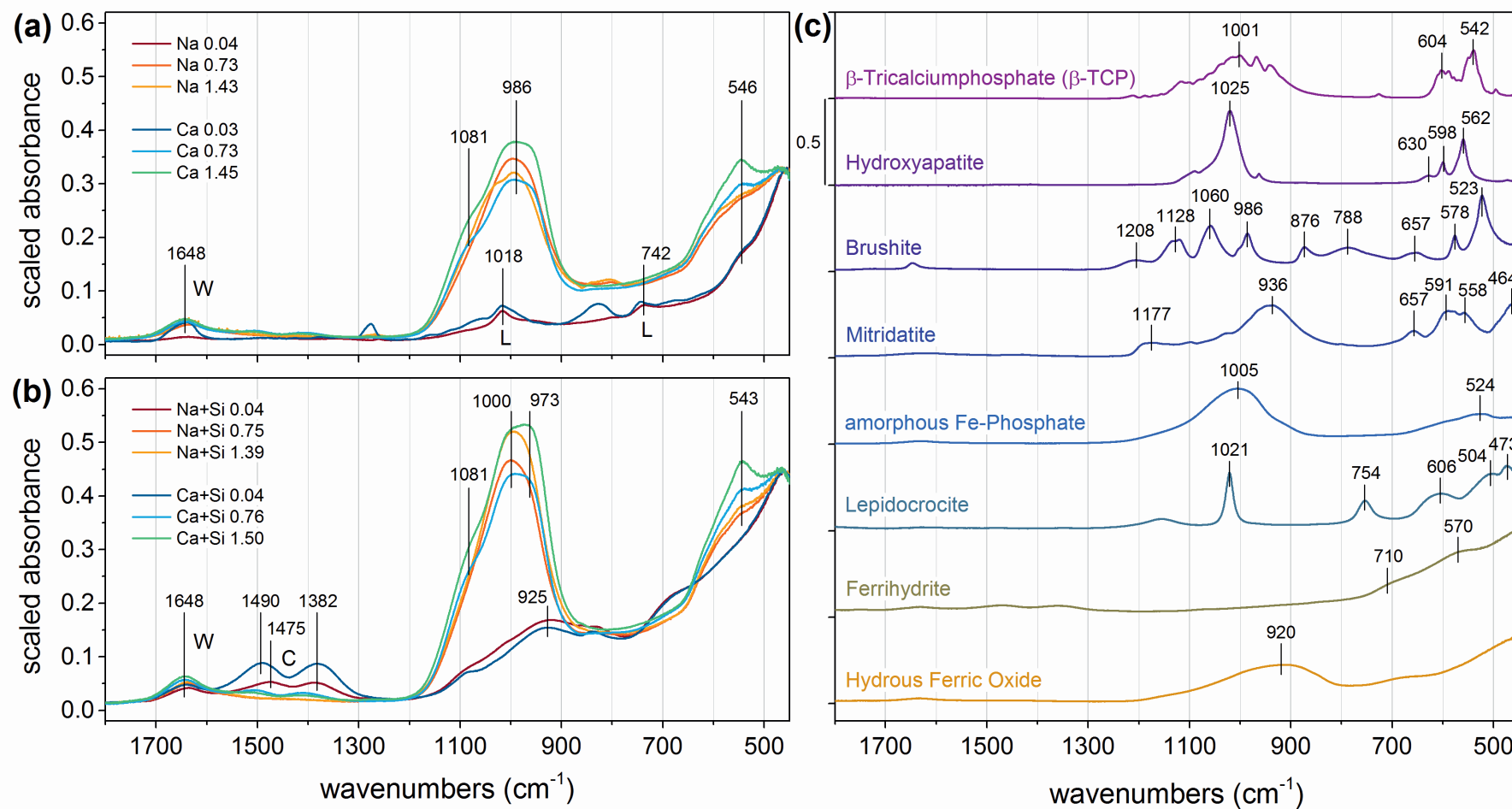


Fig. EA13. (a,b) Fourier-transform infrared spectra of selected precipitates formed in Na, Ca, Na+Si and Ca+Si electrolyte at $(\text{P/Fe})_{\text{init}}$ of ~ 0.05 , ~ 0.75 and ~ 1.5 . The spectra were scaled to the average absorbance of all spectra in the wavenumbers range $455\text{--}465\text{ cm}^{-1}$. (c) Spectra of selected references were offset by 0.5 absorbance units for clarity. Differences in the lepidocrocite peak positions are explained by the different morphologies (rod-shaped lepidocrocite reference, spherical aggregates of plate-shaped and poorly crystalline lepidocrocite in the precipitates).

EA14. Estimated Ca and phosphate fractions in Ca-Fe(III)-phosphate formed at (P/Fe)_{init} of 1.5 in Ca and Ca+Si electrolytes

Table EA7. Estimation of the fractions of Ca and phosphate associated with mitridatite-like Fe (mitr-like Fe), FeP-like Fe and remaining Ca and phosphate fractions tentatively attributed to Ca-phosphate precipitation (CaP) in Ca-Fe(III)-phosphate formed at (P/Fe)_{init} of 1.5 in Ca and Ca+Si electrolytes. The "low" estimate was based on the LCF-derived mitridatite fraction (with assumed Ca/Fe and P/Fe as in crystalline mitridatite) and the assumption that the (Ca/Fe) and (P/Fe) of the FeP-like Fe fraction corresponded to the (Mg/Fe)_{1.5} and (P/Fe)_{1.5} of the Fe(III)-phosphate formed in Mg electrolyte (Table 2). The "high" estimate was based on the assumption that the fraction of Fe in mitridatite-like Ca-Fe(III)-phosphate polymers corresponded to twice the LCF-derived mitridatite fraction (with assumed Ca/Fe and P/Fe as in crystalline mitridatite) and that the (Ca/Fe) and (P/Fe) of the FeP-like Fe fraction corresponded to the (Ca/Fe)_{1.5} and (P/Fe)_{1.5} of the Ca-Fe(III)-phosphate formed in low Ca electrolyte (Table 2). Further details in section 4.1.2.

	Fraction	% Fe _{tot}	(Ca/Fe)	(P/Fe)	(Ca/Fe) _{tot}	% Ca _{tot}	(P/Fe) _{tot}	% P _{tot}	(Ca/P) ^b
low	Total^a				<i>0.70</i>		<i>1.01</i>		
	mitr-like Fe	15%	0.67	1.00	0.10	14%	0.15	15%	
	FeP-like Fe	85%	0.25	0.71	0.21	30%	0.60	60%	
	CaP				0.39	55%	0.26	25%	1.51
high	Total				<i>0.70</i>		<i>1.01</i>		
	mitr-like Fe	30%	0.67	1.00	0.20	29%	0.30	30%	
	FeP-like Fe	70%	0.37	0.76	0.26	37%	0.53	53%	
	CaP				0.24	34%	0.18	18%	1.35

^aTotals correspond to average of (Ca/Fe)_{1.5} and (P/Fe)_{1.5} of the Ca and Ca+Si electrolytes (Table 2).

^bMolar (Ca/P) ratio of remaining Ca and phosphate (CaP fraction).

EA15. Transmission electron microscopy

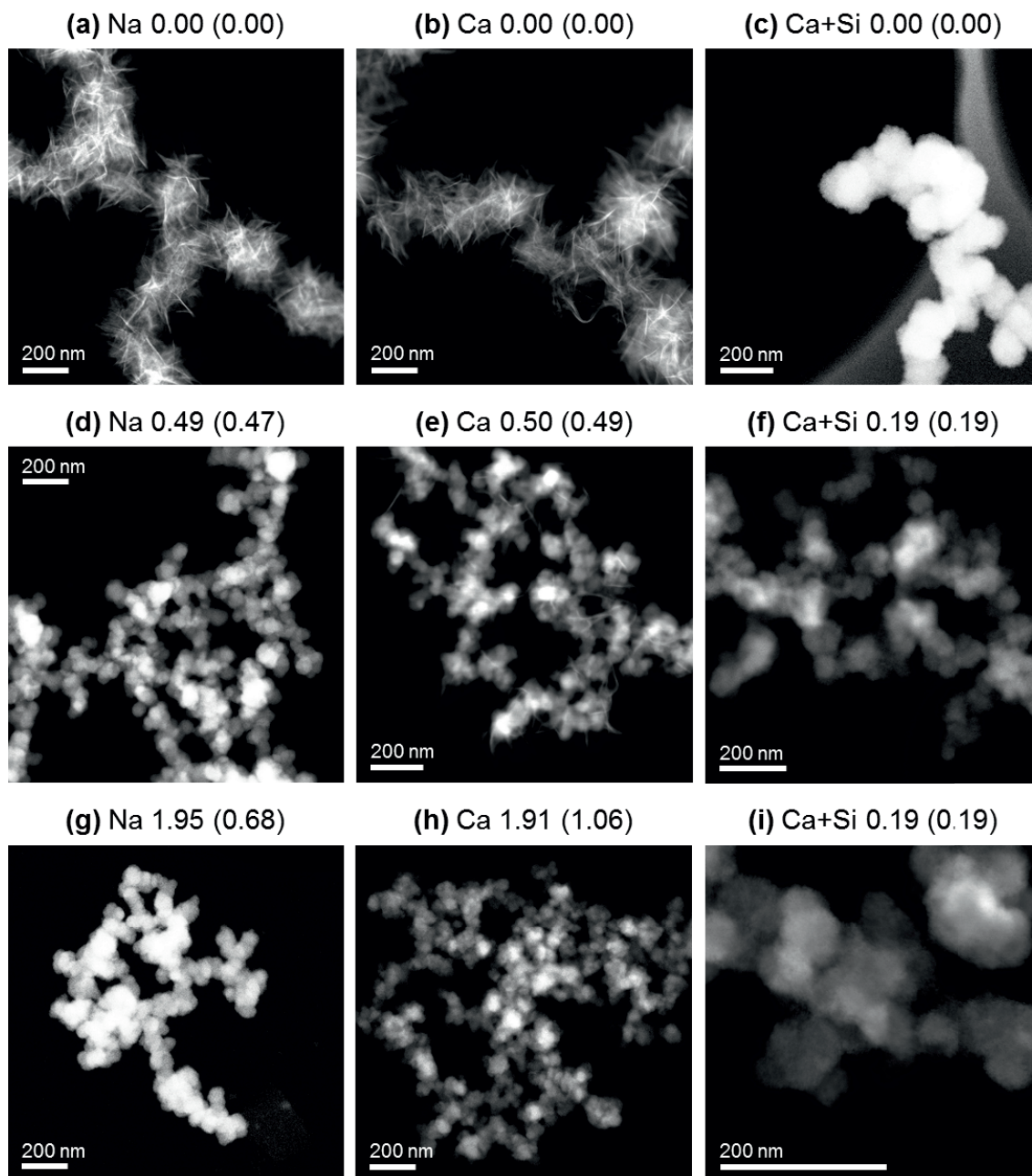


Fig. EA14. High-angle annular dark field (HAADF) STEM images indicating the mass-thickness contrast of selected Fe(III)-precipitates formed in (a,d,g) Na-, (b,e,h) Ca- and (c,f,i) Ca+Si-electrolyte at different $(P/Fe)_{init}$ ($(P/Fe)_{ppt}$ in parentheses). The corresponding secondary electron (SE) images are shown in Fig. 12.

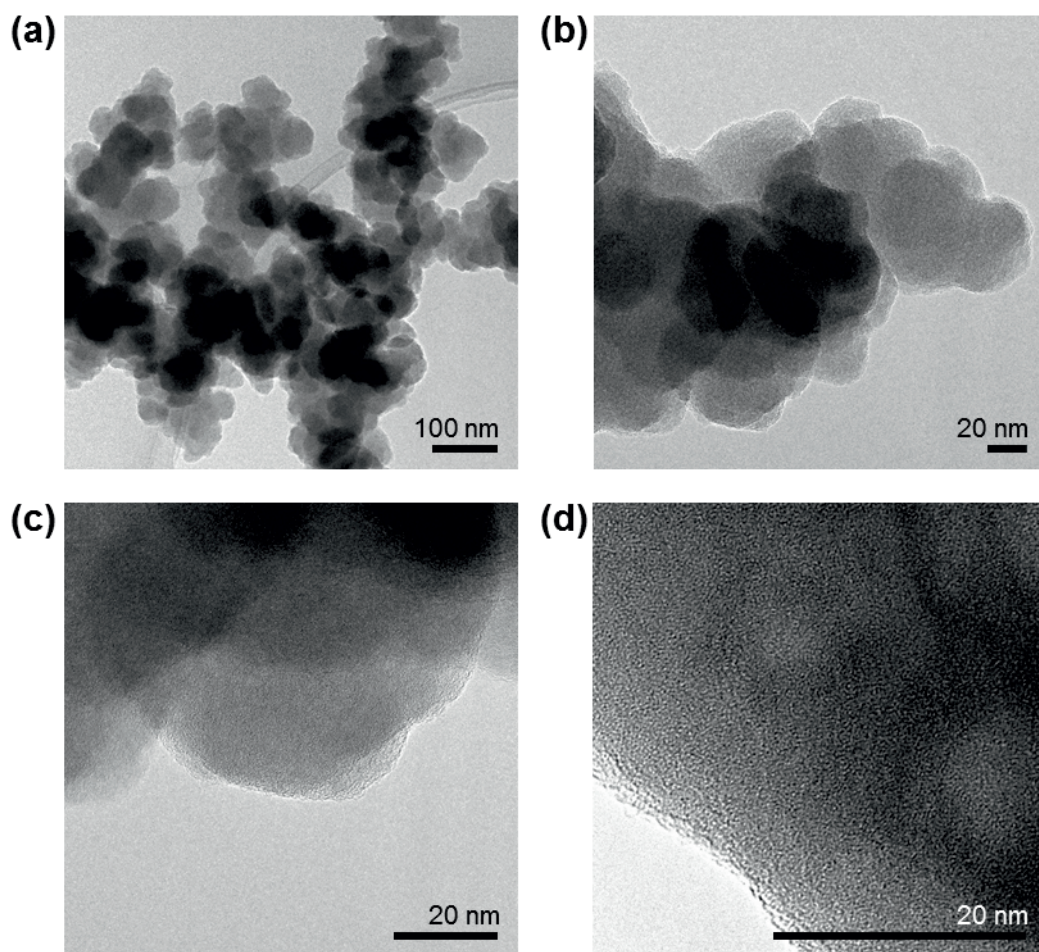


Fig. EA15. (a-d) Bright field TEM images of sample Ca 1.47 (formed in Ca electrolyte at $(\text{P/Fe})_{\text{init}} 1.47$) with increasing magnifications.

EA16. References

- Ankudinov, A.L., Ravel, B., Rehr, J.J., Conradson, S.D. (1998). Real-space multiple-scattering calculation and interpretation of x-ray absorption near-edge structure. *Physical Review B* **58**, 7565-7576.
- Cornell, R.M., Schwertmann, U. (2003) *The Iron Oxides: Structure, Properties, Reactions, Occurrences and Uses*. Wiley-VCH, Weinheim.
- Kaegi, R., Voegelin, A., Folini, D., Hug, S.J. (2010). Effect of phosphate, silicate, and Ca on the morphology, structure and elemental composition of Fe(III)-precipitates formed in aerated Fe(II) and As(III) containing water. *Geochim. Cosmochim. Acta* **74**, 5798-5816.
- Marcus, M.A., Macdowell, A.A., Celestre, R.S., Manceau, A., Miller, T., Padmore, H.A., Sublett, R.E. (2004). Beamline 10.3.2 at ALS: a hard X-ray microprobe for environmental and materials sciences. *J. Synchrotron Rad.* **11**, 239-247.
- Momma, K., Izumi, F. (2011). VESTA 3 for three-dimensional visualization of crystal, volumetric and morphology data. *Journal of Applied Crystallography* **44**, 1272-1276.
- Moore, P.B., Araki, T. (1977). Mitridatite, $\text{Ca}_6(\text{H}_2\text{O})_6[\text{FeIII}_9\text{O}_6(\text{PO}_4)_9] \cdot 3\text{H}_2\text{O}$. A noteworthy octahedral sheet structure. *Am. Min.* **16**, 1096-1106.
- Ravel, B., Newville, M. (2005). ATHENA, ARTEMIS, HEPHAESTUS: data analysis for X-ray absorption spectroscopy using IFEFFIT. *J. Synchrotron Rad.* **12**, 537-541.
- Voegelin, A., Kaegi, R., Frommer, J., Vantelon, D., Hug, S.J. (2010). Effect of phosphate, silicate, and Ca on Fe(III)-precipitates formed in aerated Fe(II)- and As(III)-containing water studied by X-ray absorption spectroscopy. *Geochim. Cosmochim. Acta* **74**, 164-186.